A NEW MEASUREMENT OF THE NEUTRON MULTIPLICITY EMITTED IN ^{252}Cf SPONTANEOUS FISSION

A Dissertation
Submitted to
the Temple University Graduate Board

In Partial Fulfillment
of the Requirements for the Degree
DOCTOR OF PHILOSOPHY

---

by
Adam B. Hansell
August 2020

Examining Committee Members:

James Napolitano, Department of Physics, Advisory Chair
Donald Jones, Department of Physics
Martha Constantinou, Department of Physics
Russell Neilson, External Reader, Department of Physics, Drexel University

ABSTRACT

The Precision Reactor Oscillation and SPECTrum Experiment (PROSPECT) was designed to probe short baseline oscillations of electron antineutrinos in search of eV-scale sterile neutrinos and precisely measure the ^{235}U reactor antineutrino spectrum from the High Flux Isotope Reactor (HFIR) at Oak Ridge national Laboratory (ORNL). The PROSPECT antineutrino detector (AD) provided excellent background rejection due to its segmented design and use of ^{6}Li-loaded liquid scintillator (LiLS) for a neutron capture target. By tracking the neutron capture lifetime from cosmogenic neutrons and a ^{252}Cf neutron source, we suspect the ^{6}Li content of our scintillator changed over time. In this thesis, I will look at this evolution and how it minimally affected the uncertainty in the published results in the PROSPECT oscillation and spectrum analyses.

Additionally, the ^{252}Cf source data taken with the PROSPECT AD for detector calibrations are used to make a new measurement on the neutron multiplicity probability distribution emitted during the spontaneous fissions of ^{252}Cf, with an average multiplicity of 3.81 ± 0.05 neutrons per fission.

ACKNOWLEDGEMENTS

The work presented in this thesis would not have been possible without the assistance and support from many, nor without perching on the shoulders of intellectual giants. First and foremost, I must thank Jim Napolitano and Don Jones for advising me through the entire PhD process and helping me figure out how to bridge the gap of where I was and where I needed to be. This was a particularly difficult task towards the end due to various complications surrounding the 2020 pandemic. Thank you for sticking with me through all this.

Within our local Temple group, I'm grateful to Danielle Berish Landschoot for being a wonderful colleague and talking through the minutia of our research together, and to James Wilhelmi for being a great companion on all the long car rides and extended stays in hotel rooms during the work on our detector. Keep blessing the rains down in Africa, my friends.

I am very thankful to have been part of PROSPECT, and owe a great deal of gratitude to the collaboration. To Tim Classen and Pieter Mumm for taking me under their wings early on to help me become a "neutron guy," and ultimately helping me find my niche within the group. To the folks who assisted in the calibration campaigns on-site at ORNL (Jeremy Lu, Corey Gilbert, Andrew Conant, Brennan Hackett), for helping me maintain my sanity for those long weeks and a couple very stressful incidents. To Nathaniel Bowden and James Nikkel for their guidance and shared wisdom while supervising these campaigns and beyond. To Tom Langford, Bryce Littlejohn and Michael Mendenhall, for teaching me the "true nature" of neutrons, and answering a million questions about our experiment and programming, from the mundane to the inane. To Danielle Norcini, Pranava Surukuchi, Xianyi Zhang, Jeremy Gaison, Ben Foust, Olga Kyzylova and Christian Nave, for all the time assembling our detector and over various meetings, dinners, and conferences.

I couldn't have asked for better colleagues with whom to share time, conversation, laughs and "discount" sushi.

I am fortunate to have the support and love of my family since day one. To my parents, I wouldn't have gotten this far without your guidance on how to live my life in a meaningful way. To my brothers Jason, Nathan, Christopher, and Chuck, thank you for being the best friends and inspirations I could ask for. I doubt I would have pursued a career in physics if not for the scientific curiosity I learned from you. You all have been the best role models in your own individual ways, and I can't thank you enough for that.

Lastly, and most importantly, to my wife, Melissa. Thank you for being there from the start of this journey at Temple, putting up with my many sleepless nights, and sharing your Sugar Crisp, of which we both can't get enough. You make the fruits of this whole endeavor all the sweeter.

TABLE OF CONTENTS

ABSTRACT **i**

ACKNOWLEDGEMENTS **ii**

LIST OF FIGURES **vii**

LIST OF TABLES **xix**

1 NEUTRINOS **1**

- 1.1 Conception and Early History 1
- 1.2 Neutrino Mass Emergence and Oscillations 2
- 1.3 Neutrino Oscillation Evidence 6

2 REACTOR NEUTRINOS **11**

- 2.1 Detecting Reactor Neutrinos 12
- 2.2 Reactor Antineutrino Spectrum Models 13
- 2.3 Reactor Antineutrino Measurements 15

3 THE PROSPECT EXPERIMENT **21**

- 3.1 The High Flux Isotope Reactor 21
  - 3.1.1 On-site Backgrounds 22
- 3.2 PROSPECT Antineutrino Detector 23
  - 3.2.1 Scintillator 26
  - 3.2.2 PMT Housings 26
  - 3.2.3 Segmentation 28
  - 3.2.4 Optical Lattice and Supports 28
  - 3.2.5 Shielding 30
  - 3.2.6 Pulse Shape Discrimination 31

    3.2.7 Data collection 33
    3.2.8 Position Reconstruction 33
    3.2.9 Energy Reconstruction 35
  3.3 PROSPECT Calibration System 37
    3.3.1 Optical Calibrations 38
    3.3.2 Radioactive Source Calibration System 39
    3.3.3 Sources 39
  3.4 Monte-Carlo Simulations 41
    3.4.1 Energy Response and Resolution 41
  3.5 Conclusions 44

4 NEUTRON RESPONSE IN PROSPECT 45
  4.1 Background Rejection With Neutrons 47
  4.2 Neutron Sources and Targets 48
  4.3 Detector Stability With Cosmogenic Neutrons 50
    4.3.1 Energy Resolution Stability 51
    4.3.2 Neutron Capture Lifetime 54
      4.3.2.1 nLi Lifetime Effect on IBD Efficiency 57
      4.3.2.2 Capture Lifetime Impact on Oscillation Analysis . . 58
  4.4 Benchmarking Lithium Content in PG4 63
    4.4.1 Lithium Doping Fraction in PG4 63
      4.4.1.1 Source Deployment Locations 63
      4.4.1.2 Event Identification 64
      4.4.1.3 Matching Simulation to Data 66
      4.4.1.4 Capture Ratio 70
      4.4.1.5 nH Capture Lifetime 71
      4.4.1.6 nLi Capture Lifetime 74
      4.4.1.7 Error from nH energy cut 75
      4.4.1.8 Error from time cut 76
      4.4.1.9 Summary of Doping Methods 77
    4.4.2 Neutron Singles Mobility 79
    4.4.3 Spatial Capture Efficiency 82
      4.4.3.1 nLi Singles Efficiency 84
      4.4.3.2 Coincident nLi Efficiency 87
  4.5 Indications and Effects of Lithium Loss 90

4.5.1 Lithium Loss Prediction from Cosmogenic Neutrons 91
4.5.2 Effects of Lithium Loss on IBD Efficiency 94
4.6 Conclusions 96

5 CF-252 NEUTRON MULTIPLICITY 98
5.1 Event Selection 98
5.2 Accidentals Pileup Treatment 100
5.3 False Triggers 103
5.3.1 Beta Decays From Fission Fragments 103
5.3.2 Other Fission Induced Signals 104
5.3.3 Background events 105
5.4 Neutron Detection Efficiency Inversion 107
5.5 Simulation Cross Checks 109
5.5.1 Accidentals Distribution Cross Check 110
5.6 Final Multiplicity Distribution 111

6 CONCLUSIONS 114

BIBLIOGRAPHY 116

APPENDIX 127

LIST OF FIGURES

1.1 Experimental data from the ALEPH, DELPHI, L3, and OPAL Collaborations for the cross section of e^+e^- annihilation. Curves show predictions of the standard model for the existence of two, three, and four species of light neutrinos [9, 10]. 2

1.2 Spectrum of the solar neutrino fluxes corresponding to the SFII-GS98 standard solar model. Electron capture from Carbon-Nitrogen-Oxygen (CNO) solar fusion cycle neutrinos (ecCNO) have been added in addition to standard fluxes. Electron capture fluxes are given in $\mathrm{cm}^{-2}\mathrm{s}^{-1}$ [15]. 7

1.3 Pattern of neutrino masses for the normal and inverted hierarchies shown as mass squared. Flavor composition of the mass eigenstates is indicated. $\Delta m^2_{atm} \approx |\Delta m^2_{31}| \approx |\Delta m^2_{32}|$ and $\Delta m^2_{sol} \approx \Delta m^2_{21}$ stands for the atmospheric and solar mass-squared splitting, respectively. This naming comes from historical convention [30]. 10

2.1 Predicted summation method of $\bar{\nu}_e$ for 4 major reactor fuel isotopes, using the JEFF-3.1.1 database fission fragment yields and the ENDF/B-VII.1 decay library [31]. 14

2.2 A sample reactor flux (b), IBD cross section (c), and detectable IBD spectrum (a) vs energy, as measured by a 12-ton fiducial mass detector located 0.8 km from a 12-GW_{th} power reactor [12]. 15

2.3 Comparison of measured antineutrino energy spectra observed from Daya Bay [32], RENO [48] and Double CHOOZ [49], showing more neutrinos in the 4-6 MeV energy range than predicted based on the Huber+Muller model [59]. 17

2.4 Rate of reactor antineutrino candidates in the six detectors used by Daya Bay [32]. Also shown are the rates predicted by the Huber+Mueller (blue) and ILL+Vogel (orange) models. 18

2.5 Reactor neutrino flux measurements, showing a ∼5-6% deficit from the Huber+Mueller prediction [61]. 18

2.6 Regions allowed in Δm^2_{14} and $\sin^2(2\theta_{14})$ (listed as Δm^2_{new} and $\sin^2(2\theta_{new})$)from ν_e and $\bar{\nu}_e$ disappearance experiments mentioned in text. The black star represents the best fit point suggesting $|\Delta m^2_{14}| > 1.5$ eV^2 and $\sin^2(2\theta_{14}) = 0.14 \pm 0.08$ at the 95% confidence level [66]. 19

3.1 Model of the HFIR core [70]. (a) and (b) show the diameter and height. (c) shows the HFIR core location from simulation, and (d) is a projection of the fission power density of HFIR [59]. 22

3.2 PROSPECT AD schematic and positioning relative to HFIR Core at Oak Ridge National Lab. [59] 24

3.3 Cross section of one segment in the PROSPECT AD grid, comprising of two photomultiplier tube housings on either end (Section 3.2.2), and reflective panels surrounding the active segmented volume (Section 3.2.4). 24

3.4 Illustration of IBD, the e$^+$e$^-$ annihilation prompt signal, and the neutron capture delay signal, described in text. 25

3.5 PROSPECT detector cross section showing the segments using the 68 ET PMTs (red) and 240 Hamamatsu PMTS (blue). 27

3.6 Detailed schematic of PMT housing modules described in text. 27

3.7 Pinwheel types used in the optical support lattice in the PROSPECT AD. (a) central pinwheel - three tabs per side hold the optical separator in place. (b) end pinwheel - spacer arms separate the PMT housing bodies and support the pinwheel string. 29

3.8 Diagram of a single PROSPECT segment. PMT housings are inserted into the optical grid on each end. (a) PMT housing with end plugs and cables out. (b) center pinwheels and optical separators, resulting in the 5.5 degree tilt. (c) end pinwheel spacer arms against adjacent segments. 29

3.9 Cross section of the design of the PROSPECT AD, showing the inner volume and the various layers of shielding. 30

3.10 Light yield for a common scintillator when excited by electrons and protons [76]. 31

3.11 The total components of the scintillation as light yield (normalized y axis) in time for neutron recoils and Compton scatters from a PROSPECT prototype. Depending on the exciting particle, more of the total light yield will be in the delayed fluorescence [77]. 32

3.12 Event PSD (vertical axis) and Energy (horizontal axis) from a distribution of ^{252}Cf neutron and gamma ray events from a PROSPECT prototype. Neutron-proton recoils contribute to the top ‘neutron recoil’ band, while gamma ray compton scatters contribute to the lower band. The distribution of nLi captures can be seen at PSD = 0.3 with energy near 0.55 MeV [77]. 33

3.13 Sample high energy cosmogenic rates vs timing difference between *dt* between PMTs. Data are plotted in blue, with red fit curves as described in text. The spacing between data peaks correlates to the pinwheel tabs in the detector [78]. 34

3.14 Reconstructed position, z as a function of the *dt* between segment PMTs for high energy cosmogenic uniform events[78]. 35

3.15 Left: Near exponential light transport efficiency curves for each PMT in a segment, as a function of energy deposit location. Right: nLi events in one segment vs *dt*, with a quadratic fit in red. 36

3.16 Left: Example of pulse area and PSD for neutron capture coincident events. The magenta rectangle outlines the clear neutron capture on ^{6} energy peak isolated in "energy" and PSD. Right: Ratio of the waveform integrals from two PMTs in a sample segment. The magenta line is a cubic polynomial fit that is used to correct the position dependent energy reconstruction [79]. 36

3.17 Cross section of AD showing vertices of source tubes (red) and optical diffusers (yellow). 38

3.18 PROSPECT source calibration system. 35 motor drives fit into a box approximately 2 m wide, and extend from the face of the detector by only 14 cm. During operation, the box is covered with panels to ensure that light does not travel into the detector volume. 39

3.19 Dimensions of aluminum radioactive source capsules used in the source tubes. Numerical tags are in millimeters. 40

3.20 Source capsule with section of timing belt. The belt slides sideways through the fitted belt connector. 40

3.21 The characterized energy resolution of energies for calibration sources fit to the resolution function. [69]. 42

3.22 Calibration data to best fit MC comparison with energy scale uncertainties. Top: The reconstructed energy for gamma ray sources. Center: The reconstructed energy for nH captures from a ^{252}Cf deployment. Bottom: The reconstructed energy for cosmogenically-produced ^{12}B.[84]. 43

4.1 Neutron capture cross sections on ^{6}Li ($\sigma_{a,Li}$, red, top), ^{35}Cl ($\sigma_{a,Cl}$, yellow, middle top), H ($\sigma_{a,H}$, blue, middle bottom) and ^{12}C ($\sigma_{a,C}$, black, bottom). The peaks in $\sigma_{a,Li}$ and $\sigma_{a,Cl}$ corresponds to a nuclear resonance energy levels. The blue vertical line indicates thermal neutron energy (0.025 eV) [88]. 49

4.2 A sample energy spectrum of the nH captures following a cosmogenic event (with accidentals subtraction) using 7 days of data. The red triangles show the reconstructed energy, while the blue squares represent the E_{smear} parameter. Gaussian fit lines are shown in Black on each distribution. 52

4.3 Mean of gaussian fit to nH Energy peak vs time. The red triangles show the reconstructed energy, while the blue squares represent the E_{smear} parameter. Linear fits applied yield stability within ±0.5%. . . 53

4.4 nH energy 1σ Gaussian width vs time. The red triangles show the reconstructed energy, while the blue squares represent the E_{smear} parameter. Linear fit trend described in text and Table 4.3. The varying statistical error bars comes from the difference in reactor on and off cycles. 53

4.5 PSD for energy near 0.53 MeV. The left distribution shows the gamma band from Figure 3.12, and the right distribution shows the nLi capture peak. The gamma band is fit with a Gaussian, and nLi are selected as events above 3.6σ above the left distribution, marked by the vertical red line. 56

4.6 Sample nLi capture lifetimes from 5 consecutive days of cosmically induced neutron data in early May 2018, to times below the fit range. Light Blue is coincidence events, magenta is the accidentals distribution, and dark blue with the red fit line is the accidentals-subtracted distribution. Error bars are statistical. Exponential fit applied is described in Equation 4.5, where the capture lifetime τ is 49.83 ± 0.05 μs. 56

4.7 nLi lifetime constant (τ) per 5 day bins from March until October 2019. Error bars are from the exponential fit errors like in Figure 4.6. A linear fit was applied to find the projected increase of 4.31 ± 0.16 ns/day in nLi τ. 57

4.8 nLi capture lifetime constant (τ) time evolution per row for the top half of the detector. Linear fit results are given in Table 4.10. 59

4.9 nLi capture lifetime constant (τ) time evolution per row for the bottom half of the detector. Linear fit results are given in Table 4.10. 60

4.10 Change in nLi capture lifetime (μs/year) for each row of the detector. The shaded region indicates the total detector average. Plotted values found in Table 4.5. 61

4.11 IBD detection efficiency from the capture lifetime window by row, at the beginning of data taking (black squares) and predicted 1 year (red triangles) from Table 4.6. Shaded regions show 0.3% (black) and 0.5% (red) range of the 9-row average for the data. 62

4.12 Location of ^{252}Cf deployment represented by a dot in detector for different deployment dates. May '18 top left, Aug '18 top right, Dec '18 middle left, Feb '19 middle right. Shaded boxes represent segments unusable for analysis. 64

4.13 PSD and Energy 2-D histogram of single pulses from August calibration data. The red dashed line signifies the 3-σ circular cut on the PSD and energy peaks used for nLi selection. 66

4.14 Sample optimization curves for the February data set. Each plot shows the χ^2 difference between data and simulation when varying μ and σ of the Gaussian term η. The fit is a quadratic polynomial used to minimize the χ^2 value. 68

4.15 Optimized match of nH energy spectra (blue data, red simulation), with residual data - sim below for each of May '18 (top left), Aug '18 (top right), Dec '18 (bottom left), and Feb '19 (bottom right). Red line in residual is a horizontal fit line. 69

4.16 Optimized match of nLi energy spectra (blue data, red simulation), with residual data-sim below for each of May '18 (top left), Aug '18 (top right), Dec '18 (bottom left), and Feb '19 (bottom right). Red line in residual is a horizontal fit line. 69

4.17 Optimized match of nLi PSD distribution (blue data, red simulation), with residual data-sim below for each of May '18 (top left), Aug '18 (top right), Dec '18 (bottom left), and Feb '19 (bottom right). Red line in residual is a horizontal fit line. 70

4.18 nH/nLi capture ratio for various doping fractions given on/off segment orientation for each data set. Black represents the simulated capture ratios, the blue lattice region represents the capture ratio range for data with uncertainty, and the red line is the fit from Equation 4.15. . 71

4.19 Neutron capture time on hydrogen in data (left) and an example simulation (right) for Feb '19 for the correlated time distribution (light blue), accidentals scaled timing distribution (magenta), and the accidentals subtracted curve (dark blue hatches), with red fit line $y = p_0 \cdot e^{\frac{-t}{\tau}}$. 72

4.20 nH capture lifetimes for various doping percentages. Black represents the simulated nH capture lifetimes, the blue lattice region represents the nH capture lifetime for data with uncertainty, and the red line is the $\tau = \frac{p_0}{\text{Doping Fraction}} + p_1$ fit. 73

4.21 Neutron capture time on lithium in data (left) and example simulation (right), for the correlated time distribution (light blue), accidentals scaled timing distribution (magenta), and the accidentals subtracted curve (dark blue hatches), with red fit line $y = p_0 \cdot e^{\frac{-t}{\tau}}$. 74

4.22 nLi capture lifetimes for various doping percentages. Black represents the simulated nLi capture lifetimes, the blue lattice region represents the nLi capture lifetime for data with uncertainty, and the red line is the $\tau = \frac{p_0}{\text{Doping Fraction}} + p_1$ fit. 75

4.23 nH capture energy for August calibration data. Since histograms are normalized to their integrals, the fit residual around the peak looks worse than previously in Figure 4.15. 76

4.24 Doping percentage match for each calibration data set with linear fit. Blue data points represent the doping percentage to match the nH capture lifetime, red for the nLi capture lifetime, and black for the capture ratio (nH/nLi). Black lattice region around the nH/nLi ratio is the systematic error from changing the nH energy cut or the timing cut described in previous sections. 78

4.25 PSD and Energy of events near the nLi peak in data (left) and simulation (right). The red dashed lines outline a 3σ circular region in the two axes. 80

4.26 Optimization curve for simulation position resolution smearing to match data. χ^2 per degrees of freedom between data and simulation position distributions. The fit is a quadratic polynomial used to minimize the χ^2 value. 80

4.27 Comparison of the reconstructed position distribution of nLi captures from the ^{252}Cf source. Data is in blue, simulation in red. Simulation is smeared by a value determined by the χ^2 minimization demonstrated in Figure 4.26. The bottom plot is the residual between data and simulation. The fit is consistent with 0 at the $< 2\sigma$ level with good χ^2. 81

4.28 Detected nLi capture rates for regions of differing distance to ^{252}Cf location (black circle in region scheme). The inset image defines which segments are assigned to which region bin; in this inset, 'X' indicates an inactive segment. Blue dots represent data, while red lines represent PG4 simulations. As seen in Table 4.15, these two distributions agree within error out to region 3. 82

4.29 ^{252}Cf source deployment locations used for the efficiency study. 83

4.30 PSD spectrum near the nLi peak for data (left) and simulation (right). Gaussian fits are applied to determine cut widths. 84

4.31 Energy spectrum for data (left) and simulation (right), within 3-sigma range of PSD determined in Figure 4.30. The Figures' applied fit is a Gaussian plus an exponential term. 85

4.32 nLi singles detection efficiency as described in text comparing Simulation (dashed line) to data (solid line) for the top two Figures for a central (left) and edge (right) source deployment. The shaded region around data values represents the systematic error associated with the source strength uncertainty. The bottom two Figures show the ratio of simulation/data for each point. Segment ends are denoted by vertical blue lines. 86

4.33 nLi singles effficiency curves from Figure 4.32 but using the absolute value along the z-axis, utilizing the source deployment offset to fill out the efficiency points. Segment ends are denoted by vertical blue lines. The ratio plots are fit with a constant out to 500 mm as discussed in text. 87

4.34 nLi coincidence detection efficiency as described in text comparing Simulation (dashed line) to data (solid line) for the top two Figures for a central (left) and edge (right) source deployment. The bottom two Figures show the ratio of simulation/data for each point. 89

4.35 nLi coincidence efficiency curves from Figure 4.34 but using the absolute value along the z-axis, utilizing the source deployment offset to fill out the efficiency points. The ratio plots are fit with a constant out to 500 mm as discussed in text. 90

4.36 Calculated fractional loss in ^{6}Li (red) and ^{227}Ac (blue) [80] per row. The shaded regions represent the full detector averages. 94

5.1 ^{252}Cf spontaneous fission gamma energy spectrum selection for nonzero neutron multiplicities. Signals at low energies and nH captures motivates the energy selection of E $>$ 3.0 MeV to eliminate signals not from ^{252}Cf spontaneous fission. 99

5.2 Multiplicity of nLi captures coincident with a fission trigger. Error bars are statistical. The excess of events with zero multiplicity is discussed in the text. 100

5.3 Accidental nLi multiplicity distribution, A_i from Equation 5.1, for a deployed ^{252}Cf source. 102

5.4 Neutron multiplicity distribution after applying the treatment from Equation 5.4 using the distribution from 5.3 for distribution A_i. nLi multiplicities past 8 are consistent with 0 in statistically propagated error. Y axis is converted to Rate for comparison with later plots. . . 102

5.5 Beta energy distribution from fission fragments produced from ^{252}Cf spontaneous fission [98]. 103

5.6 Electron energy loss in aluminum as a function of the electron energy [99]. 104

5.7 Coincidence nLi multiplicity distribution for ambient background data. 105

5.8 Accidental nLi multiplicity distribution for ambient background data. 106

5.9 Background nLi multiplicity distribution after the accidentals pileup treatment in Equation 5.4 using the distributions in Figures 5.7 and 5.8, converted to a rate for comparison to the coincidence distribution. 106

5.10 TOP: nLi multiplicity rate distribution comparing data from the source measurements, background measurements, and the calculated beta rate from the source. BOTTOM: The background and beta rates subtracted from the source rates, with errors added in quadrature. 107

5.11 Resulting multiplicity distributions after efficiency correction in Equation 5.7. The multiple distributions cover the range of uncertainty in our efficiency. Error bars are statistical and propagated from Figure 5.10. Multiplicities above 10 are shown to exhibit the oscillatory behavior from the inversion described in text. Statistical error bars for these higher multiplicities are ignored since they are not reported later, and extend outside the range of the y-axis. 109

5.12 Toy simulation (red) and data (blue) for the accidentals multiplicity distribution from a ^{252}Cf source (top), with the plotted difference between the distributions (bottom). The red band signifies systematic error from the neutron capture lifetime and efficiency. 110

5.13 Neutron multiplicity probability distribution from the spontaneous fission of ^{252}Cf from this work (black circles) compared to the distributions from Holden & Zucker [92] (teal squares) and Santi & Miller [93] (red triangles). 111

6.1 ^{252}Cf manufacturer source certificate. 127

LIST OF TABLES

1.1 The best fit values and 3σ allowed ranges of the 3-neutrino oscillation parameters [12]. Values outside parentheses are for the normal mass hierarchy, and values inside the parentheses are for the inverted mass hierarchy. 9

3.1 The various radioactive calibration sources used in the PROSPECT detector. 40

4.1 Density and composition of the PROSPECT Scintillator [74]. 49

4.2 Cuts used to identify nH captures after a cosmically induced event. . 51

4.3 Slopes from the linear fits in Figure 4.4. 53

4.4 Cuts used to identify nLi captures after a cosmically induced event. . 55

4.5 Summary of the change in the nLi capture lifetime, from linear fits in Figures 4.7, 4.8, and 4.9. 61

4.6 Projected change in nLi capture lifetime over 1 year given linear trends in fit lines in Figures 4.7, 4.8, and 4.9. 62

4.7 Data selection criteria for location nLi and nH captures from a ^{252}Cf source for the doping study. 65

4.8 Values used on simulation to minimize χ^2 to data. “Shift” refers to the non-zero Gaussian mean of η, and “smear” is related to σ_{Gaus} in MeV. 67

4.9 Capture ratios and doping fractions required to match simulation to data for each calibration data set. 71

4.10 Neutron capture lifetimes on hydrogen for each calibration data set, and the ^{6}Li doping fraction required to match that value in simulation. 74

4.11 Neutron capture lifetimes on ^{6}Li for each calibration data set, and the ^{6}Li doping fraction required to match that value in simulation. 75

4.12 Doping fraction difference for each calibration data set for nH/nLi, using a time window of 20-250 μs instead of 2-250 μs. 77

4.13 Doping fractions required to match simulation to data for each calibration data set for all 3 methods. nH/nLi ratio systematic errors are from changing the nH energy cut and the timing cut described in previous sections. 78

4.14 Loss of ^{6}Li doping fraction determined from linear fit in Figure 4.24. Absolute % loss is given compared to the May ’18 doping fraction. . . 79

4.15 nLi capture rates per region in Figure 4.28 for Data and Simulation . 82

4.16 Selection Cuts summary for coincident nLi efficiency. The 3σ cuts on energy and PSD can be seen in Figure 4.25. 88

4.17 Percentage ^{6}Li loss annually from Figure 4.36. 93

4.18 Values used to determine the thermal neutron capture probability on ^{6}Li [74, 88]. 95

4.19 Change in IBD efficiency between rows 1, 4, and 10 in the detector due to the loss of lithium in the detector from Table 4.17 after 3 months and 1 year. These values assume a 0.7546 starting efficiency for each row, based on a ^{6}Li doping fraction of $7.9 \cdot 10^{-4}$. 96

5.1 Neutron multiplicity probability distribution of ^{252}Cf spontaneous fission from this work, compared to the values from Holden & Zucker [92] and Santi & Miller [93]. 112

CHAPTER 1

NEUTRINOS

Neutrinos are nearly massless particles that rarely interact with matter, and were conceived before they were detected. Their conceptual existence began as a solution to the energy spectrum from beta decay, but has since posed more interesting questions to the Standard Model of particle physics.

1.1 Conception and Early History

Measurements of the radiation from beta decay by Chadwick in 1914 [1] showed continuous electron energies. At the time, beta decay was believed to be a 2-body decay, and the proton and electron energies should be fixed by kinematics. In 1930, Wolfgang Pauli conceived a neutral, spin 1/2 particle emitted during beta decay (Equation 1.1) in order to explain the continuous energy spectrum [2]. In 1934, Fermi laid out the formalism for this particle, coining the name neutrino, along with the theory of beta decay [3], where a decaying neutron produces a proton, electron, and electron antineutrino:

$$n \rightarrow p + e^- + \bar{\nu}_e. \tag{1.1}$$

In 1956, Reines, Cowan *et al.* detected experimentally the neutrino at the Savannah River reactor, eventually earning the Nobel Prize in 1995 [4, 5, 6]. Albeit one of the most abundant particles in the universe, the neutrino and its anti-particle (the antineutrino) are extremely difficult to detect, since they only interact via the weak and gravitational forces. With experimental measurements and the field theory from Fermi, the weak interaction cross section is calculated to be $\mathcal{O}(10^{-20}\text{ b})$, more than 10 orders of magnitude lower than typical electromagnetic cross sections.

In 1962, an experiment at Brookhaven National Lab by Lederman, Schwartz, and Steinberger showed that more than one type of neutrino exists, distinguishing between the electron and muon neutrino, earning a Nobel Prize in 1988 [7]. The discovery of the tau lepton in the 1970s implied the existence of a third flavor of neutrino (the tau neutrino), which was experimentally confirmed in 2000 by the DONUT collaboration [8]. As shown in Figure 1.1, experimental measurements of the Z^0 width performed at the Large Electron-Proton (LEP) Collider demonstrated with high precision that there are only three flavors of light neutrinos corresponding to the electron, muon, and tau leptons [9, 10]. However, the existence of more flavors that interact differently than these three is not ruled out.

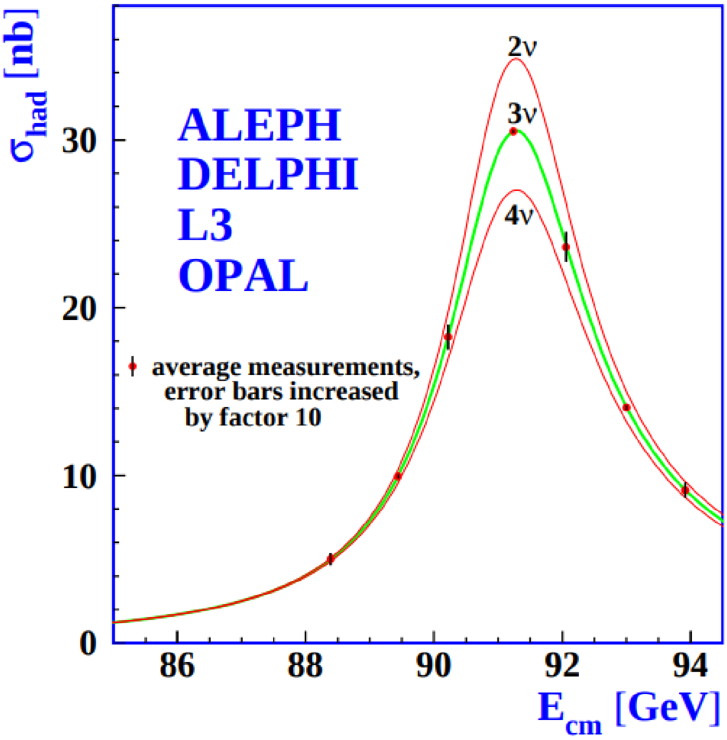

Figure 1.1: Experimental data from the ALEPH, DELPHI, L3, and OPAL Collaborations for the cross section of e^+e^- annihilation. Curves show predictions of the standard model for the existence of two, three, and four species of light neutrinos [9, 10].

1.2 Neutrino Mass Emergence and Oscillations

In line with Fermi's neutrino formalism and according to the Standard Model of Particle Physics, neutrinos were initially assumed to be massless. Since then, experiments have shown not only the existence of three leptonic flavors of neutrinos, but also three mass eigenstates which are linear combinations of the neutrino flavor eigenstates and vice versa [11]. The rest mass of these eigenstates are not currently known, but in addition to constraints on the total mass and individual upper limits, measurements have been made on the mass squared difference between the mass eigenstates [12]. Two of the key measurements in many neutrino oscillation experiments is the mass squared difference between these neutrino mass eigenstates, and the mixing angle between the mass eigenstates. As will be evident in the following derivation, the mixing of neutrino states is intimately connected to the neutrino mass eigenstate masses. If each neutrino had the same mass, then there would not be any neutrino oscillations.

Conceptually, it is helpful to start by deriving the two neutrino mixing case, and then address the format for the full three known neutrino mixing. If the electron and muon neutrino flavor states, ν_e and ν_μ respectively, can change identity into one another, then neither is an eigenstate of the full Hamiltonian. Let us first consider the mixing of only two neutrinos, starting with the electron and muon neutrino. Say ν_e and ν_μ exist as a superposition of 2 orthogonal, linear combinations of the mass eigenstates ν_1 and ν_2:

$$\begin{bmatrix} \nu_\mu \\ \nu_e \end{bmatrix} = \begin{bmatrix} \cos(\theta) & \sin(\theta) \\ -\sin(\theta) & \cos(\theta) \end{bmatrix} \begin{bmatrix} \nu_1 \\ \nu_2 \end{bmatrix} \tag{1.2}$$

The use of trigonometric functions and a neutrino mixing angle θ is common convention to enforce normalization for the unitary transformation matrix. Subscripts will be introduced to denote mixing of specific states, in this case we would use θ_{12} to denote a mixing between the ν_1 and ν_2 states. These eigenstates have a simple time dependence according to the Schrödinger Equation,

$$|\nu_1(t)\rangle = e^{-iH_1 t} |\nu_1(t=0)\rangle = |\nu_1(t=0)\rangle \, e^{-iE_1 t/\hbar} \tag{1.3a}$$

$$|\nu_2(t)\rangle = e^{-iH_2 t} |\nu_1(t=0)\rangle = |\nu_2(t=0)\rangle \, e^{-iE_2 t/\hbar} \tag{1.3b}$$

giving a neutrino that originated as $|\nu_e\rangle$ evolving in time as

$$|\nu_e(t)\rangle = |\nu_2(0)\rangle \cos(\theta) e^{-iE_2 t/\hbar} - |\nu_1(0)\rangle \sin(\theta) e^{-iE_1 t/\hbar}. \tag{1.4}$$

The probability that a neutrino originating as $|\nu_e\rangle$ being detected as $|\nu_\mu\rangle$ at time t is

$$P_{\nu_e \to \nu_\mu}(t) = |\langle \nu_\mu | \nu_e(t) \rangle|^2 \tag{1.5}$$

The $|\nu_1\rangle$ and $|\nu_2\rangle$ states are orthonormal to each other, so Eq. 1.5 simplifies to

$$P_{\nu_e \to \nu_\mu}(t) = |\sin(\theta)\cos(\theta)(e^{-iE_2t/\hbar} - e^{-iE_1t/\hbar})|^2 \tag{1.6}$$

$$P_{\nu_e \to \nu_\mu}(t) = \left| \frac{1}{2}\sin(2\theta)(e^{-iE_2t/\hbar} - e^{-iE_1t/\hbar}) \right|^2 \tag{1.7}$$

Squaring the absolute values by parts and using trigonometric identities, we get

$$P_{\nu_e \to \nu_\mu}(t) = \sin^2(2\theta)\sin^2\left(\frac{(E_2 - E_1)t}{2\hbar}\right) \tag{1.8}$$

To further interpret this probability, we assume neutrinos have fixed momentum and relate the highly relativistic neutrino energy to its momentum and mass ($|p| \gg mc$ for m_1 and m_2).

$$E^2 = |p|^2c^2 + m^2c^4 = |p|^2c^2\left(1 + \frac{m^2c^2}{|p|^2}\right) \tag{1.9}$$

$$E \approx |p|c(1 + \frac{1}{2}\frac{m^2c^2}{|p|^2}) = |p|c + \frac{m^2c^3}{2|p|} \tag{1.10}$$

$$E_2 - E_1 \approx \frac{m_2^2c^3 - m_1^2c^3}{2|p|} \approx \frac{m_2^2 - m_1^2}{2E}c^4 \tag{1.11}$$

Entering this into the neutrino oscillation probability gives

$$P_{\nu_e \to \nu_\mu}(t) = \left[\sin(2\theta)\sin\left(\frac{(m_2^2 - m_1^2)c^4}{4\hbar E}t\right)\right]^2 \tag{1.12}$$

For highly relativistic particles, we can approximate the distance a neutrino travels as $L \approx ct$, finally giving

$$P_{\nu_e \to \nu_\mu}(L) = \sin^2(2\theta)\sin^2\left(\frac{c^3}{\hbar}\frac{\Delta m_{21}^2}{4E}L\right) \tag{1.13}$$

where $\Delta m_{21}^2 = m_2^2 - m_1^2$, so Δm_{ij}^2 can take on negative values. The emerging mass difference allows the mass eigenstates to get out of phase with respect to each other, so measurements can pick these out by measuring the projection of one flavor state to another in Equation 1.5. It is common to use units of eV^2 for Δm_{ij}^2, and m/MeV for L/E, giving a representation of

$$P_{\nu_e \to \nu_\mu}(L) = \sin^2(2\theta)\sin^2\left(1.27\Delta m^2_{21}\frac{L}{E}\right). \tag{1.14}$$

The above probability is only for the case of detecting a muon neutrino that originated as an electron neutrino (while ignoring the existence of the m_3 mass eigenstate), so the mixing angle above would be written as θ_{12}. In this two neutrino example, the corresponding survival probability of the electron neutrino is

$$P_{\nu_e \to \nu_e} = 1 - P_{\nu_e \to \nu_\mu} \tag{1.15}$$

In order to calculate oscillations considering the three known types of light neutrinos (electron, muon, and tau), we will use a 3 dimensional unitary matrix to relate the flavor states in the mass eigenstate basis

$$\begin{bmatrix} \nu_e \\ \nu_\mu \\ \nu_\tau \end{bmatrix} = \begin{bmatrix} U_{e1} & U_{e2} & U_{e3} \\ U_{\mu 1} & U_{\mu 2} & U_{\mu 3} \\ U_{\tau 1} & U_{\tau 2} & U_{\tau 3} \end{bmatrix} \begin{bmatrix} \nu_1 \\ \nu_2 \\ \nu_3 \end{bmatrix} \tag{1.16}$$

where the above 3x3 unitary matrix is known as the Pontecorvo-Maki-Nakagawa-Sakata (PMNS) matrix [12]. It can be thought of as the product of three rotation matrices, each one being a rotation from one mass eigenstate to another

$$U = \begin{bmatrix} c_{12} & s_{12} & 0 \\ -s_{12} & c_{12} & 0 \\ 0 & 0 & 1 \end{bmatrix} \begin{bmatrix} c_{13} & 0 & s_{13}e^{i\delta_{CP}} \\ 0 & 1 & 0 \\ -s_{13}e^{-i\delta_{CP}} & 0 & c_{13} \end{bmatrix} \begin{bmatrix} 1 & 0 & 0 \\ 0 & c_{23} & s_{23} \\ 0 & -s_{23} & c_{23} \end{bmatrix} \tag{1.17}$$

where δ_{CP} is the phase related to CP violations, and the convention $\sin(\theta_{ij}) = s_{ij}$ and $\cos(\theta_{ij}) = c_{ij}$ is used for brevity. Multiplying through we get

$$U = \begin{bmatrix} c_{12}c_{13} & s_{12}c_{13} & s_{13}e^{i\delta_{CP}} \\ -s_{12}c_{23} - c_{12}s_{23}s_{13}e^{i\delta_{CP}} & c_{12}c_{23} - s_{12}s_{23}s_{13}e^{i\delta_{CP}} & s_{23}c_{13} \\ s_{12}s_{23} - c_{12}c_{23}s_{13}e^{i\delta_{CP}} & -c_{12}s_{23} - s_{12}c_{23}s_{13}e^{i\delta_{CP}} & c_{23}s_{13} \end{bmatrix}. \tag{1.18}$$

Given this result, the electron neutrino state in the mass eigenstate basis is

$$|\nu_e\rangle = \sum_{i=1,2,3} U_{ei} |\nu_i\rangle = c_{12}c_{13} |\nu_1\rangle + s_{12}c_{13} |\nu_2\rangle + s_{13}e^{i\delta_{CP}} |\nu_3\rangle \tag{1.19}$$

and including time evolution, we can calculate the survival probability of the electron neutrino in the three neutrino model at some time t using

$$P_{\nu_e \to \nu_e}(t) = \left| \langle \nu_e | \, e^{-iHt} \sum_{i=1,2,3} U_{ei} |\nu_i\rangle \right|^2 \tag{1.20}$$

or conversely as a function of L/E [13, 14]

$$\begin{aligned} P_{\nu_e \to \nu_e}(L/E) = 1 &- \cos^4(\theta_{13}) \sin^2(2\theta_{12}) \sin^2\left(1.27\Delta m^2_{21} \frac{L}{E}\right) \\ &- \cos^2(\theta_{12}) \sin^2(2\theta_{13}) \sin^2\left(1.27\Delta m^2_{31} \frac{L}{E}\right) \\ &- \sin^2(2\theta_{12}) \sin^2(2\theta_{13}) \sin^2\left(1.27\Delta m^2_{32} \frac{L}{E}\right). \end{aligned} \tag{1.21}$$

It becomes clear in the 3 neutrino mixing case that if all Δm^2_{ij} are zero, then the survival probability of the neutrino is always 1. The amplitude of neutrino oscillations depends on the mixing angles θ_{ij} while the oscillation wavelength depends on the squared mass difference Δm^2_{ij}. If we know the oscillation parameters Δm^2_{ij} and θ_{ij} for each mixing, we can maximize the signal disappearance by varying our detection distance depending on the energy.

1.3 Neutrino Oscillation Evidence

Early neutrino oscillation evidence came from experiments measuring the neutrino flux from the Sun. Protons in the Sun undergo fusion producing deuterium, which undergoes fusion again among other interactions, which ultimately produces electron neutrinos. Figure 1.2 shows the energies of electron neutrinos produced in the various solar reactions [15].

In the late 1960s, the Homestake experiment aimed to measure the neutrino flux from the Sun. Using Chlorine as a target for neutrino interactions:

$$\nu_e +^{37} Cl \to^{37} Ar + e^- \tag{1.22}$$

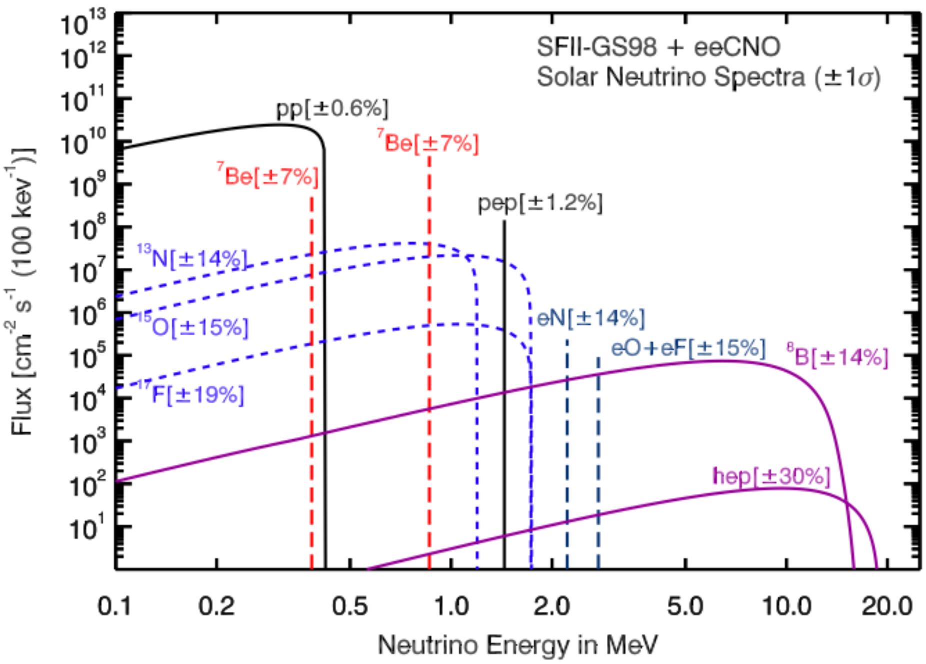

Figure 1.2: Spectrum of the solar neutrino fluxes corresponding to the SFII-GS98 standard solar model. Electron capture from Carbon-Nitrogen-Oxygen (CNO) solar fusion cycle neutrinos (ecCNO) have been added in addition to standard fluxes. Electron capture fluxes are given in $cm^{-2}s^{-1}$ [15].

and then by counting the number of radioactive Argon atoms, the experiment could determine how many electron neutrinos interacted with Chlorine in a 380 m^2 container. The energy threshold for the neutrino-Chlorine interaction is 814 keV, which allowed the experiment to measure neutrinos created by ^{8}B, ^{7}B, *pep*, ^{13}N, and ^{15}O in the Sun with intensities shown in Figure 1.2. However, the experiment only observed 1/3 of the expected number of neutrinos predicted by solar models. This discrepancy was dubbed the "Solar Neutrino Problem."

Following Homestake, three more experiments set out to measure the Sun's neutrino flux. SAGE [16], GALLEX [17], and Gallex's follow-up GNO [18] all used

$$\nu_e +^{71} Ga \rightarrow^{71} Ge + e^- \tag{1.23}$$

to detect solar neutrinos. With a neutrino energy threshold of 233 keV, these experiments were sensitive to more of the solar neutrino flux spectrum, including the *pp* neutrinos with a more easily calculated flux. All three experiments confirmed the deficit showed by Homestake. Further confirmation came from Kamiokande-II in the mid 1980s [19].

Since calculating the flux spectrum from the Sun is difficult, the science community was slow to accept neutrino oscillations as the solution to the Solar Neutrino Problem. However, Heeger and Robertson later argued that independent of solar models, the most probable solution would require Beyond the Standard Model physics [20]. Early experiments trying to measure the Sun's neutrino flux were not sensitive to muon neutrinos or tau neutrinos, so only the electron neutrinos flux was measured. Bruno Pontecorvo [21, 22] had already proposed in 1968 that if neutrinos have mass, then they can change from one flavor eigenstate to another. This implies that if the electron neutrinos had oscillated into muon and tau neutrinos, these experiments were not actually detecting the initial electron neutrino flux from the Sun. The Super-Kamiokande experiment detected atmospheric neutrino-electron elastic scattering [23], which is sensitive to all neutrino flavors. This means that they would not expect to see the deficit, since they would detect even the neutrinos that oscillated. With a 4 MeV energy threshold, it was only sensitive to the ^{8}Be channel solar neutrinos. Since they still measured a neutrino deficit of 53%, they confirmed the solar neutrino problem at high statistics and placed limits on neutrino oscillation parameters.

Definitive evidence of neutrino oscillations came from the Sudbury Neutrino Observatory (SNO) experiment in 2001, which used a heavy water Cherenkov detector. SNO was sensitive to all neutrino flavors l through the neutral current weak interaction

$$\nu_l + D \to \nu_l + n + p \tag{1.24}$$

and through neutrino-electron scattering

$$\nu_l + e^- \to \nu_l + e^- \tag{1.25}$$

but isolated detecting electron neutrinos via charged the current interaction

$$\nu_e + D \to e^- + p + p. \tag{1.26}$$

By measuring the total neutrino flux separate from the ν_e flux, they provided the first clear evidence of neutrino oscillations, earning a shared 2015 Nobel Prize in physics with a researcher with the Super-Kamiokande experiment [24]. In 2005, the

Kamioka Liquid Scintillator Antineutrno Detector (KamLAND) experiment established antineutrino disappearance at high significance [25].

The current resolution with solar neutrino oscillations includes the Mikheyev-Smirnov-Wolfenstein (MSW) effect. The MSW effect explains that electrons in matter cause electron neutrinos suffer an additional potential affecting charged current forward scattering. This leads to change in the effective mass for ν_e oscillations. Since the Sun has high a electron density, and solar neutrinos must also travel through a vacuum before reaching detectors on Earth, this effect is more pronounced for solar neutrino experiments. At high neutrino energies, the probability for neutrino survival is at a maximum, depending only on the mixing angle [26, 27, 28].

The eventual discovery of three neutrino oscillations has incidentally established that at least two neutrinos have non-zero mass. Experiments measuring the mass squared difference were not sensitive to the sign of the mass squared difference, and make no assumptions on which mass eigenstate is larger than another, resulting in two mass hierarchies, shown in Figure 1.3. Table 1.1 summarizes the knowledge of neutrino masses and mixings including neutrino mixing angles, the CP phase, and the neutrino mass-squared differences, based on fits since 2014 [12]. Some of these values will be discussed in detail with respect to the series of reactor neutrino experiments that determined them.

Parameter	Best-fit	3 σ
Δm^2_{21} $[10^{-5}\ \text{eV}^2]$	7.37	6.93 - 7.96
$\Delta m^2_{31(23)}$ $[10^{-5}\ \text{eV}^2]$	2.56 (2.54)	2.45 - 2.69 (2.42 - 2.66)
$\sin^2\theta_{12}$	0.297	0.250 - 0.354
$\sin^2\theta_{23}$	0.425 (0.589)	0.381 - 0.615 (0.384 - 0.636)
$\sin^2\theta_{13}$	0.0215 (0.0216)	0.0190 - 0.0240 (0.0190 - 0.0242)
δ/π	1.38 (1.31)	2σ: 1.0 - 1.9 (0.92 - 1.88)

Table 1.1: The best fit values and 3σ allowed ranges of the 3-neutrino oscillation parameters [12]. Values outside parentheses are for the normal mass hierarchy, and values inside the parentheses are for the inverted mass hierarchy.

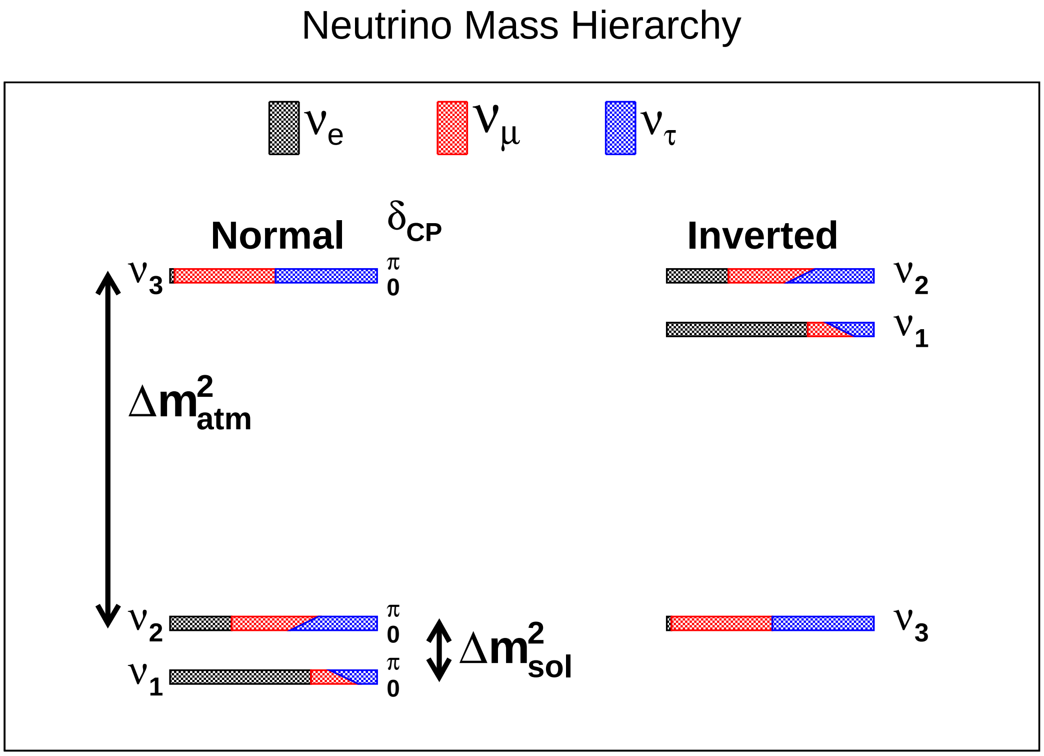
Neutrino Mass Hierarchy
ν_e
ν_μ
ν_τ
Normal
δ_{CP}
Inverted
ν_3
π
0
ν_2
ν_1
Δm^2_{atm}
ν_2
π
0
ν_1
π
0
Δm^2_{sol}
ν_3

Figure 1.3: Pattern of neutrino masses for the normal and inverted hierarchies shown as mass squared. Flavor composition of the mass eigenstates is indicated. $\Delta m^2_{atm} \approx |\Delta m^2_{31}| \approx |\Delta m^2_{32}|$ and $\Delta m^2_{sol} \approx \Delta m^2_{21}$ stands for the atmospheric and solar mass-squared splitting, respectively. This naming comes from historical convention [30].

CHAPTER 2

REACTOR NEUTRINOS

While the experiments discussed in Chapter 1 were concerned with solar neutrinos, many other experiments looked to nuclear reactors as an intense source of electron antineutrinos. Reactor experiments have more control over the distance (baseline) to detectors than experiments measuring solar neutrinos. This means experiments can better optimize various research parameters in order to test for oscillations and other aspects about neutrinos. Precision measurements from reactor neutrino experiments left the particle physics community with interesting anomalies that paved the way for a new generation of experiments.

Neutron induced fission of ^{235}U, ^{238}U, ^{239}Pu, and ^{241}Pu follow the general format of

$$\text{neutron} + X \rightarrow 2 \text{ Fission Fragments} + \text{neutrons} + \text{``Energy''} \tag{2.1}$$

where X is the fissionable heavy isotope. The neutron rich daughter particles are unstable, and will β decay on average 3 times in order to achieve stability, releasing an electron and an electron antineutrino in each decay. For every GW of thermal energy, a reactor will release $\mathcal{O}(10^{20})$ electron antineutrinos.

Reactors that use uranium as a fuel source are classified as High Enriched Uranium (HEU) which has more than 20% ^{235}U enrichment, or Low Enriched Uranium (LEU) for less than 20% ^{235}U enrichment. Although ^{238}U is typically the most abundant fission isotope in reactors, more than half of the $\bar{\nu}_e$ come from ^{235}U due to relevant neutron cross sections [31].

2.1 Detecting Reactor Neutrinos

Neutrinos are notoriously difficult to detect, since they only interact through the weak force. One common mechanism for detecting reactor electron antineutrinos uses inverse beta decay (IBD)

$$\bar{\nu}_e + p \rightarrow n + e^+, \tag{2.2}$$

a weak force, charged current interaction that proceeds via a W^+ boson exchange. This decay is a variation on the process in Equation (1.1), and is the basis for many antineutrino detector systems, such as those used by Daya Bay, Double Chooz, and even Reines and Cowan during their discovery. Since there are two products from IBD, many experiments locate the neutron and positron separately separated in short time scales. The positron annihilates with a local electron almost immediately, and the neutron captures on the nucleus of some isotope in the detector medium. The isotope type and density is chosen for a high neutron capture cross section, and to produce a characteristic de-excitation signal in times after the positron capture. This is referred to as a "prompt-delay" signal scheme. By detecting the neutron capture in this coincidence scheme, many experiments are able to reduce backgrounds by orders of magnitude [32, 33, 34].

If we ignore the relatively small neutron recoil kinetic energy, the minimum $\bar{\nu}_e$ energy for an IBD interaction is

$$E_{thresh,\bar{\nu}_e} = m_n + m_{e^+} - m_p = 1.804 \text{ MeV} \tag{2.3}$$

where we are now using natural units. The detected energy, often called the "prompt energy," which is the kinetic energy of the positron plus the combined mass of 1.022 MeV from the positron/electron pair from annihilation, is related to the energy of the $\bar{\nu}_e$ by

$$E_{\bar{\nu}_e} = E_{det} + E_{thresh,\bar{\nu}_e} - 1.022 \text{ MeV} = E_{det} + 0.782 \text{ MeV}. \tag{2.4}$$

Thus, in order to obtain the neutrino spectrum one must reconstruct it from the detected visible energy, including a model that accounts for the specifics of detector response.

2.2 Reactor Antineutrino Spectrum Models

Before addressing the measured spectrum of reactor antineutrinos, it is necessary to understand the expected neutrino flux and spectrum, as well as various models used by the community for comparison. The reactor antineutrino spectrum can be written as

$$S(E_{\bar{\nu}_e}) = \frac{W_{th}}{\sum_i f_i e_i} \sum_i f_i \frac{\partial N_i}{\partial E_{\bar{\nu}_e}} \tag{2.5}$$

where W_{th} is the thermal power of the reactor, f_i is the fission fraction of isotope i, e_i is the energy per fission for isotope i, and $\frac{\partial N_i}{\partial E_{\bar{\nu}_e}}$ is the cumulative neutrino spectrum of isotope i [31]. One method of determining the neutrino spectrum is the *ab initio* summation method, which involves summing all contributions from β decays,

$$\frac{\partial N_i}{\partial E_{\bar{\nu}_e}} = \sum_n Y_n(Z, A) \sum_{n,i} b_{n,i}(E_0^i) P_{\bar{\nu}_e}(E_{\bar{\nu}_e}, E_0^i, Z) \tag{2.6}$$

where Y_n is the fission yield of isotope (Z, A) which gives the number of β-decays at a given time, $b_{n,i}$ is the branching ratio, the index n indicates whether an isotope is in the ground or excited state, E_0^i is the endpoint of the β branches, and $P_{\bar{\nu}_e}$ is the normalized $\bar{\nu}_e$ energy spectrum from isotope n, i. This method is dependent on nuclear databases for information on branching ratios and is sensitive to uncertainties from β-spectrum shapes of forbidden transitions. Figure 2.1 shows the *ab initio* spectra from the four major reactor fission isotopes as published in Ref [31].

The *ab initio* method is difficult for many reasons. It's computationally exhaustive, there are thousands of daughter isotopes with approximately 6000 β branches, the branching ratios of multiple isotopes are poorly known, there are large uncertainties in fission yields, and there are relatively high systematic errors in nuclear calculations. These complications result in over 10% uncertainty from summation calculations [31, 35, 36, 37, 38].

An alternative to the *ab initio* summation method is the conversion method, where the measured β energy of the fissioning isotopes are converted into the $\bar{\nu}_e$ spectra. By binning the total measured β energy spectrum, a set of virtual end-point energies, E_0^i are defined. The sum from individual β spectra are experimentally fit with weighted amplitudes as

$$\frac{\partial N_i}{\partial E_e} = \sum_i a_i P(E, E_0^i, \bar{Z}(E_0^i)) \tag{2.7}$$

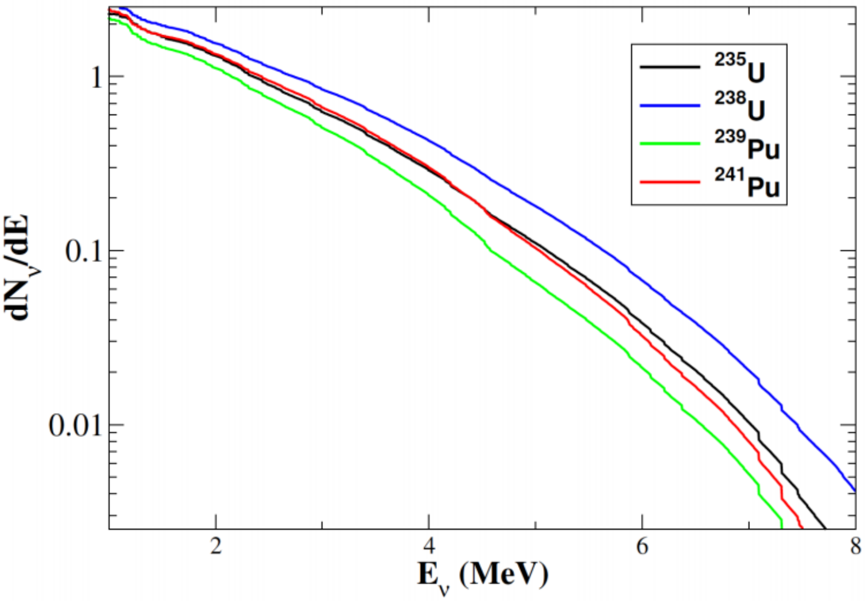

Figure 2.1: Predicted summation method of $\bar{\nu}_e$ for 4 major reactor fuel isotopes, using the JEFF-3.1.1 database fission fragment yields and the ENDF/B-VII.1 decay library [31].

for each end-point energy, where a_i is the amplitude of the virtual β branch and $\bar{Z}$ describes the mean atomic number of the fission products using the β branch endpoint energy E_0^i. For each β branch, we replace E_e with $E_0 - E_{\bar{\nu}_e}$ by conservation of energy. The flux per fission is then given as the sum of the $\bar{\nu}_e$ energy spectrum converted from each virtual β branch,

$$\frac{\partial N_i}{\partial E_{\bar{\nu}_e}} = \sum_i a_i P(E_0^i - E, E_0^i)\bar{Z}(E_0^i). \tag{2.8}$$

The conversion method is still dependent on spectral shape and energy level assumptions. The conversion method has ∼5% uncertainty coming from various experimental uncertainties [39].

Models have been developed using combinations of databases, theoretical models, and experimental data. In 1989, Vogel combined measurements of the electron spectra for (^{235}U, ^{239}Pu, ^{241}Pu) performed at the Institut Laue-Langevin (ILL) reactor in the 1980s [40, 41, 42], and calculations of the ^{238}U spectrum to comprise the “ILL-Vogel” flux model [43]. In 2011, to improve the accuracy of reactor antineutrino spectrum predictions, Mueller combined updated information from nuclear databases for dominant isotopes with the ILL measured electron spectra [44]. This, combined with Patrick Huber's higher order corrections using the conversion method [45], gives what is called the "Huber+Mueller" model.

The detectable IBD spectrum is determined by the $\bar{\nu}_e$ energy spectrum and the IBD cross section. The IBD cross section calculated by Beacom and Vogel [46] is commonly used. Figure 2.2 shows how the detector flux and cross sections at various energies produce the detectable IBD spectrum from a sample 12-ton fiducial mass detector 0.8 km from a 12-GW$_{th}$ power reactor. Most neutrinos generated in nuclear reactors have energies below the threshold value in Equation 2.4 and are undetectable from this process [47].

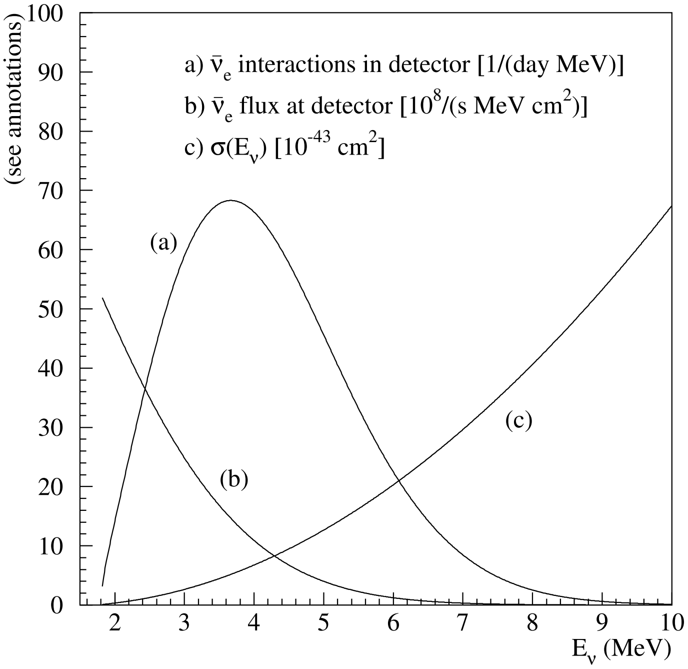

Figure 2.2: A sample reactor flux (b), IBD cross section (c), and detectable IBD spectrum (a) vs energy, as measured by a 12-ton fiducial mass detector located 0.8 km from a 12-GW$_{th}$ power reactor [12].

2.3 Reactor Antineutrino Measurements

One of the major successes of reactor neutrino experiments has been the precise measurement of the θ_{13} mixing angle. Measurements from accelerator experiments showed the optimal disappearance distance (using Equation 1.21) was around 2 km. In order to be sensitive to the anticipated small θ_{13}, the maximum disappearance to measure θ_{13} would be $\sim$1%, much smaller than reactor flux calculation uncertainties. To lessen the effects of reactor flux uncertainties, experiments built multiple detectors to measure neutrino flux very close to the reactor, and around an optimal oscillation detection distance. By comparing the two detector site results, experiments could measure deviations in the $1/r^2$ in rate, greatly reducing the uncertainty from reactor neutrino flux. This method was used by the Daya Bay [32], RENO [48] and Double CHOOZ [49] experiments in the early to mid-2010s.

The results of these experiments have uncovered some discrepancies in the calculated and measured antineutrino flux and spectra. They determined the antineutrino energy spectrum with unprecedented statistics by detecting millions of IBD events. Figure 2.3 shows their measured antineutrino energy spectrum, in which all three exhibit an excess of events in the 4-6 MeV region compared to the Huber+Muller model [32, 50, 51]. Since previous experiments measuring the spectra from ^{235}U, ^{239}Pu, and ^{241}Pu did not show a similar feature [52, 53, 54, 55, 56], a possible explanation is that the bump is from the ^{238}U fast-neutron fission [31, 57]. A measurement by Haag *et al.* in 2014 [58] did not show this "bump" in the β spectrum of ^{238}U fast neutron induced fission, casting doubt on ^{238}U being responsible for this feature. Without conclusive evidence, precision measurements of fission isotopes are necessary.

The Daya Bay collaboration observed a correlation between the reactor core fuel composition and the measured changes in the reactor antineutrino flux and energy spectrum. Daya Bay measured the successive β decays from neutron rich fission fragments of the fissionable isotopes ^{235}U, ^{238}U, ^{239}P and ^{241}P, with ^{235}U and ^{239}P being the two dominant fission isotopes. By correlating changes in fuel fraction to total neutrino flux, they found the neutrino yield from ^{239}Pu agreed with predictions from the Huber model, but the yield from ^{235}U $\sim$8% lower than predictions [60].

In addition to the antineutrino spectra from reactors, the reactor experiments were able to compare the neutrino flux measurements to predictions. Anomalous results in reactor electron antineutrino flux measurements suggest that the current understanding of flavor change and mixing in the three neutrino model is incomplete. The Daya Bay experiment calculated the reactor neutrino yield with all 6 of their detectors (3 near, and 3 far), shown in Figure 2.4. The average of the three near detectors is shown as the gray line, extended through the far detectors as a dotted

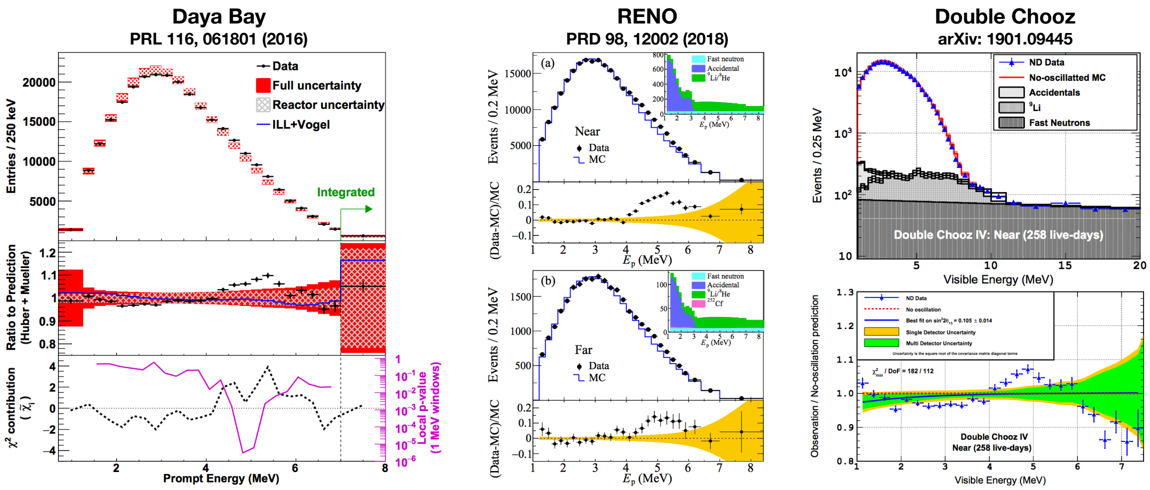

Figure 2.3: Comparison of measured antineutrino energy spectra observed from Daya Bay [32], RENO [48] and Double CHOOZ [49], showing more neutrinos in the 4-6 MeV energy range than predicted based on the Huber+Muller model [59].

gray line, with a gray band for systematic uncertainties. While the individual detectors from Daya Bay are in agreement, there is significant disagreement between these results and the Huber+Mueller model, although there is concern over underestimations of the systematic uncertainties [35]. Figure 2.5 shows an observed 6% deficit in the absolute flux of world-wide reactor neutrino measurements compared to recent predictions, referred to as the “Reactor Antineutrino Anomaly” (RAA) [61, 44, 45].

One explanation for the RAA deficit is the existence of a fourth generation “sterile neutrino,” with $\Delta m^2_{14} \sim \mathcal{O}(\mathrm{eV}^2)$ and an oscillation wavelength $\mathcal{O}$(meters) [62]. Sterile neutrinos would only interact via the gravitational force, and not participate in weak interactions, so previous experiments were not sensitive to detecting them. One approach to identifying the existence of these sterile neutrinos is to make precise measurements of neutrino deficits consistent with the above parameters, with a detector distance from the reactor on the order of the oscillation wavelength.

While searching for neutrino oscillations in the $\bar{\nu}_\mu \rightarrow \bar{\nu}_e$ channel, the Liquid Scintillator Neutrino Detector (LSND) Experiment at Los Alamos National Laboratory measured an excess of low energy events consistent with a fourth generation sterile neutrino with mass splitting of $|\Delta m^2| \sim 1$ eV^2 [63]. To test the same L/E region of this anomaly with additionally the $\nu_\mu \rightarrow \nu_e$ channel, Mini Booster Neutrino Experiment (MiniBooNE) at Fermilab confirmed the excess of events with some overlap in the allowed parameter regions for the existence of 3 active neutrinos and 1 sterile

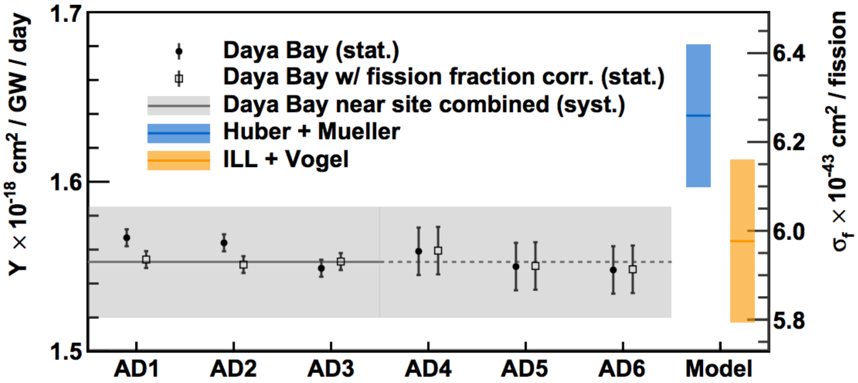

Figure 2.4: Rate of reactor antineutrino candidates in the six detectors used by Daya Bay [32]. Also shown are the rates predicted by the Huber+Mueller (blue) and ILL+Vogel (orange) models.

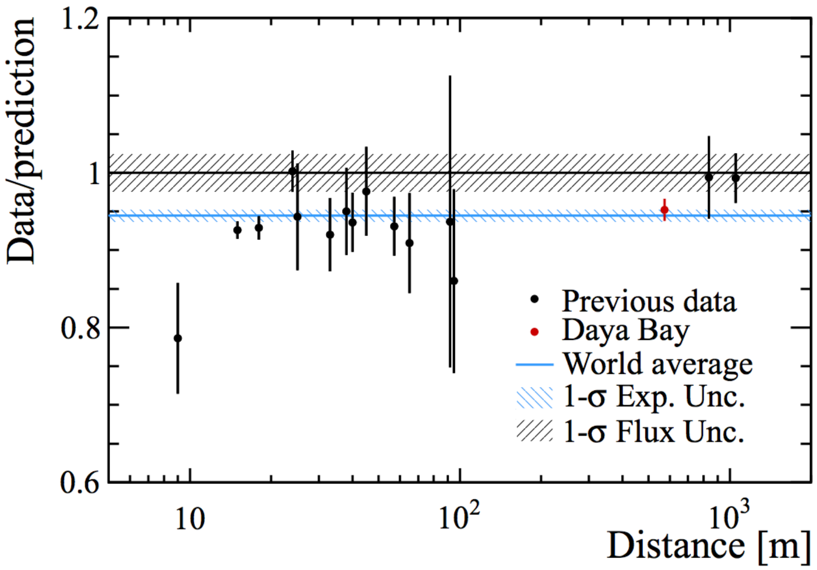

Figure 2.5: Reactor neutrino flux measurements, showing a ∼5-6% deficit from the Huber+Mueller prediction [61].

neutrino state (the "3+1" model) [64]. Using intense ^{51}Cr and ^{37}Ar sources, the solar neutrino detectors GALLEX [17] and SAGE [16] observed ~24% ν_e disappearance, referred to as the Gallium anomaly, which can also be explained by a sterile neutrino with $\Delta m^2 \sim 1$ eV^2 [65]. Figure 2.6 shows a global fit of the sterile neutrino 3+1 model using these experiments to give oscillation restraints of $\Delta m^2_{14} > 1.5\text{eV}^2$ and $\sin^2(2\theta_{14}) = 0.14 \pm 0.08$ [66].

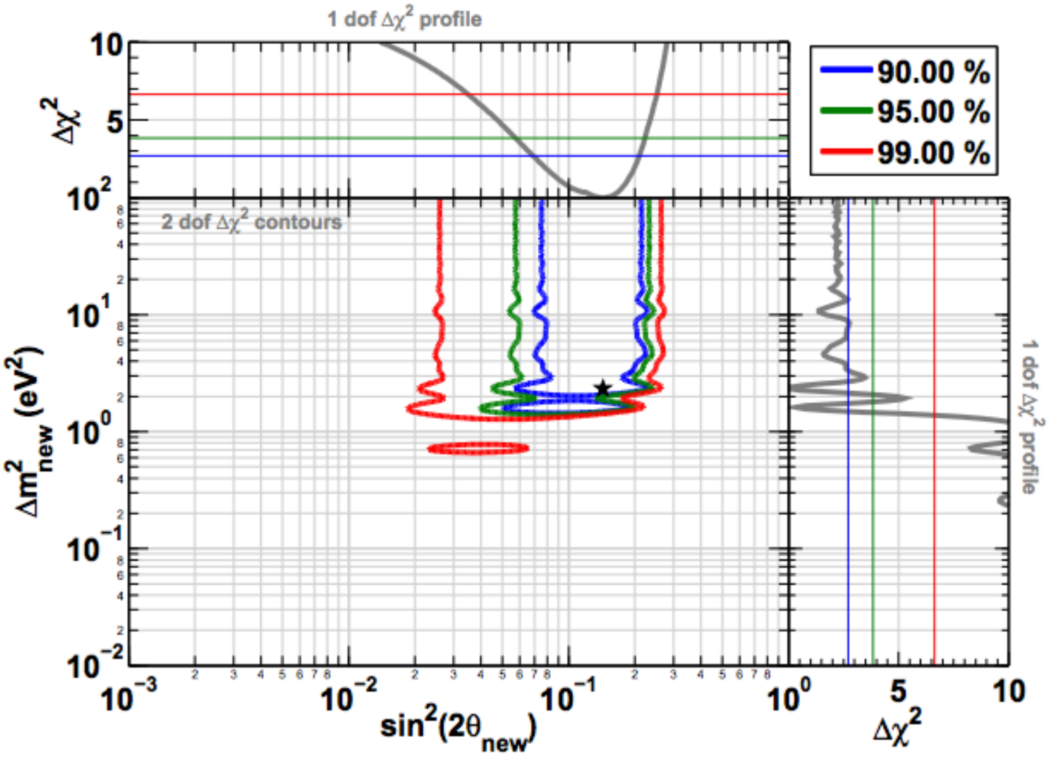

Figure 2.6: Regions allowed in Δm^2_{14} and $\sin^2(2\theta_{14})$ (listed as Δm^2_{new} and $\sin^2(2\theta_{new})$)from ν_e and $\bar{\nu}_e$ disappearance experiments mentioned in text. The black star represents the best fit point suggesting $|\Delta m^2_{14}| > 1.5$ eV^2 and $\sin^2(2\theta_{14}) = 0.14 \pm 0.08$ at the 95% confidence level [66].

We have now outlined the RAA and other discrepancies in neutrino physics. In order to isolate the cause or sources of the "bump" seen in the antineutrino energy spectra from Daya Bay, Double CHOOZ and RENO, direct measurements of the reactor neutrino flux of single fission isotopes' spectra are necessary. Since the Daya Bay analysis found a discrepancy in the neutrino yield for ^{235}U between their measurements and the Huber model, HEU reactors are ideal for this due to their high concentration of antineutrinos from ^{235}U. Additionally, a short baseline detector experiment located within meters of a research reactor is ideal to simultaneously probe eV-scale sterile neutrinos with a meter-scale oscillations. In order to test short baseline oscillations, a detector must be sensitive to the total reactor flux but also be able to identify oscillations patterns in energy and distance from reactor. Uncertainties of new experiments would need to be at the level of a few percent for definitive results. Between this and the oscillation parameters in question, the distance between the neutrino source and detector should be less than 15 m, since distances farther away would yield a lower flux and the oscillatory behavior would be washed out [31].

CHAPTER 3

THE PROSPECT EXPERIMENT

While the Standard Model of particle physics includes only three neutrino flavors, recent anomalies outlined in Chapter 2 have hinted at a potential "sterile" neutrino that detectors are insensitive to measuring directly. The Precision Reactor Oscillation and Spectrum Experiment, PROSPECT, aimed to perform a precise measurement of the antineutrino spectrum produced by the High Flux Isotope Reactor (HFIR) at Oak Ridge National Lab (ORNL), in addition to probing meter scale oscillations at short baselines (7-9 m) in search of a sterile neutrino state [34, 59]. The detector's close proximity to the reactor is ideal for searching for oscillations arising from $\sim$1 eV sterile neutrinos, as well as providing a relatively large electron antineutrino flux from the reactor core. PROSPECT's use of a segmented detector with ^{6}Li doped liquid scintillator (LiLS) efficiently detected reactor antineutrinos through the inverse beta decay reaction and provided excellent background rejection [34]. Constructed in the mid-1960s, HFIR operates at 85 MW$_{th}$ and uses highly enriched ^{235}U as fuel [67]. The first oscillation and spectrum results from PROSPECT can be found in Ref [68, 69]. In this chapter, we will describe the experimental setup and reactor site, in addition to some design and construction details of the PROSPECT detector.

3.1 The High Flux Isotope Reactor

The HFIR site at ORNL was chosen for a number of advantageous parameters. One of these advantages of the HFIR core is that it is compact, lowering the uncertainty of neutrino travel distances. A non-point source of neutrinos smears the origin, making a given position in the detector a distribution of neutrino travel distances. The compactness of the HFIR core reduced this systematic to the point that it was not significant. Figure 3.1 shows the cylindrical, compact size HFIR core ideal for constraining the uncertainty in neutrino baselines.

The HEU research fission reactor at HFIR has an average ^{235}U enrichment of ∼93%, and the contribution of neutrinos from ^{235}U throughout a given cycle is >99%. Since HFIR operates in relatively short reactor cycles (20-30 days) in order to maintain a high ^{235}U enrichment, the effects of an evolving fuel contribution breakdown are negligible [70].

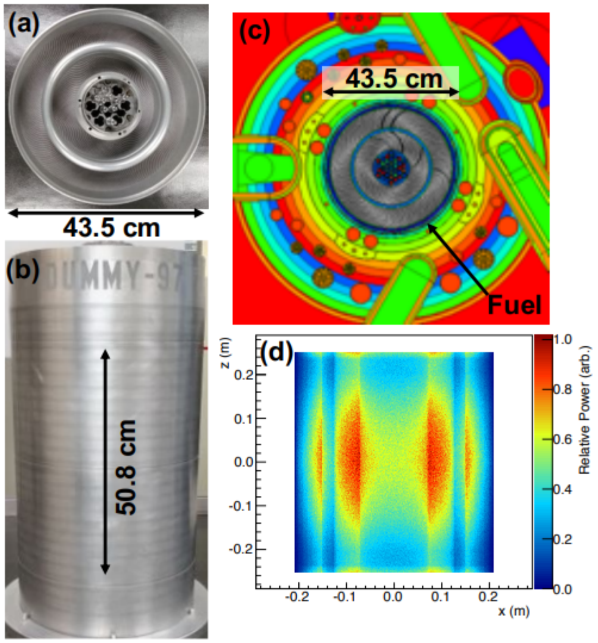

Figure 3.1: Model of the HFIR core [70]. (a) and (b) show the diameter and height. (c) shows the HFIR core location from simulation, and (d) is a projection of the fission power density of HFIR [59].

3.1.1 On-site Backgrounds

In order to sit within short baseline distances of the HFIR core, the PROSPECT detector needed to be near ground level, making it sensitive to cosmic ray backgrounds with minimal overburden. High energy cosmogenic events can produce signals similar to IBD candidates in the detector. In addition, the nearby reactor also generates background neutrons and gamma rays. Additionally, research below the detector site uses neutron beam lines which produces background signals in the PROSPECT detector.

Some of these backgrounds provide coincident events that mimic the IBD signature signal described in Section 3.2. One example is a high energy neutron that scatters on carbon, ^{12}C(n,n')^{12}C*, during thermalization, which produces a $\sim$4.4 MeV gamma ray, followed by a neutron capture. Measurements and studies before detector construction indicated that appropriate passive shielding suppresses reactor related backgrounds to a point where a measurement was feasible. Measurements when the reactor was off were used for cosmogenic background subtraction during analysis. Section 3.2.5 discusses the passive shielding system of the PROSPECT detector, as we now turn to a detailed description of the PROSPECT detector. More information on the background measurements can be found in [71, 72, 73].

3.2 PROSPECT Antineutrino Detector

The PROSPECT Antineutrino Detector (AD) is a single volume filled with ^{6}Li loaded EJ-309 liquid scintillator (LiLS) separated optically by highly reflective panels, forming a 14 wide by 11 high grid of 154 elongated segments. Figure 3.2 shows the detector grid and size relative to the detector core. In Figure 3.3, we see the schematic of one of the individual detector segments. The active area of each segment between the PMT housing faces is approximately 117.6 cm long, and 14.5 cm square along the cross section. At either end of each segment sits a photomultiplier tube (PMT) in a specially designed housing. Due to manufacturing lead times that did not coincide with the experiment's schedule, two types of PMTs (240 Hammamatsu R6594 SEL and 68 ADIT Electron Tubes brand) were used in the detector, with each segment having identical PMTs on either end. Electron Tubes (ET) are only used in the peripheral segments as shown in Figure 3.5.

When the reactor antineutrinos enter the detector, they interact with protons as described above via inverse beta decay (IBD). The neutrons produced from IBD then capture on either ^{6}Li atoms or protons:

$$\mathrm{n} + {}^{6}\mathrm{Li} \rightarrow \alpha(2.73\ \mathrm{MeV}) + {}^{3}\mathrm{H}(2.05\ \mathrm{MeV}) \tag{3.1}$$

$$\mathrm{n} + \mathrm{H} \rightarrow {}^{2}\mathrm{H} + \gamma(2.2\ \mathrm{MeV}). \tag{3.2}$$

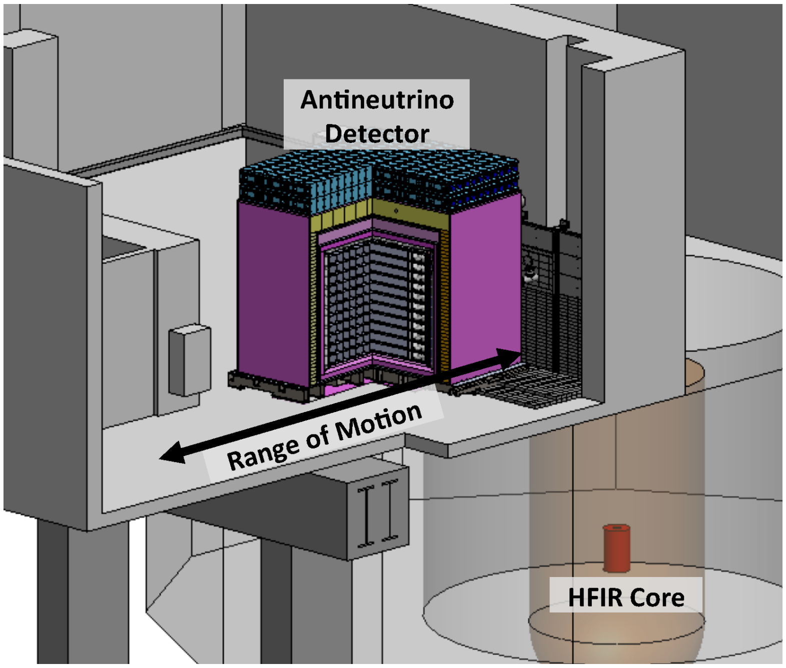
Antineutrino Detector
Range of Motion
HFIR Core

Figure 3.2: PROSPECT AD schematic and positioning relative to HFIR Core at Oak Ridge National Lab. [59]

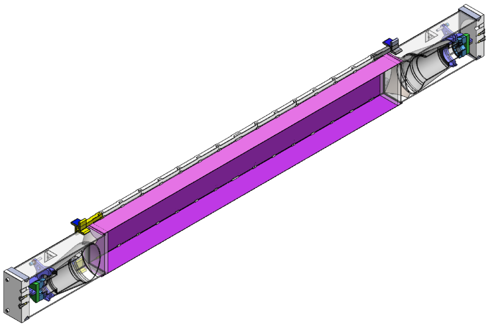

Figure 3.3: Cross section of one segment in the PROSPECT AD grid, comprising of two photomultiplier tube housings on either end (Section 3.2.2), and reflective panels surrounding the active segmented volume (Section 3.2.4).

These neutron capture with a measured lifetime of ~50 μs, forming a delayed energy signal that is quenched in the LiLS, meaning the detectable energy seen as scintillation light is decreased by a nonlinear factor. The α and triton pair produced from nLi captures deposit their energies in very close proximity and time to each other. Within the scintillator, this appears as one energy deposit. Since the α and triton are both heavy particles, their total energy gets quenched down from 4.78 MeV to approximately 0.55 MeV of visible scintillation. Figure 3.4 shows a diagram of the IBD and prompt-delay detection. The neutron captures on ^{6}Li approximately four times as often as on protons.

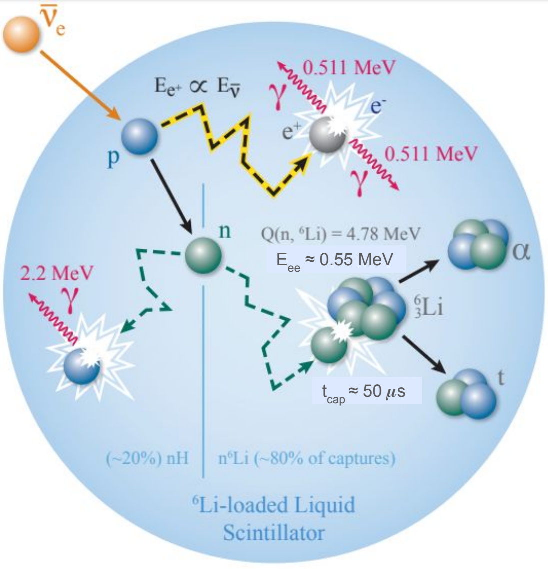
$\overline{\nu}_e$
$E_{e^+} \propto E_{\overline{\nu}}$
p
0.511 MeV
γ
e⁻
e⁺
0.511 MeV
γ
n
Q(n, ⁶Li) = 4.78 MeV
$E_{ee} \approx 0.55$ MeV
α
2.2 MeV
γ
$^6_3$Li
t
$t_{cap} \approx 50\ \mu$s
(~20%) nH
n⁶Li (~80% of captures)
⁶Li-loaded Liquid Scintillator

Figure 3.4: Illustration of IBD, the e^+e^- annihilation prompt signal, and the neutron capture delay signal, described in text.

The signals from the alpha and ^{3}H from neutrons capturing on ^{6}Li occur within ~10 μm and appear as one energy deposit in the PROSPECT detector. This is in contrast to the popular use of Gd as the neutron target. Gd has a higher capture cross section, but produces multiple MeV scale gamma rays, which would travel multiple segments in various directions in the distance of the PROSPECT AD detector before depositing their energy, which makes determining the IBD location less precise [32]. This time correlated prompt-delay signature, along with the pulse shape discrimination produced from the signals, creates an effective cut on data to eliminate random accidental backgrounds.

The AD shielding consists of water bricks and polyethylene for shielding against outside neutrons, a lead casing, and an inner neutron shield to reduce neutron spallation from the lead outer casing. Many of these features are discussed in more detail in the following sections. Construction concluded in Winter 2017 and data-taking began in early 2018.

3.2.1 Scintillator

PROSPECT required a scintillator with good pulse shape discrimination (see Section 3.2.6) for background suppression, and good energy resolution through high light yield. HFIR safety regulations also require the scintillator be low toxicity and non-flammable. A subgroup of the PROSPECT collaboration at Brookhaven National Lab (BNL) and the National Institute of Standards and Technology (NIST) developed a novel ^{6}Li-loaded liquid scintillator (LiLS) with a commercial EJ-309 by adding a surfactant to the base scintillator, allowing the loading of an enriched (95% ^{6}Li) LiCl aqueous solution in a thermodynamically stable and uniform microemulsion. They determined a final ^{6}Li loading fraction of $0.082\pm0.001\%$ by mass, with an energy resolution of $5\%/\sqrt{E(\text{MeV})}$. Additionally, $\sim$0.5 Bq of ^{227}Ac was uniformly distributed throughout the scintillator to monitor the relative volumes of each segment. The PROSPECT collaboration published details on scintillator production, found in Ref. [74]. Characterizing and monitoring the ^{6}Li doping fraction during the lifetime of the PROSPECT detector is the focus of Section 4.4.1 of this thesis.

3.2.2 PMT Housings

The PROSPECT AD uses a total of 240 Hamammatsu R6594 SEL PMTs and 68 ADIT Electron Tubes (ET) 9372KB PMTs, arranged as in Figure 3.5. Each of these 308 PMTs are contained in a liquid-tight, rectangular acrylic housing with a 13 mm thick ultraviolet transmitting acrylic window. Figure 3.6 shows a diagram of the PMT housing design. Between the PMT bulbs and housing windows are conical reflectors to improve light collection efficiency in corners. The housings were filled with optical grade mineral oil for optical matching to increase the transmission of scintillation light. The housings are mounted on an acrylic support structure which holds them in place. More details on the PMT housings and design can be found at ref [59].

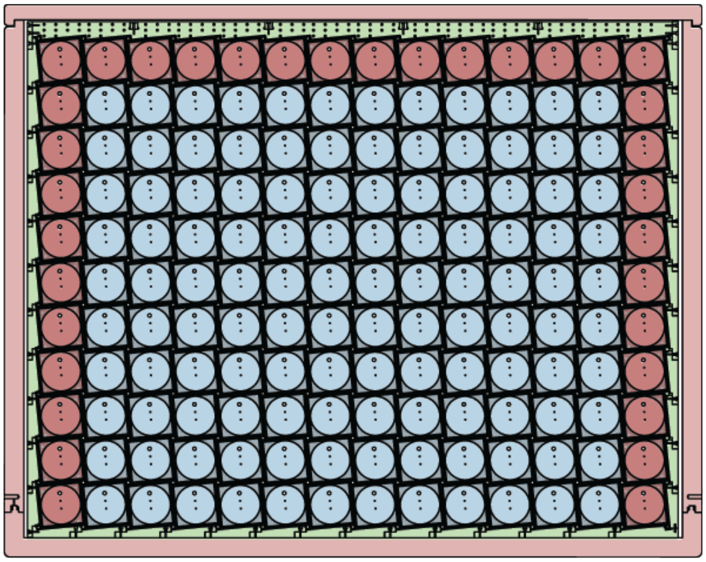

Figure 3.5: PROSPECT detector cross section showing the segments using the 68 ET PMTs (red) and 240 Hamamatsu PMTS (blue).

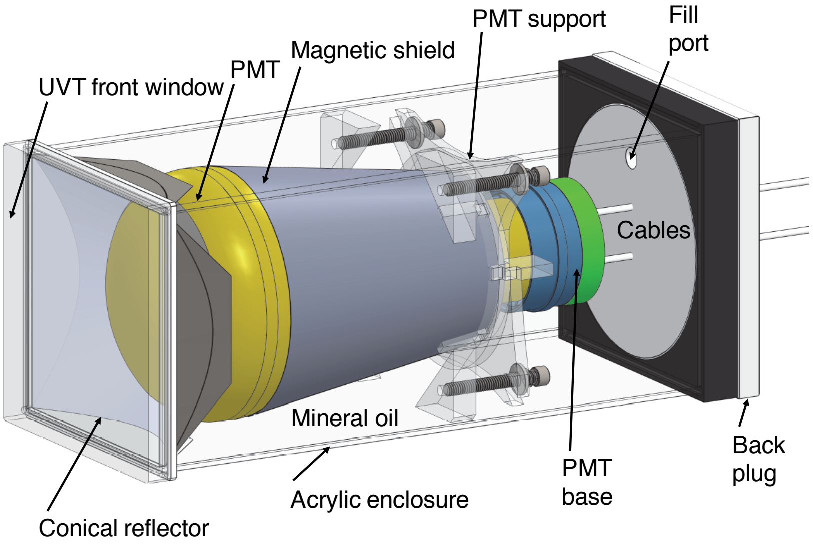
PMT support
Fill port
Magnetic shield
PMT
UVT front window
Cables
Mineral oil
Back plug
PMT base
Acrylic enclosure
Conical reflector

Figure 3.6: Detailed schematic of PMT housing modules described in text.

3.2.3 Segmentation

Similarly to how the θ_{13} experiments utilized multiple detectors in order to eliminate the reactor flux uncertainties, the PROSPECT detector utilizes a segmented design in order to make a flux independent oscillation measurement. The detector active volume is defined by an inner acrylic containment tank, and is separated by low mass, reflective optical separators held together by 3D printed hollow support rods, forming a 14×11 grid of optically separated segments. Each segment has a photomultiplier tube (PMT) housing on each end. When particles interact in the scintillator, the resulting scintillation in that segment is registered by the two PMTs at either end, with negligible cross talk between segments by design. While the scintillator provides ^{6}Li targets for neutron capture with localized nLi decay products, the segmentation provided position information for both prompt and delay signals and allowed a more distinct topology for IBD events.

3.2.4 Optical Lattice and Supports

The detector active volume is 1.176 m wide × 2.045 m long × 1.607 m tall. The optical grid consists of low-mass, highly reflective opaque optical separators held in place by 3D printed hollow support rods, which allows for the internal radioactive source calibration system (Section 3.3). Optical separator panels have a carbon fiber center, covered with a specularly reflective film and an optically clear adhesive film. A fluorinated ethylene propylene (FEP) film coats the panel to provide compatibility with the LiLS. The panel reflects more than 99% of photons above 400 nm, at normal incidence. In addition to providing structural support, the carbon fiber sheet eliminates light cross-talk between segments.

Figure 3.7 shows the "pinwheel" support rods. Multiple pinwheel segments are strung onto teflon tubing for use in the calibration system, or acrylic rods. Rods contain multiple tabs to grip the optical separator panels. The total mass of the optical lattice and support rods comprises less than 3% of the total detector target mass. The design of the pinwheel and lattice system tilts each segment by about 5.5 degrees. Figure 3.8 shows a diagram of all these aspects in relation to a single segment's construction. More details including the optical lattice system design, production can be found in Ref. [75].

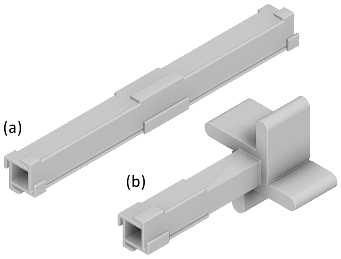

Figure 3.7: Pinwheel types used in the optical support lattice in the PROSPECT AD. (a) central pinwheel - three tabs per side hold the optical separator in place. (b) end pinwheel - spacer arms separate the PMT housing bodies and support the pinwheel string.

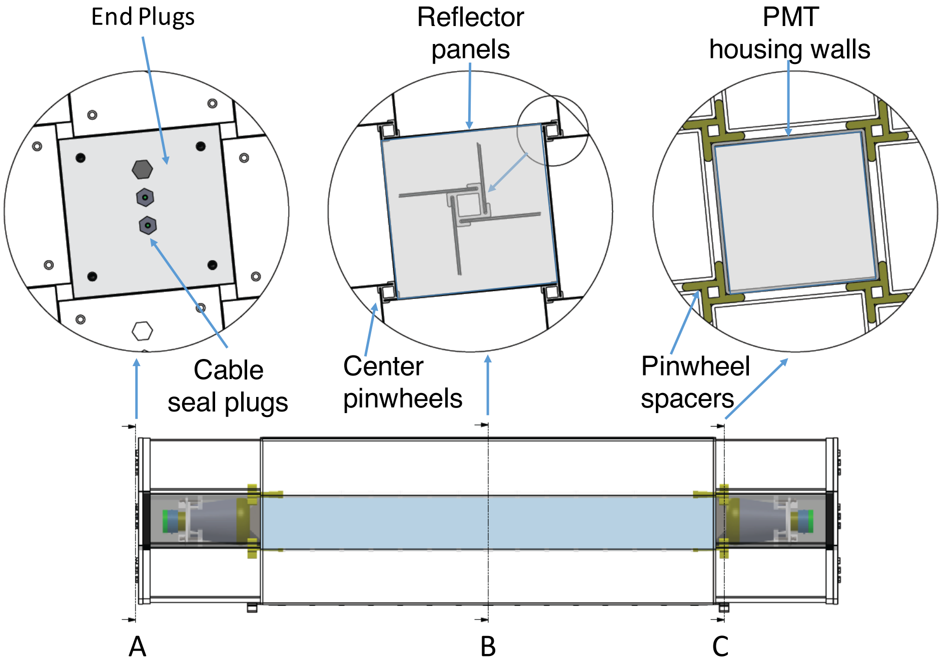
End Plugs
Reflector panels
PMT housing walls
Cable seal plugs
Center pinwheels
Pinwheel spacers
A
B
C

Figure 3.8: Diagram of a single PROSPECT segment. PMT housings are inserted into the optical grid on each end. (a) PMT housing with end plugs and cables out. (b) center pinwheels and optical separators, resulting in the 5.5 degree tilt. (c) end pinwheel spacer arms against adjacent segments.

3.2.5 Shielding

Background measurements at HFIR, in combination with prototypes and simulations, guided the design of the passive shielding of the PROSPECT AD. Backgrounds that mimic the IBD selection could come from neutron interactions that produce a gamma ray, such as from nC* collisions, or multiple incident neutrons, where one captures on hydrogen that produces a 2.2 MeV gamma ray, preceding a second neutron capture on ^{6}Li. Some of these backgrounds, and how they are handled in the analysis, are discussed in Section 4.1. In order to suppress high energy cosmic neutrons, the top of the detector is layered with hydrogenous material, in addition to layers of 0.025 m thick lead and 5% borated polyethylene (BPE) surrounding all sides of the detector. Figure 3.9 shows the various layers of shielding along with the inner detector.

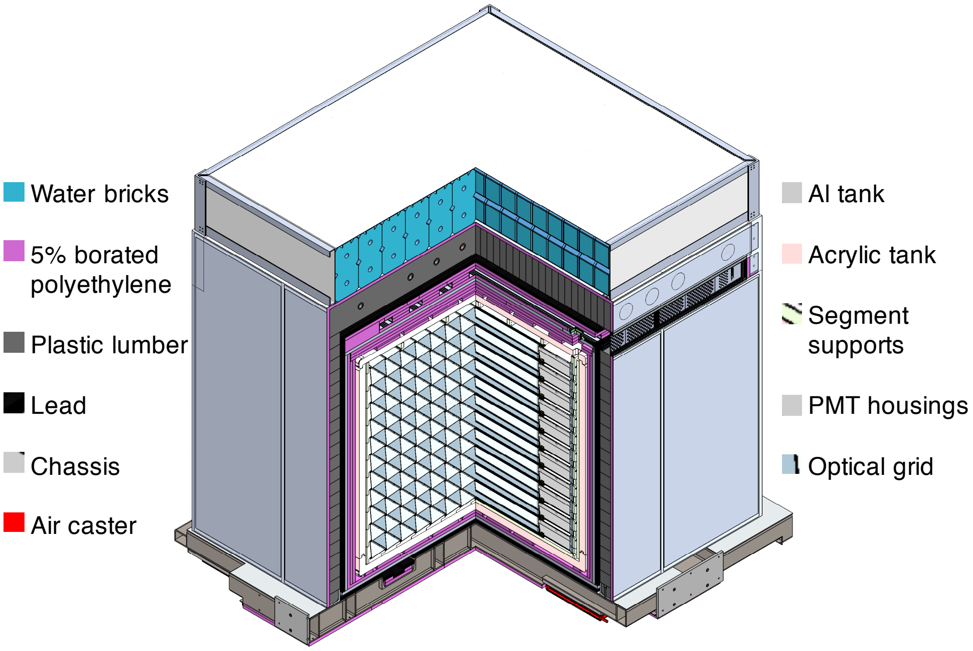

Figure 3.9: Cross section of the design of the PROSPECT AD, showing the inner volume and the various layers of shielding.

A secondary containment vessel made of aluminum and inside the outer shielding is sealed at the top of the detector to control the gaseous environment around the detector. Sheets of BPE and demineralized water between the aluminum tank and the inner acrylic tanks absorb externally originated thermal neutrons. This secondary containment vessel is supported by walls of interlocking 0.025 m thick lead bricks, with lead bricks of the same thickness underneath. Further details on the detector containment vessels and shielding can be found at Ref [59].

3.2.6 Pulse Shape Discrimination

In order to distinguish the identity of particles in the PROSPECT AD, it is useful to incorporate an analysis of particle pulse shape discrimination (PSD). When a charged particle travels through scintillator, some of its kinetic energy is converted into flourescent energy. For many organic scintillators the converted energy is dependent on both the particle type and its energy. In such cases, the response to electrons is approximately linear for particle energies above approximately 125 keV, and the response to heavier and thus slower charged particles (such as protons and alpha particles) is less for equivalent energies and is nonlinear to much higher energies [76]. Figure 3.10 shows the difference in response between electrons and protons for an example scintillator. This response produces the signals seen in Figure 3.11 for neutron recoils and Compton scatters in the PROSPECT scintillator.

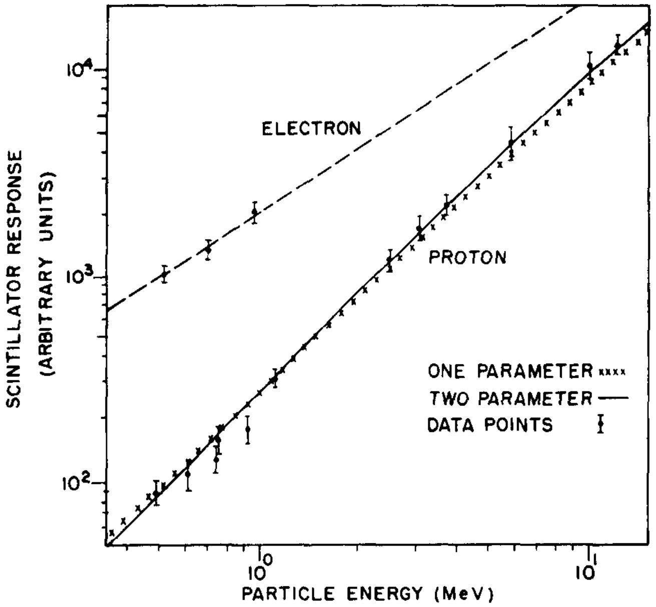

Figure 3.10: Light yield for a common scintillator when excited by electrons and protons [76].

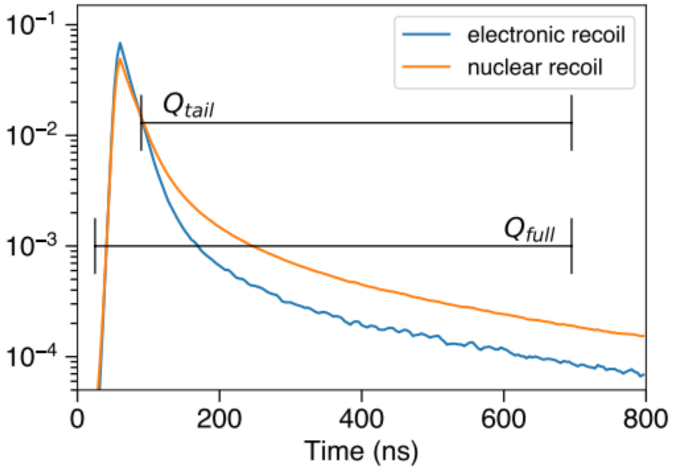

Figure 3.11: The total components of the scintillation as light yield (normalized y axis) in time for neutron recoils and Compton scatters from a PROSPECT prototype. Depending on the exciting particle, more of the total light yield will be in the delayed fluorescence [77].

The light produced in these scintillators comprises of a prompt and delayed fluorescence. These can be represented by the sum of two exponential decays - the fast and slow components of the scintillation. The prompt decay time is only a few nanoseconds, whereas the delayed decay time is generally hundreds of nanoseconds. The fraction of light in the delayed fluorescence is dependent on the type of exciting particle, as seen in Figure 3.11. Differentiating between particles by finding the fraction of light in the slow component is referred to as pulse shape discrimination [76]. PROSPECT defines PSD as

$$\mathrm{PSD} = \frac{\int_{\mathrm{tail\ start}}^{\mathrm{tail\ end}} \mathrm{Q(t)dt}}{\int_{\mathrm{total}} \mathrm{Q(t)dt}} \tag{3.3}$$

where the integral of $Q(t)$ is the PMT current and the integration bounds on the pulse shape are determined by optimization, demonstrated in Figure 3.11. Using PSD in combination with event energy provides good particle distinction, particularly above 0.5 MeV, as shown in Figure 3.12.

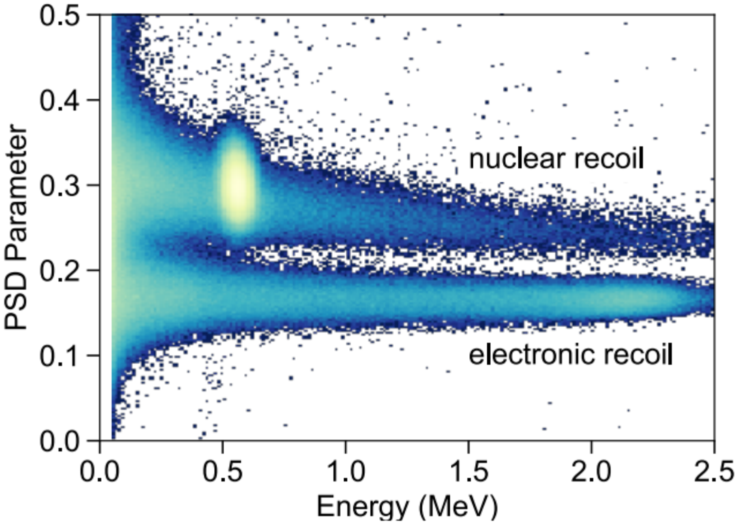

Figure 3.12: Event PSD (vertical axis) and Energy (horizontal axis) from a distribution of ^{252}Cf neutron and gamma ray events from a PROSPECT prototype. Neutron-proton recoils contribute to the top 'neutron recoil' band, while gamma ray compton scatters contribute to the lower band. The distribution of nLi captures can be seen at PSD = 0.3 with energy near 0.55 MeV [77].

3.2.7 Data collection

Data are collected from the detector through 21 CAEN V1725 Waveform Digitizer (WFD) modules. If both PMTs register a signal exceeding a threshold signal within 64 ns of each other, all the WFD channels are triggered and all channels above a second, lower threshold level trigger record a waveform of 148 samples at a frequency of 250 Hz. The 308 PMTs readouts are handled by 21 WFD modules. Data are transfered from the WFD modules to disks on two Data Aquisition (DAQ) controller computers, and then is immediately transferred to a multi-disk array for temporary storage, with permanent storage located at Lawrence Livermore National Lab. Details on the DAQ system can be found at Ref [59].

3.2.8 Position Reconstruction

The detector segmentation allows for a discrete determination of an event's (x, y) coordinates. For an IBD event, the segment that registers the highest energy for the prompt signal is considered the IBD location. The z coordinate, along the segment length, is reconstructed using a linear combination of the relative timing between the two PMTs in a segment (dt) and their relative light yields, with the combination of these chosen to minimize uncertainty. High energy cosmogenic events provide a large and relatively uniform set of data to calibrate the position curves in the detector. Since the pinwheel tabs block the reflective panels, there is a loss of scintillation light near these pinwheels. Figure 3.13 shows the high energy pulse rate vs the timing difference dt between two PMTs in a segment. Noticeable peaks arise with a periodicity correlating to the spacing between the pinwheel tabs from Figure 3.7. This is fit to an "M" curve, $M(dt)$ shown in Figure 3.13, and then the sinusoidal structure is fitted by

$$n(dt) = M(dt)\left[1 + k\cos\left(\frac{2\pi}{\delta}(a\,dt + b\,dt^3)\right)\right] \tag{3.4}$$

where $n(dt)$ is fit to data, and the average spacing between pinwheel tabs, $\delta = 78.5$ mm, and k, a, and b are fit parameters used to reconstruct the detector position [78]. Figure 3.14 shows the resulting position calibration with fit parameters a and b as

$$z(dt) = a\,dt + b\,dt^3. \tag{3.5}$$

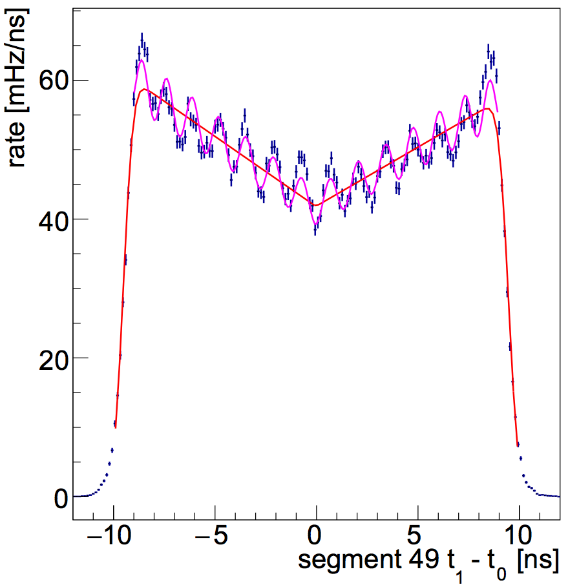

Figure 3.13: Sample high energy cosmogenic rates vs timing difference between dt between PMTs. Data are plotted in blue, with red fit curves as described in text. The spacing between data peaks correlates to the pinwheel tabs in the detector [78].

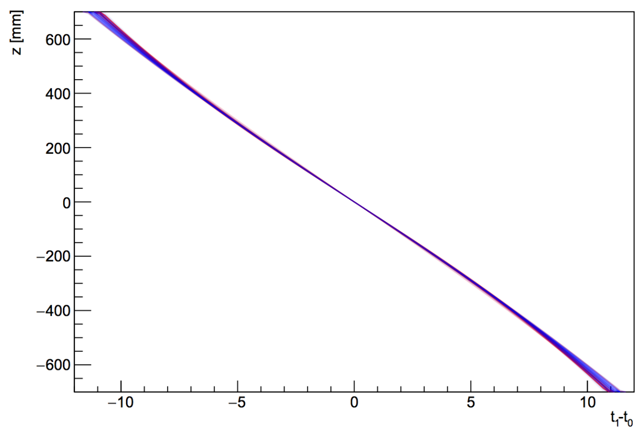

Figure 3.14: Reconstructed position, z as a function of the dt between segment PMTs for high energy cosmogenic uniform events[78].

3.2.9 Energy Reconstruction

Since the light collection varies with the distance from each PMT, the location of each signal has an effect on the energy calibration scheme. The left panel of Figure 3.15 shows the relative light collection efficiency for both PMTs as a function of the energy deposit reconstructed position. To correct this dependence on signal location, we define

$$R = S_1/S_0 \; ; \; S = \sqrt{S_0 S_1} \tag{3.6}$$

where S_i is the integral of the signal from PMT i for a given segment. Figure 3.16 shows the nLi capture peak in terms of S and PSD. While $\ln(S_1/S_0)$ was found to be roughly linear with dt for each segment as shown in Figure 3.16, $S(dt)$ showed a quadratic trend in the nLi capture peak along the segment length as shown in the right panel of 3.15. The relative light collection efficiency for each PMT in terms of R and S is then modeled by the light collection curve from the opposite PMT as

$$\epsilon_0(dt) = \frac{S(dt)}{S(0)}\sqrt{\frac{R(dt)}{R(0)}} \; ; \; \epsilon_1(dt) = \frac{S(dt)}{S(0)}\sqrt{\frac{R(0)}{R(dt)}} \tag{3.7}$$

where $dt = 0$ is defined as the time difference between two PMT signals from a source at the center of a segment.

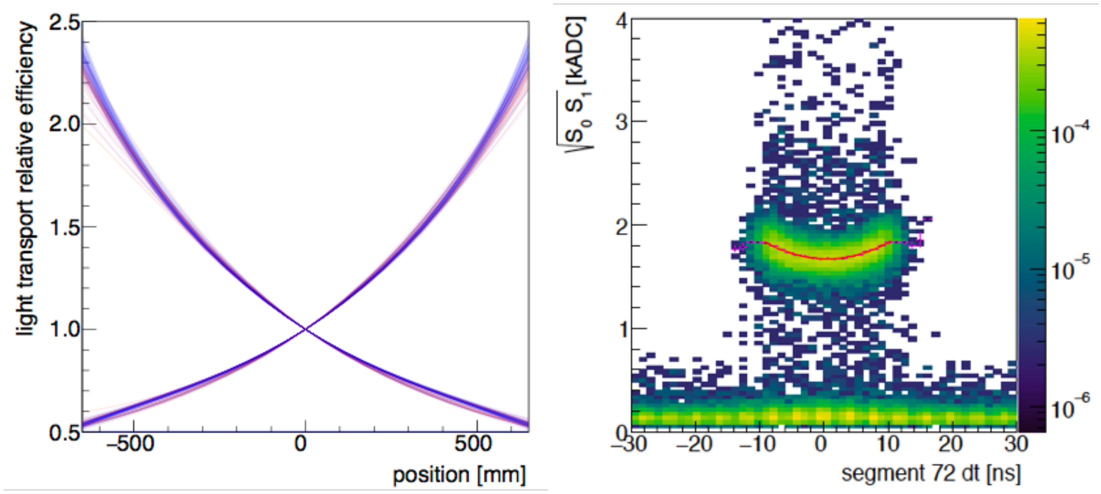

Figure 3.15: Left: Near exponential light transport efficiency curves for each PMT in a segment, as a function of energy deposit location. Right: nLi events in one segment vs dt, with a quadratic fit in red.

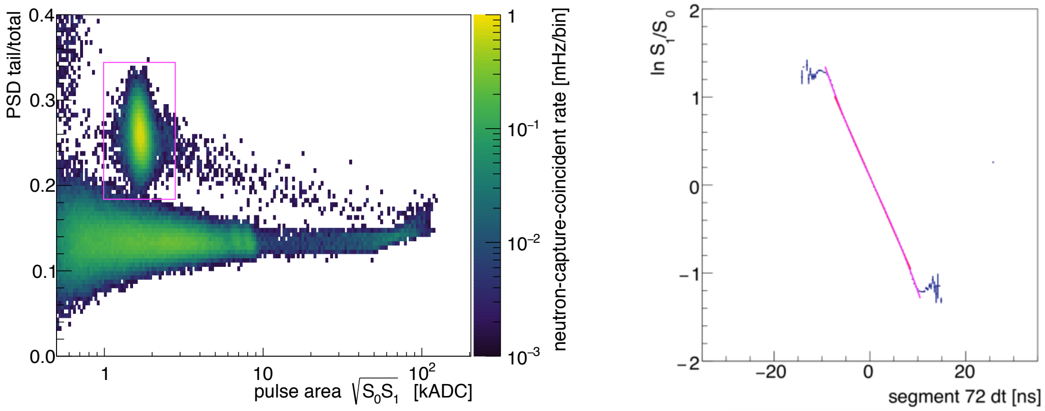

Figure 3.16: Left: Example of pulse area and PSD for neutron capture coincident events. The magenta rectangle outlines the clear neutron capture on ^{6} energy peak isolated in “energy” and PSD. Right: Ratio of the waveform integrals from two PMTs in a sample segment. The magenta line is a cubic polynomial fit that is used to correct the position dependent energy reconstruction [79].

The reconstructed event energy is then calculated as

$$E = \frac{N_0 + N_1}{\epsilon_0(dt) r_{E,0} + \epsilon_1(dt) r_{E,1}} \tag{3.8}$$

where $r_{E,i}$ is the resolution for PMT i fixed to 250 photoelectrons per MeV, and N_i

is the average number of detected photoelectrons by PMT i as

$$N_i = r_{E,i}\frac{S_i}{g_i} \tag{3.9}$$

where the gain factors g_i are determined to correct for energy variations over time, defined as

$$g_0 = \frac{S(0)}{\sqrt{R(0)}E_{nLi}} \; ; \; g_1 = \frac{S(0)\sqrt{R(0)}}{E_{nLi}} \tag{3.10}$$

where E_{nLi} is the energy from nLi. The energy scale calibrations are further adjusted using scaling factors determined by simulations with gamma sources and cosmogenic ^{12}B signals. This provides a scale to convert the recorded signal from Analog-to-Digital Converter (ADC) units, to MeV.

Particles with enough energy can travel through multiple segments in the detector and register multiple energy deposits. The particle energy is reconstructed by counting the light scintillation collected by the PMTs at either end of the segment. When multiple energy deposits register in separate segments with less than 20 ns between deposits, the signals in all segments are grouped together into a *cluster*. The total event energy is determined by summing over the cluster energies. The position for this type of event is taken as the position of the largest energy deposit from the cluster.

Measured energy in PROSPECT is sometimes reported in terms of electron-equivalent energy (MeVee = MeV electron equivalent), which indicates the quoted energy is calibrated to the scintillation light level of an electron. The actual energy of the event will depend upon the charge and mass of the particle due to quenching effects. Since heavier particle energies are quenched, they register as lower energy in our detector, as explained in Section 3.2 .

3.3 PROSPECT Calibration System

The PROSPECT detector utilized various methods for calibrating the detector. As described in Section 3.2.1, ^{227}Ac was uniformly distributed throughout the scintillator to calibrate relative segment volumes, but was also used to monitor energy and position resolution stability [80]. Cosmogenic events were also used for various calibrations, some of which are covered in chapter 4. The unique segmentation of the PROSPECT detector allowed for hollow support rods along the edges of each segment, as described in Section 3.2.3. Through these supports, various calibration sources and optical fibers were inserted into the detector volume. Figure 3.17 shows the designated grid for calibration deployment options. Each segment has one corner adjacent to an optical diffuser containing optical fibers, and another corner adjacent to a guide tube designed for the deployment of a radioactive calibration source. In total, there are 42 light injection points and 35 guide tubes.

3.3.1 Optical Calibrations

Each segment has a laser light injection at the segment length midpoint for dedicated periods of calibration. A short pulse driver was utilized with adjustable intensity allowing for calibration across a range of signal sizes. A custom optical splitter allowed the option for simultaneous calibration of the entire detector response. This allowed for studies on the conversion between ADC and photoelectron number by varying the PMT gain settings. While one intention for this system was to calibrate the relative timing between PMT channels and calibrating each PMT's single photoelectron response, other methods were favored for this purpose.

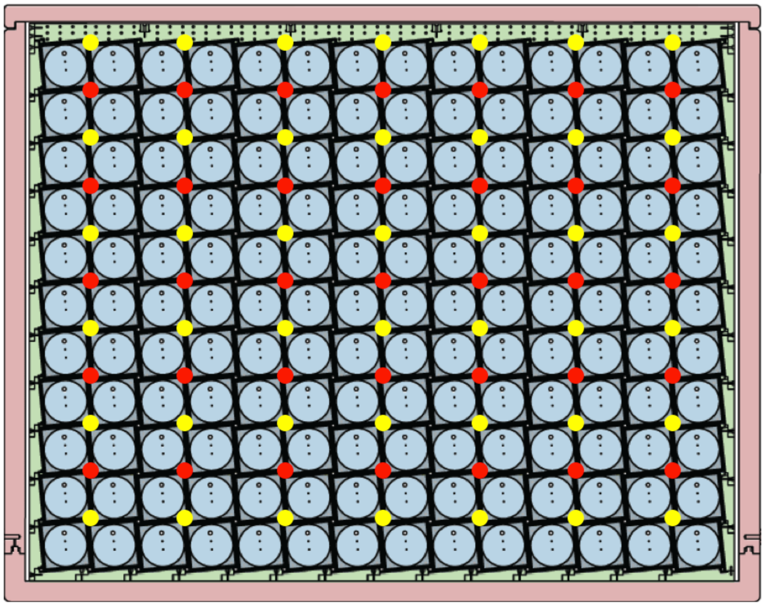

Figure 3.17: Cross section of AD showing vertices of source tubes (red) and optical diffusers (yellow).

3.3.2 Radioactive Source Calibration System

The Radioactive Source Calibration System (RSCS) in the PROSPECT AD was designed to fit the reactor site constraints, and allowed for remote source source deployments. The RSCS uses stepper motors with plastic toothed timing belts to deploy radioactive sources through low-friction tubes. This driver system fits on the side of the outer casing of the PROSPECT AD, as shown in Figure 3.18. During specific reactor off times, calibration campaigns were undertaken during which one or more of the motors drive a source through the polyteraflouroethylene (PTFE) tubing inside of the hollow supports to a location specified and monitored through a slow control web interface. Excess timing belt is routed to storage tubes above the detector. Fully retracted sources they sit inside the belt guides shown on the right of Figure 3.18, where they can be exchanged and stored. The detector shielding is sufficient that the radioactive sources do not introduce significant background while stored in the driver boxes.

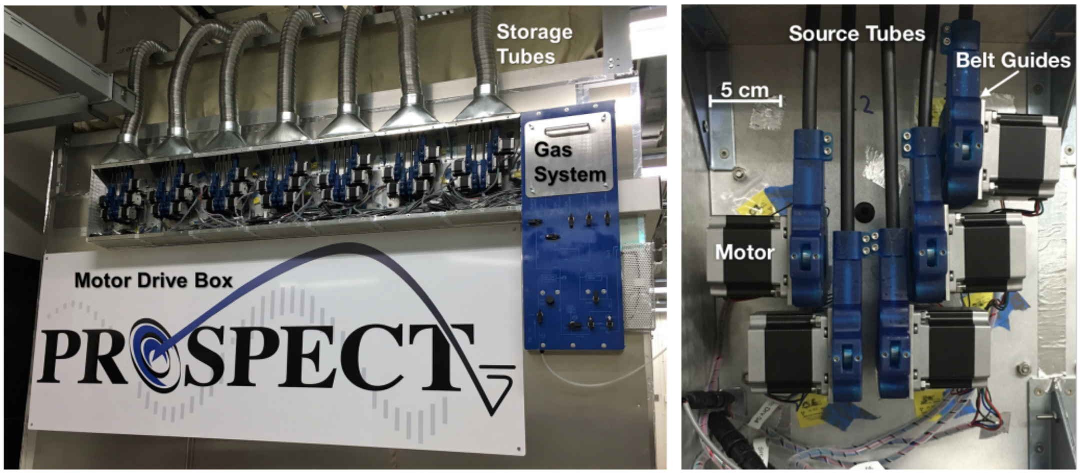

Figure 3.18: PROSPECT source calibration system. 35 motor drives fit into a box approximately 2 m wide, and extend from the face of the detector by only 14 cm. During operation, the box is covered with panels to ensure that light does not travel into the detector volume.

3.3.3 Sources

^{137}Cs, ^{60}Co, and ^{22}Na, AmBe (Americium-Beryllium), and ^{252}Cf sources were contained in aluminum capsules attached to a section of the driver system timing belt, as shown in Figures 3.19 and 3.20. These sources were chosen to be able to characterize various components of PROSPECT's IBD signal, including positron annihilation, energy scale studies, and the neutron mobility and capture. Table 3.1 shows the various decays for these sources.

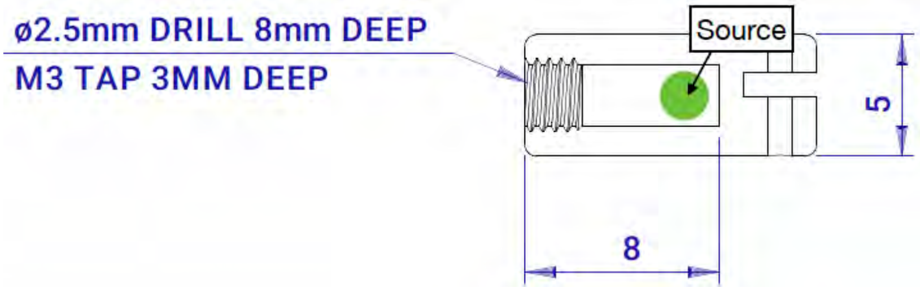
ø2.5mm DRILL 8mm DEEP
M3 TAP 3MM DEEP
Source
5
8

Figure 3.19: Dimensions of aluminum radioactive source capsules used in the source tubes. Numerical tags are in millimeters.

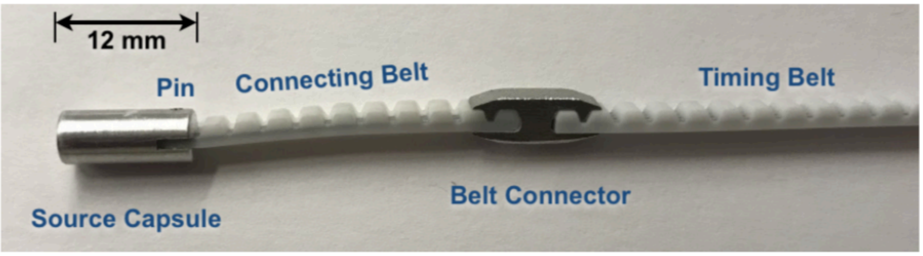
12 mm
Pin
Connecting Belt
Timing Belt
Belt Connector
Source Capsule

Figure 3.20: Source capsule with section of timing belt. The belt slides sideways through the fitted belt connector.

Source	Emission	Energy [MeV]	Approx. Rate
^{137}Cs	β^-	0.662 γ	0.1 μC
^{22}Na	β^+	1.275 γ, 0.511($\times$2)	0.1 μC
^{60}Co	β^-	1.332, 1.173 γs	0.1 μC
AmBe	γ, n	4.4 γ, varies	42 Hz, 70 n/s
^{252}Cf	n (SF)	varies, 2.22 γ (nH capture)	1000 n/s

Table 3.1: The various radioactive calibration sources used in the PROSPECT detector.

Source capsules are sealed with a stainless steel set screw and epoxy, and etched with identification numbers. The source capsules are permanently mounted to a short section of timing belt with a stainless steel spring pin, and the section is then joined to the full driver timing belt by a custom made belt connector, as seen in Figure 3.20. With this scheme, only a short portion of the belt needs to be switched to replace sources, while the remainder of the timing belt remains installed in the tube.

More in depth coverage of the PROSPECT radioactive source calibration system can be found in Ref [81]. Details on the neutron response and calibrations with the ^{252}Cf source is a focus of Chapter 4.

3.4 Monte-Carlo Simulations

In the PROSPECT analysis, Monte-Carlo (MC) simulations are important for determining the energy response matrix for converting the prompt energy spectrum to neutrino energy and for determining the efficiency variation from segment to segment. Since the detectable neutrino energy spectrum is dependent on the detector response, it is important for simulations to accurately replicate known energy responses in the detector. Additionally, to properly measure the segment to segment IBD rate variations, it is important to understand the relative segment efficiency that results from variations in the detector geometry. Simulations were also useful for characterizing detector performance, determining systematic uncertainties from detector geometry, and studying the detector energy response.

The PROSPECT collaboration uses the computational platform GEANT4 as its simulation package. A successor of GEANT developed by CERN, GEANT4 allows specific input on geometry, detector response, and tracking of particles during interactions and decays [82]. PROSPECT-Geant4 (PG4) is the customized version of GEANT4 that contains relevant geometries and event generators. PG4 has been tested in conjunction with PROSPECTs prototyping program to validate the detector simulation model, and has been updated with data to better replicate the detector response. Adjusting and comparing the PG4 simulation to the neutron response of the detector is covered in parts of Chapter 4 as part of my contribution to the PROSPECT analysis.

3.4.1 Energy Response and Resolution

PROSPECT utilizes a calibration scheme that calibrates away position dependence from light collection and then applies a universal scale factor to convert from signal integral to MeV. The remaining non-linear response is dealt with by inclusion in PG4 and using the simulation to convert between detected and real energy. We then interpret the data based on what simulation says the input spectrum will match a given energy spectrum. Birk's Law defines the light yield per path length of a particle traveling through scintillator [83]. PG4 applies Birk's Law as

$$\frac{dL}{dx} = \frac{\frac{dE}{dx}}{1 + k_{B_1}\frac{dE}{dx} + k_{B_2}(\frac{dE}{dx})^2} \tag{3.11}$$

to model the quenching in the scintillator, where $\frac{dL}{dx}$ is the light yield per path length of a particle, $\frac{dE}{dx}$ is the energy deposited per path length, and $k_{B_{1,2}}$ are material dependent first and second order Birk's constants that are fine tuned by comparison with data. The effect of the scintillator nonlinearity is more severe at lower energies, as shown in Figure 3.21.

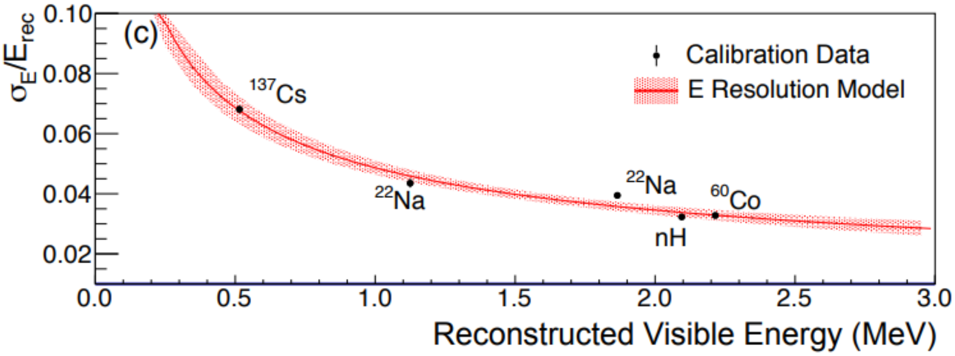

Figure 3.21: The characterized energy resolution of energies for calibration sources fit to the resolution function. [69].

A combination of data from calibration sources and natural backgrounds was used to determine the Birk's constants. The spectra from cosmogenic ^{12}B electrons, nH capture gamma rays, and gamma rays from the sources described in Section 3.3 were simultaneously fit to the PG4 detector response model to determine the Birk's constants as well as other scaling factors, such as effects from Cherenkov radiation. Excellent agreement between data and simulation can be seen in Figure 3.22 for the range of energies as well as the energy deposit multiplicity.

The simulated energy resolution is matched to the data using the following form:

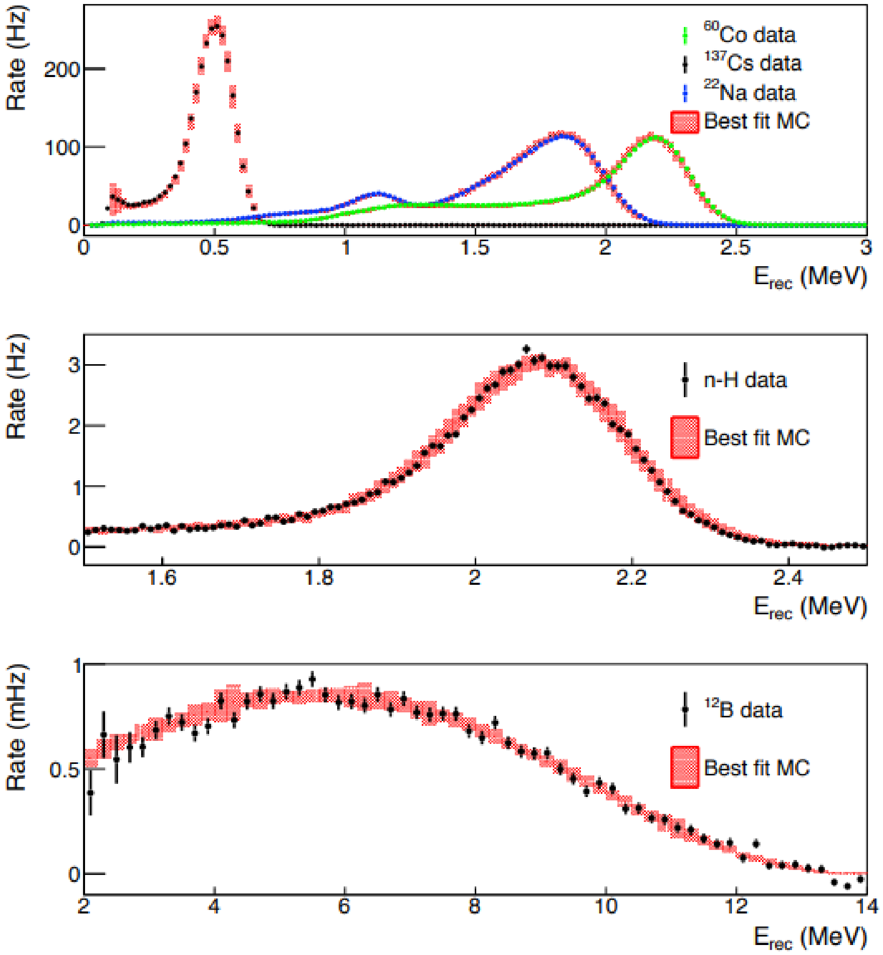

Figure 3.22: Calibration data to best fit MC comparison with energy scale uncertainties. Top: The reconstructed energy for gamma ray sources. Center: The reconstructed energy for nH captures from a ^{252}Cf deployment. Bottom: The reconstructed energy for cosmogenically-produced ^{12}B.[84].

$$\frac{\sigma_E}{E} = \sqrt{a^2 + \frac{b^2}{E} + c^2E^2} \tag{3.12}$$

where a, b and c are dependent on the detector geometry, photostatistics, and PMT quantum efficiency. Figure 3.21 shows this fit giving an energy resolution of 4.8±0.2% at 1 MeV for gamma rays [84].

3.5 Conclusions

The PROSPECT collaboration constructed, installed, and operated a multi-ton, highly segmented antineutrino detector within 7 m of HFIR at ORNL. Although operating at the surface of the Earth, PROSPECT achieved a signal to background ratio of better than 1:1 through a combination of shielding and analysis techniques. The grid design of the detector was ideal for measuring meter-scale wavelength neutrino oscillations, and independent of reactor flux calculations. PROSPECT has already published papers on various detector aspects [59, 77] including the RSCS [81], the optical-grid system [75], and the LiLS scintillator production [74] in addition to the oscillation and spectrum results [69, 68]. While the detector has been decommissioned as of late 2019, there is still unpublished data that is currently being analyzed for future publications. Additionally, research efforts into measuring the longevity of various aspects of the detector's design are underway in preparation for a refurbishment and redeployment in the future.

CHAPTER 4

NEUTRON RESPONSE IN PROSPECT

The PROSPECT experiment has two main goals. One is to make an unambiguous discovery of eV-scale sterile neutrinos, or exclude the existence of this particle in the allowed parameter region with high significance. This is done through the observation of energy and baseline dependent oscillation effects with a method independent of reactor flux predictions. The other goal is to directly test reactor antineutrino spectrum predictions using a well-understood reactor dominated by fission of ^{235}U [34].

Short baseline antineutrino experiments present a number of design challenges related to their proximity to a reactor core. This position all but assures that the detector is near the surface of the earth with little overburden and is inundated by reactor-related backgrounds. Studies have shown that a signal to background ratio of 1:1 is highly desirable, although difficult in practice to achieve. Many factors must be considered to reduce backgrounds, including shielding, energy resolution, fiducialization, segmentations/position resolution, and neutron capture lifetime. This study suggested among other things that a $< 10\%/\sqrt{E(\mathrm{MeV})}$ energy resolution was required. While PROSPECT far exceeded these design goals, ultimately achieving a signal to background ratio of 1.7:1 and 1.32:1 in publications, the detector was observed to degrade much more rapidly in time than expected, while segments being shut off and scintillator properties changing with time, potentially impacting the analysis at a significant level. In this chapter, we detail the use of neutrons to monitor detector performance and address how the detector and LiLS evolution contributes to the uncertainties in the published and future PROSPECT analyses.

For signals with the appropriate PSD, simulations and background measurements predicted a background rate of $> 1000\times$ the rate of IBD events from HFIR. The use of neutron correlated event tagging reduces backgrounds by about two orders of magnitude, which when combined with other event rejections in analysis produces our published 1.7:1 (spectrum [69]) and 1.32:1 (oscillation [68]) signal-to-background ratios. In order to be valid, these background rejection techniques require the detector's energy response and neutron capture lifetime to be stable. We demonstrate through the use of cosmogenic neutrons that our detector energy resolution, while worsening over time, can be manipulated in software so they are stable over time and stay within the necessary $10\%/\sqrt{E}$. We also show how the evolution of our neutron capture lifetime contributes to the assigned 5% systematic uncertainty in the PROSPECT published oscillation analysis [68]. However, these evolutions draws concerns about detector and scintillator degradation that would become more problematic for longer data sets.

Since the oscillation analysis is dependent on measuring relative rates based on location, it is important to understand the neutron capture efficiency as a function of position. Relative variations in efficiency between segments and between time period are important, since the IBD efficiency is expected to be dependent on a segment's proximity to dead segments and the outside of the detector. During the data taking period, multiple PMTs were excluded from analysis since they exhibited anomalous instabilities. Segments that became inactive during the lifetime of the detector, referred to as "dead segments," introduce further detection efficiency concerns. PG4 simulations model the relative segment IBD detection efficiency variations caused by this effect for the oscillation analysis. Therefore it is critical to benchmark the simulation to ensure it gets the physics of neutron mobility right. In this chapter I demonstrate this agreement is sufficient for PROSPECT. One critical parameter in obtaining reasonable agreement between simulation and data is the lithium loading in scintillator. Since the measured neutron capture lifetime did not match simulations using the predicted 0.1% lithium doping fraction, we used PG4 and a deployed ^{252}Cf source to determine the necessary LiLS doping to match the capture lifetime and capture target ratio in data. This doping fraction directly affects the simulated neutron detection efficiency and mobility, which in turn impacts the ability of PG4 to predict the segment efficiency variations. We will show that the determined PG4 doping fraction replicates the neutron mobility from a ^{252}Cf source within statistical error, and replicates the nLi capture efficiency within 2σ of systematic and statistical uncertainty.

4.1 Background Rejection With Neutrons

In IBD (equation 2.2), most of the antineutrino energy is carried by the positron. This positron scatters, depositing most of its energy in nanoseconds, and then pair annihilates with an electron in the detector, as described with equation 2.4. Even with various physical shieldings in place, backgrounds from other signals, such as from cosmogenic events and reactor generated high energy gamma rays and fast neutrons, exceed the number of IBD events by a factor of approximately 1300 [34]. A large number of these background events are removed using a "fiducial" cut where segments are excluded along the outside of the detector grid where we see a higher rate of cosmogenic backgrounds than other segments. Utilizing a neutron coincidence with the IBD positron further removes 98% of the background rate.

Hydrogen present in commercial liquid scintillator provides a target for neutrons captures with a density and capture cross section that yields a neutron capture lifetime of hundreds of microseconds. The 2.2 MeV gamma produced by nH captures travels through multiple segments in the PROSPECT detector with multiple energy deposits, which makes imposing position correlations between the positron and neutron capture signals less useful. By doping the scintillator with ^{6}Li, we provided a neutron capture target with a cross section orders of magnitude higher than with hydrogen alone, as discussed in Section 4.2. The signal produced by nLi is highly localized ($\sim$10 μm) with a PSD distinct from the positron signals. This increase in capture targets with higher capture cross sections reduced the neutron capture lifetime to $\sim$50 μs, improving our background rejection abilities by requiring a smaller coincidence timing between the two signals. Requiring our positron energy signals be correlated with a nLi capture, we reduce our backgrounds by several orders of magnitude.

Data taken while the reactor was shut off is used to measure and subtract backgrounds not produced by the reactor, so any time dependent changes in the energy resolution will complicate subtracting the reactor on/off IBD energy spectra. Additionally, if the IBD detection efficiency changes over time, this will affect subtracting individual segment rates used for measuring neutrino oscillations. Any changes in detector behavior and response over the data taking period must be carefully measured and compensated. The following sections detail how we use neutrons to characterize the detector's response over time by measuring the neutron capture lifetime and energy resolution. We also need to be able to accurately simulate the detector response in terms of neutron mobility and efficiency, which is achieved by comparisons of data and simulation with a ^{252}Cf source.

4.2 Neutron Sources and Targets

We use two primary sources of neutrons to measure the neutron response in the PROSPECT detector. One is a deployed ^{252}Cf source in the calibration system, that gives off almost 1000 neutrons per second from a known point source location in the detector. The other source is from cosmogenic sources that appear throughout the detector at all times. Cosmogenic neutrons impinge on the detector with a rate of tens of Hz [85].

^{252}Cf is an alpha-emitter with a 3.1% spontaneous fission branching fraction. An average of 3.757 neutrons and 7.98 gamma rays are emitted per fission [86]. The average neutron energy is 2.1 MeV, and the average gamma ray energy is 0.87 MeV [87].

When cosmic high energy protons and other nuclei scatter in the Earth's atmosphere, they produce showers of secondary particles that can reach the Earth's surface. Muons, protons, neutrons and other hadrons are among the secondary particles produced. The neutrons can find their way into the detector at high enough energies. If a high energy cosmic particle hits the lead shielding in the PROSPECT detector, this can induce neutron spallation while also depositing large amounts of energy into the detector. We can identify and use these neutrons to measure the neutron response throughout the detector.

The two dominant targets for neutron captures in the PROSPECT detector are ^{6}Li atoms and protons (H). Details about the scintillator are found in Section 3.2.1. When discussing neutron captures, we will call captures on ^{6}Li "nLi" and captures on H "nH." Figure 4.1 shows the capture cross section, σ_a, of fast neutrons on these two targets, as well as the next two likely nuclei for neutron captures (^{12}C and ^{35}Cl)

[88]. To determine how many neutrons we expect to capture on H vs ^{6}Li we first need to determine how much of each is in the detector.

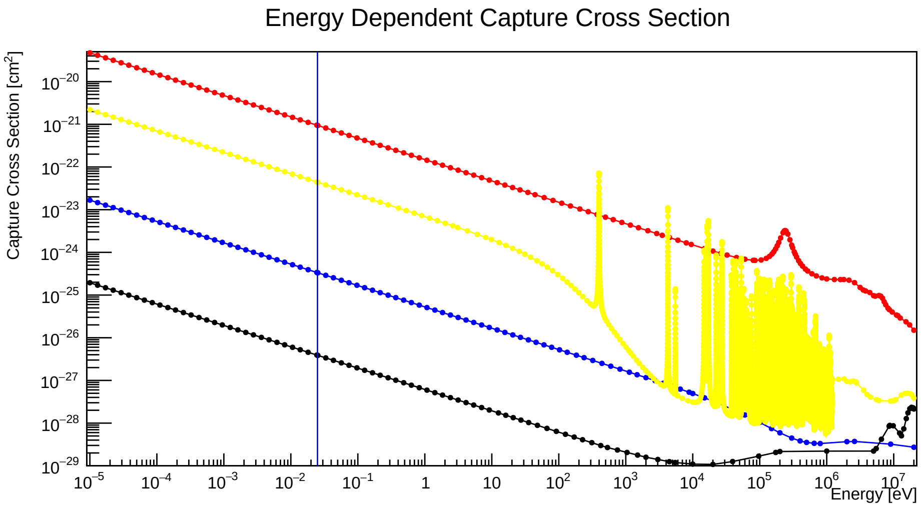

Figure 4.1: Neutron capture cross sections on ^{6}Li ($\sigma_{a,Li}$, red, top), ^{35}Cl ($\sigma_{a,Cl}$, yellow, middle top), H ($\sigma_{a,H}$, blue, middle bottom) and ^{12}C ($\sigma_{a,C}$, black, bottom). The peaks in $\sigma_{a,Li}$ and $\sigma_{a,Cl}$ corresponds to a nuclear resonance energy levels. The blue vertical line indicates thermal neutron energy (0.025 eV) [88].

The ^{6}Li doping fraction of the scintillator can be defined as

$$f_{Li} = \frac{\rho_{Li} \cdot M_{Li}}{\sum\limits_i (\rho_i \cdot M_i)} \tag{4.1}$$

where ρ_i and M_i are the volume number density and molecular mass of each element in the scintillator. The scintillator density and main component composition is summarized in Table 4.1.

Property	PROSPECT Liquid Scintillator
C:H:O ratio (by weight)	84.34 ± 0.11: 9.69 ± 0.21 : 5.97 ± 0.24 %
Density (g/mL)	0.9781 ± 0.0008

Table 4.1: Density and composition of the PROSPECT Scintillator [74].

A study at Brookhaven National Lab (BNL) of the LiLS production after starting analysis measured the lithium doping fraction by weight of $(8.2 \pm 0.1) \cdot 10^{-4}$ for each barrel of scintillator [74]. We used 28 Li-doped barrels and 1 undoped barrel to fill the detector, resulting in a doping fraction of approximately $(7.9 \pm 0.1)\cdot 10^{-4}$ for the bulk scintillator of the detector, which is slightly lower than the initially desired doping fraction of $1\cdot 10^{-3}$. Using Equation 4.1, the doping fraction from the BNL measurement, and the density of materials in the scintillator, the expected volume number density of ^{6}Li in the scintillator is $(7.62 \pm 0.09) \cdot 10^{19}$ /cm^3, and $(5.66 \pm 0.12) \cdot 10^{22}$ /cm^3 for H. The expected ratio of neutron captures on hydrogen to lithium can be expressed as

$$\frac{\text{nH}}{\text{nLi}} = \left(\frac{\rho_H}{\rho_{Li}}\right) \cdot \left(\frac{\sigma_{a,H}}{\sigma_{a,Li}}\right) \tag{4.2}$$

Using the capture cross sections from Figure 4.1 for thermal neutrons and the volume densities of ^{6}Li and H,

$$\frac{\text{nH}}{\text{nLi}}(\text{therm}) = 0.256 \pm 0.007. \tag{4.3}$$

The relative capture ratio for thermal neutrons shows that we should expect approximately 4× more captures on ^{6}Li than on protons. While the capture cross section for ^{35}Cl is much more than for H, the relative density of the two means thermal neutrons will capture on H ∼5.6× more often than ^{35}Cl, with ^{12}C being even less often. Since nLi events are the cleanest to identify and most plentiful, the IBD analysis uses these events as the neutron capture target. As highlighted in the following sections, both nLi and nH captures were used to track various aspects the calibration highlighted in the following sections.We also also primarily used ^{6}Li events for the neutron calibration analyses highlighted in the following sections. In general using ^{6}Li as the capture target is best for statistics, and is used for IBD detection instead of H.

4.3 Detector Stability With Cosmogenic Neutrons

PROSPECT took continuous data for ∼10 months of time to measure both the antineutrino spectrum and the IBD rate as a function of position. We observed significant changes in the detector performance and measures were adopted to mitigate these changes. We will show that the neutron response was key in diagnosing the detector changes with time, and their effect on the analyses. Furthermore, experiments such as PROSPECT that sit next to research reactors use reactor off times to measure and subtract backgrounds. It is critical that we consider changes in the detector response between periods of the reactor being on and off. Thus, a great deal of effort was put into measuring the detector stability over time and calibrating away any changes seen. In this section, we will analyze 7 months of data to show how cosmogenic neutrons were used to measure the energy resolution stability with nH captures, as well as how our collaboration analysis handled a worsening resolution, and for how long our methods are viable. Then, we will show how the nLi capture lifetime evolved during the detector lifetime, and its impact on the IBD detection efficiency.

4.3.1 Energy Resolution Stability

Neutrons capturing on hydrogen provide a sample of mono-energetic 2.2 MeV gamma rays, which can be used to track the detector performance and calibrations with respect to energy reconstruction. The following analysis was used to demonstrate our detector energy resolution in the oscillation result publication [68].

Table 4.2 summarizes the event selection for this study. We identify cosmogenically produced neutrons by looking for a high energy (E > 15 MeV) hit in the detector (typically a muon) followed by one or more neutron captures. We use a time window removed from truly correlated signals to measure the signal component arising from random but uncorrelated coincidences. We call this the "accidentals" time window. To reduce the statistical uncertainty from the background subtraction by more than 3×, the accidentals time window is 10 times longer than the coincidence time window, and scaled appropriately.

Cut type	Description
prompt E	$E > 15.0$ MeV
delayed E	1.8 - 2.5 MeV
coincidence window	$2 < t_{nH} - t_{prompt} < 250\ \mu$s
accidental window	$-2500 < t_{nH} - t_{prompt} < -20\ \mu$s

Table 4.2: Cuts used to identify nH captures after a cosmically induced event.

Figure 4.2 shows the resulting nH energy spectrum from the entire detector volume. Here we see a spectrum of energies below the peak, due to not detecting every Compton scatter and energy deposit by the 2.2 MeV gamma ray. The peak itself is smeared out at energies below the spectrum peak. By fitting the 2.0 to 2.35 MeV energy range with a Gaussian, a peak sigma value is obtained. Figure 4.4 summarizes these values with linear fits to track the evolution over time.

It is clear that the energy resolution (measured by a Gaussian 1σ width) is degrading over time, by ~11% over 7 months. Studies of other energy sources have shown that the energy resolution decreases steadily in the detector due to an overall decrease in light collection over time. This implies some factor of scintillator degradation whose cause is not yet understood. In order to match the detector resolution over time for subtracting the reactor on and off spectrain the IBD analysis, the value E_{smear} was introduced. To mitigate the energy resolution changes with time and the accompanying response matrix evolution, for each published analysis a software calculated value, E_{smear}, was utilized instead of energy, where an additional time-dependent noise component was artificially added to the data to force the energy resolution to be constant in time. The E_{smear} peak width and the resulting Gaussian fit parameter are also plotted in Figures 4.2 and 4.4. We do not expect the mean E_{smear} to be any more stable than the original energy, since they are calibrated to the same mean value. The mean energies are stable within ±0.5%.

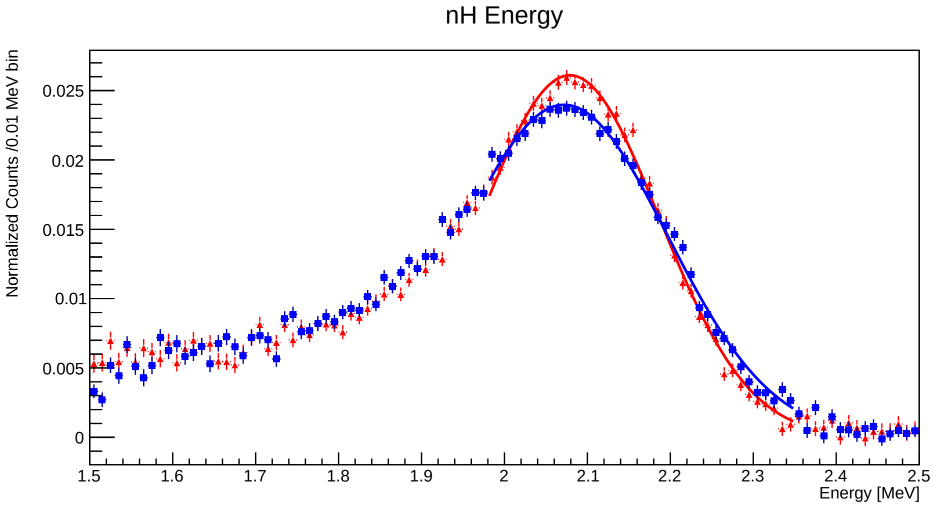

Figure 4.2: A sample energy spectrum of the nH captures following a cosmogenic event (with accidentals subtraction) using 7 days of data. The red triangles show the reconstructed energy, while the blue squares represent the E_{smear} parameter. Gaussian fit lines are shown in Black on each distribution.

The slopes of the linear fits from Figure 4.4 are summarized in Table 4.3. These fits show that within error the nH width for E_{smear} are stable (rate of change consistent with zero), but not without this smearing.

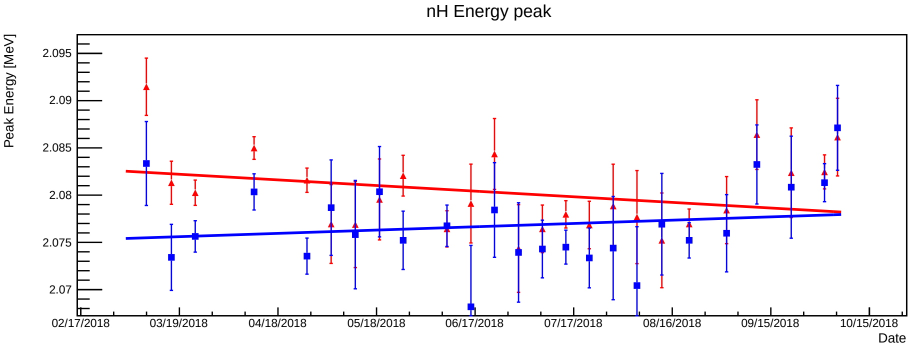

Figure 4.3: Mean of gaussian fit to nH Energy peak vs time. The red triangles show the reconstructed energy, while the blue squares represent the E_{smear} parameter. Linear fits applied yield stability within ±0.5%.

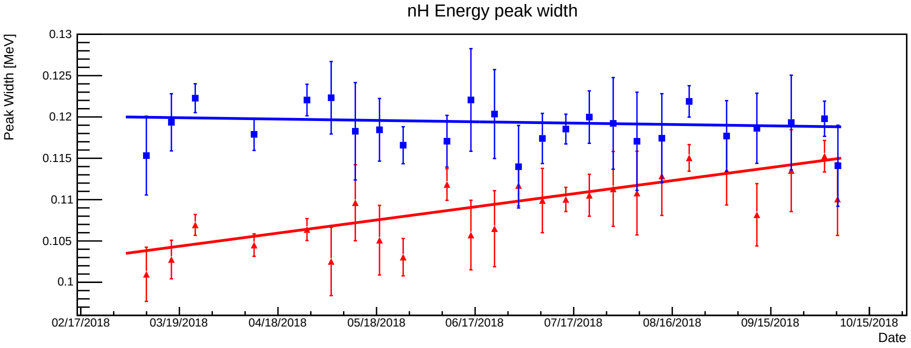

Figure 4.4: nH energy 1σ Gaussian width vs time. The red triangles show the reconstructed energy, while the blue squares represent the E_{smear} parameter. Linear fit trend described in text and Table 4.3. The varying statistical error bars comes from the difference in reactor on and off cycles.

Data	Width change [keV/day]
E	0.053 ± 0.0077
E_{smear}	-0.005 ± 0.009

Table 4.3: Slopes from the linear fits in Figure 4.4.

This study demonstrates the evolution of the PROSPECT detector energy resolution, but is a poor indicator of the absolute energy resolution. While the energy width would represent a ~8.2%/$\sqrt{E}$ energy resolution, since the peak is not Gaussian and there are energy loss effects in this energy peak, this is not a great measure of the energy resolution. Simulations replicated key photon energy resolutions as shown in Figure 3.21 to give a final energy resolution of ~5.5% at the end of data taking in December 2018. Using the linear resolution trend line in Figure 4.4 and the PG4 simulation matched energy resolution, it is predicted that the energy resolution would only reach 10% after more than 1500 total days of data taking. While this effect is within the requirements for the PROSPECT analysis, the degradation is highly undesirable since it increases the systematics and the degraded resolution reduces the reach of the oscillation analysis and the resolution of spectrum measurements.

4.3.2 Neutron Capture Lifetime

In order to understand the efficiency of the time window between prompt and delay IBD events, it is necessary to know the capture lifetime of neutrons in the detector, and how much it evolves over time. Before measuring the capture lifetime, we will first derive the expected form of our capture lifetime distribution.

Assume a rate of neutrons R traveling some distance dx through a uniform volume of targets with capture cross section σ and number density ρ. The rate of neutrons capturing on the target evolves as

$$dR = -R\rho\sigma dx = -R\rho\sigma v dt \tag{4.4}$$

for neutrons moving with speed v. For thermal neutrons, σ and v are approximately constant, with a solution of

$$R = R_0 e^{-t/\tau} \tag{4.5}$$

where

$$\tau \equiv \frac{1}{\rho\sigma v}. \tag{4.6}$$

When there is a mixture of targets in the volume, we sum over individual targets, $\sum_i n_i \sigma_i$, which makes the total capture lifetime

$$\frac{1}{\tau} \equiv \left[\sum_i \rho_i \sigma_i\right] v \equiv \sum_i \frac{1}{\tau_i} \tag{4.7}$$

which will still give a general form of Equation 4.5. At fast neutron energies, $\mathcal{O}$(MeV), the neutron capture cross section is orders of magnitude lower as seen in Figure 4.1. The most likely scenario for these neutrons is that they scatter and thermalize in times much shorter than the capture lifetime, τ.

Events in data are selected by first identifying a potential muon event with energy above 15 MeV as in the energy stability study. Then, nLi captures are identified in a coincidence time window as shown in Table 4.4. Once again we use a scaled down accidental time window with an extended range to reduce statistical error. The energy and PSD parameters of nLi are the same as used by the IBD analysis. The PSD of these nLi captures must be $> 3.6\sigma$ from the gamma-like PSD band mean (demonstrated in Figure 4.5), and the nLi energy must be between 0.46-0.60 MeV. Toy simulations of fast neutrons in scintillator predict a thermalization time ~6 microseconds, which causes slight deviations from exponential behavior at early capture times. Because of this, capture lifetime fits for cosmogenic induced nLi use only 6-250 μs.

Cut type	Description
prompt E	E > 15.0 MeV
delayed E	0.46-0.60 MeV
delayed PSD	$> 3.6\sigma$ above gamma band
coincidence window	$6 < t_{nLi} - t_{prompt} < 250$ μs
accidental window	$-2500 < t_{nLi} - t_{prompt} < -60$ μs

Table 4.4: Cuts used to identify nLi captures after a cosmically induced event.

The accidental subtracted coincidence distribution in Figure 4.6 fits well to the exponential distribution described by Equation 4.5. By performing this process in 5 day time bins, a nLi capture lifetime trend is obtained as shown in Figure 4.7. For consistency, segments that were on in March but off in October were ignored for this analysis, so each data point in Figure 4.7 uses the same segment list.

The nLi capture lifetime increased from 49.52 ± 0.06 μs to 50.62 ± 0.06 μs from March to October 2019. Extrapolating the linear trend shown in Figure 4.7 predicts an increase of 1.57 ± 0.06 μs (3.18 ± 0.01 %) annually. In addition to having implications on the IBD efficiency, this change could point to a larger problem in the evolving lithium composition of the LiLS. Due to evidence from this and other channels, PROSPECT is currently investigating the possibility of the ^{6}Li content changing

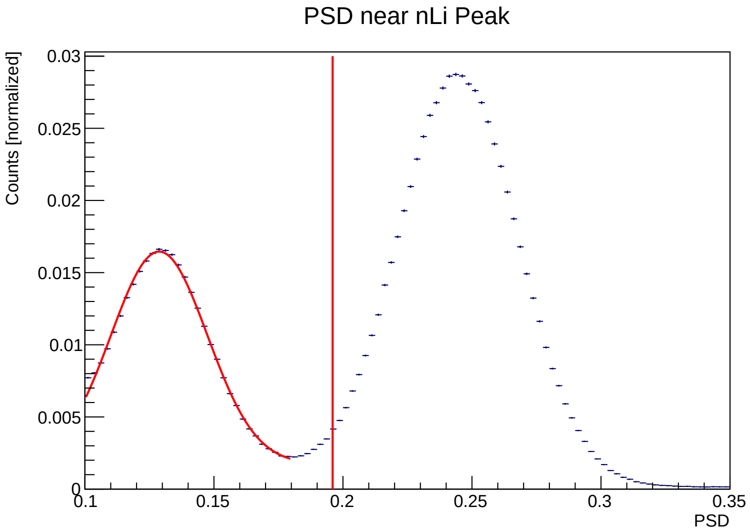

Figure 4.5: PSD for energy near 0.53 MeV. The left distribution shows the gamma band from Figure 3.12, and the right distribution shows the nLi capture peak. The gamma band is fit with a Gaussian, and nLi are selected as events above 3.6σ above the left distribution, marked by the vertical red line.

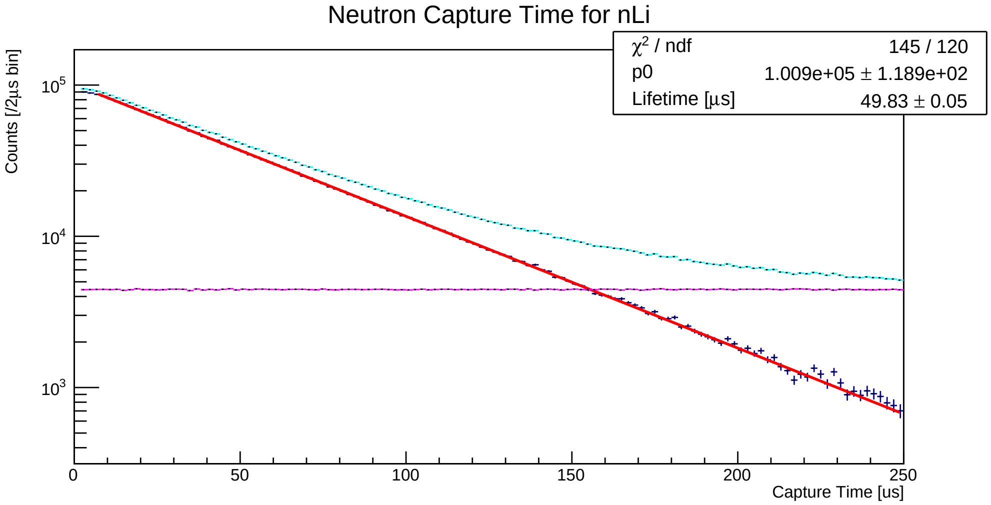

Figure 4.6: Sample nLi capture lifetimes from 5 consecutive days of cosmically induced neutron data in early May 2018, to times below the fit range. Light Blue is coincidence events, magenta is the accidentals distribution, and dark blue with the red fit line is the accidentals-subtracted distribution. Error bars are statistical. Exponential fit applied is described in Equation 4.5, where the capture lifetime τ is 49.83 ± 0.05 μs.

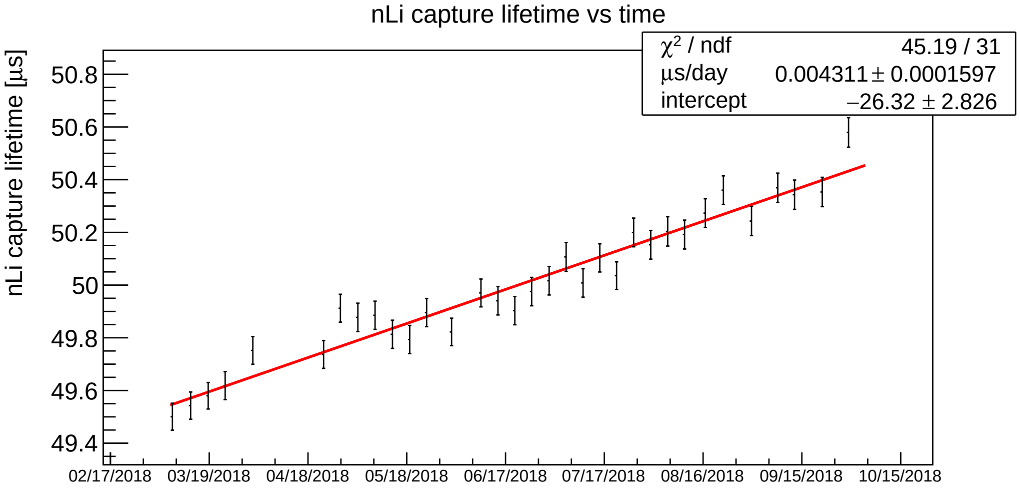

Figure 4.7: nLi lifetime constant (τ) per 5 day bins from March until October 2019. Error bars are from the exponential fit errors like in Figure 4.6. A linear fit was applied to find the projected increase of 4.31 ± 0.16 ns/day in nLi τ.

with time in the detector. Further implications of this loss of ^{6}Li on the IBD detection efficiency is analyzed later in Section 4.5.

4.3.2.1 nLi Lifetime Effect on IBD Efficiency

Since the IBD analysis uses a coincidence time window cut for times between 1-120 μs, the increasing nLi capture lifetime causes a change in the IBD detection efficiency. To calculate the IBD efficiency from the neutron capture time window, where we can integrating over all time, with R from Equation 4.5,

$$N_{Tot} = \int_0^\infty R dt = -R_0\tau[e^{-\infty/\tau} - e^{0/\tau}] = R_0\tau \tag{4.8}$$

and the detected number of neutrons as

$$N_{Det} = \int_{t_1}^{t_2} R dt = R_0\tau[e^{-t_1/\tau} - e^{-t_2/\tau}] \tag{4.9}$$

and we calculate an efficiency from this cut for each lifetime as

$$\text{Efficiency} = \frac{N_{Det}}{N_{Tot}} = (e^{-1/\tau} - e^{-120/\tau}). \tag{4.10}$$

This gives an efficiency of 0.8914 ± 0.0003 (for τ = 49.52 ± 0.06 μs) and 0.8870 ± 0.0003 (for τ = 50.62 ± 0.06 μs), resulting in a relative decrease of $(0.48 \pm 0.04)\%$ in IBD detection efficiency due to increasing nLi capture lifetime in 210 days of data.

For background subtractions, the average difference between a given reactor on and reactor off period is generally less than one month for the PROSPECT analyses. The change in detection efficiency from this time window effect is 0.07 ±0.005% over 1 month difference. At the rate of IBD detection (771/day), with taking into considerations backgrounds and accidentals, the statistical uncertainty in the number of IBDs detected would reach 0.44% in 1 year, and 0.25% in 3 years [69]. This demonstrates that the detection efficiency change will generally stay well below the statistical uncertainty for data sets longer than 3 years.

4.3.2.2 Capture Lifetime Impact on Oscillation Analysis

In the interest of measuring position dependent variations in the detector, the capture lifetime distributions are separated into rows. By measuring how much the capture lifetime changes in the 7 months of data, we extrapolate the lifetime trend out to one year and calculate the IBD detection efficiency difference from the evolving capture lifetime. It is important to note here that the top row of the detector (row 10) was excluded for the IBD analysis, as part of the fiducial cuts described in Section 4.1. Figures 4.8 and 4.9 show the capture lifetime evolution for each row in the detector, with their linear trends shown in Figure 4.10 and Table 4.5. Table 4.6 then summarizes the time window efficiency per row at the start of data taking and a projected 1 year efficiency change using Equation 4.10 and the values in Table 4.6. These efficiencies from Table 4.6 are plotted in Figure 4.11.

As shown in Figure 4.11, the IBD detection efficiency from the nLi capture lifetime varies from row to row in the detector. The variation between the efficiencies at the start of data taking in the detector is within ±0.3% for rows 1-9, and projected to stay within ±0.5% for 1 year of detector operation. In the published oscillation analysis, these segment-to-segment variations were accounted for using the ^{227}Ac rate variation of <2% between segments, which was combined with other effects as a 5% segment-uncorrelated IBD rate uncertainty, which will conservatively cover the variation from the spatial dependent efficiency [68]. Further implications from this effect as interpreted as a different lithium content per row is discussed in Section 4.5

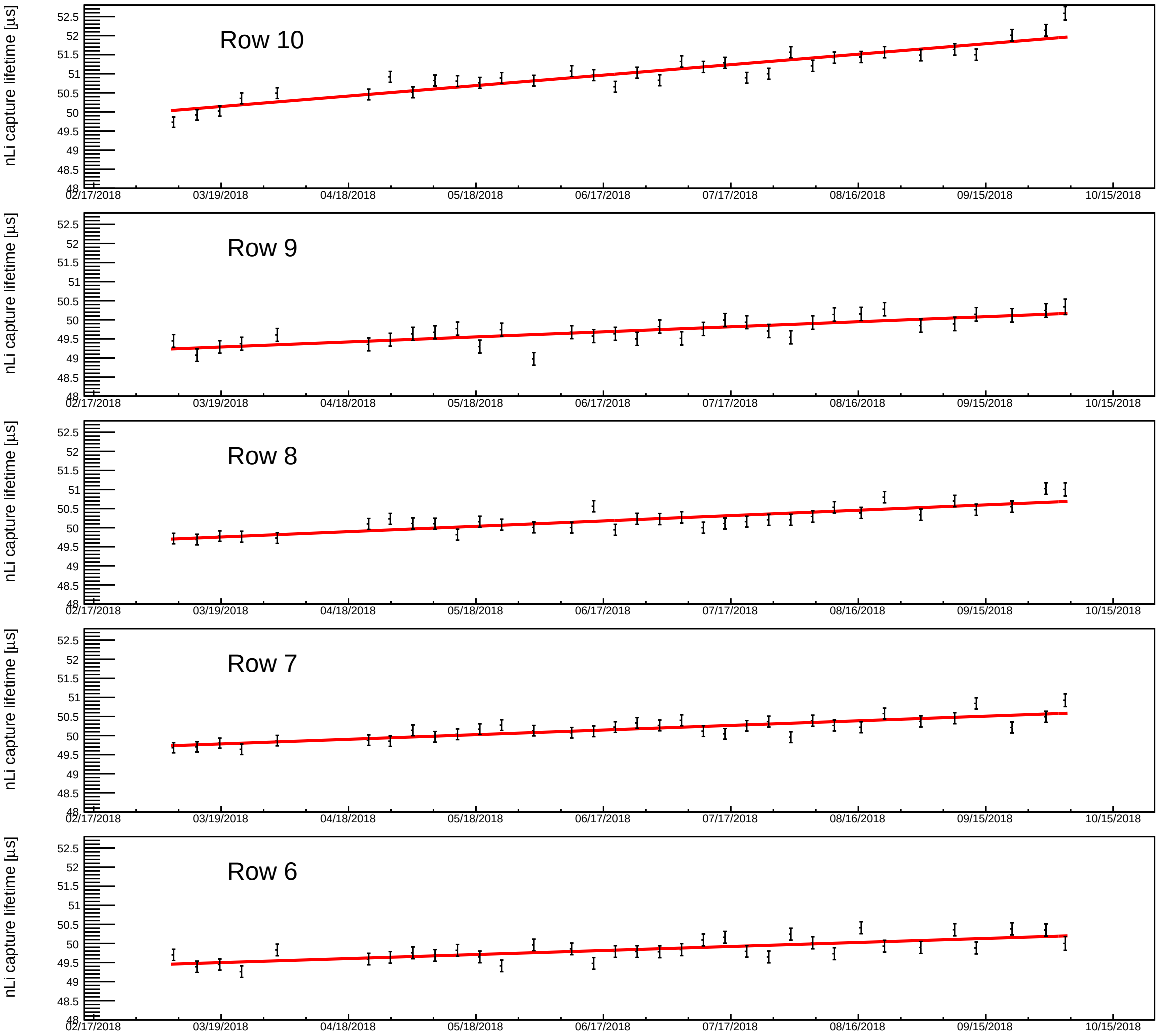

Figure 4.8: nLi capture lifetime constant (τ) time evolution per row for the top half of the detector. Linear fit results are given in Table 4.10.

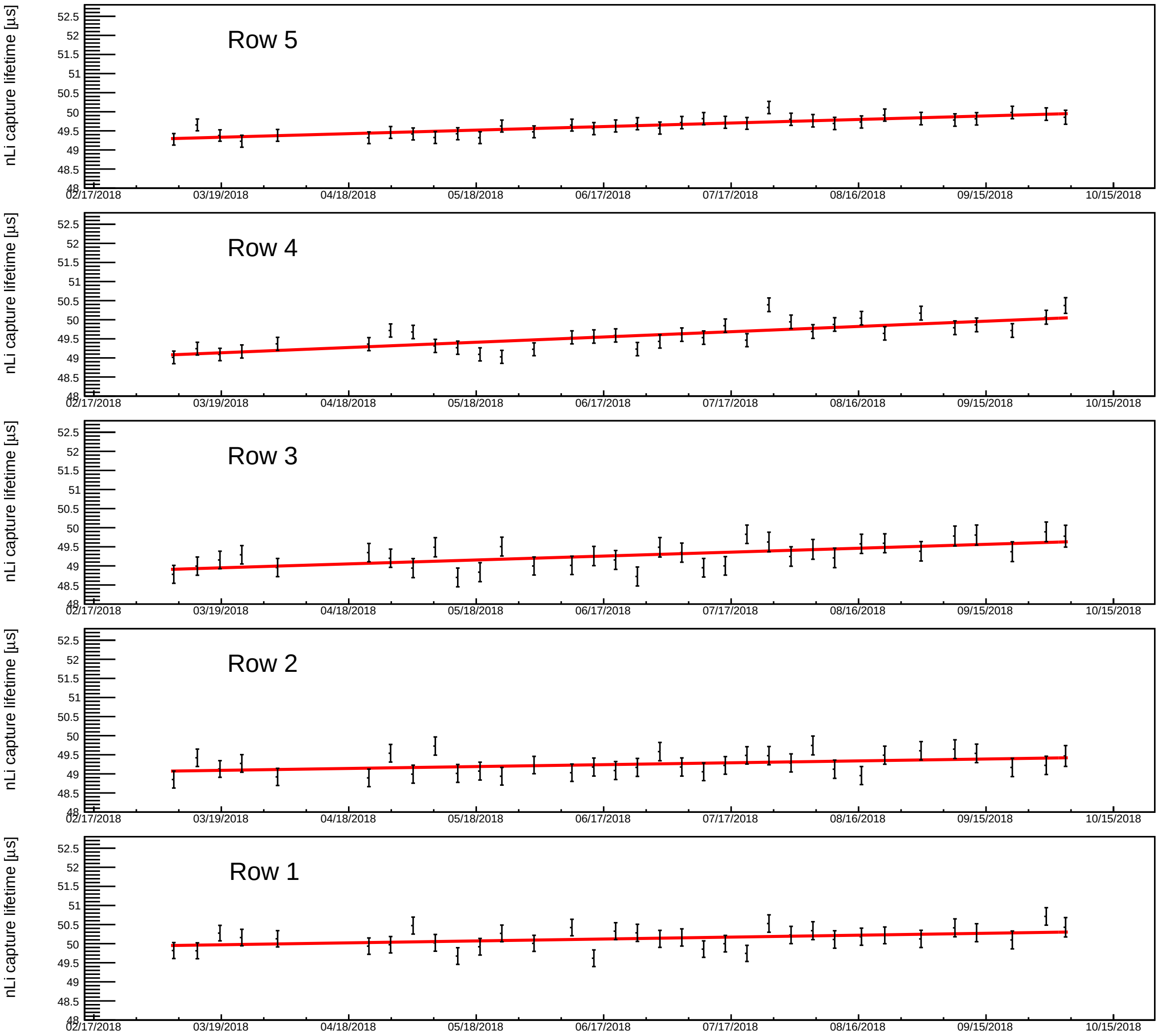

Figure 4.9: nLi capture lifetime constant (τ) time evolution per row for the bottom half of the detector. Linear fit results are given in Table 4.10.

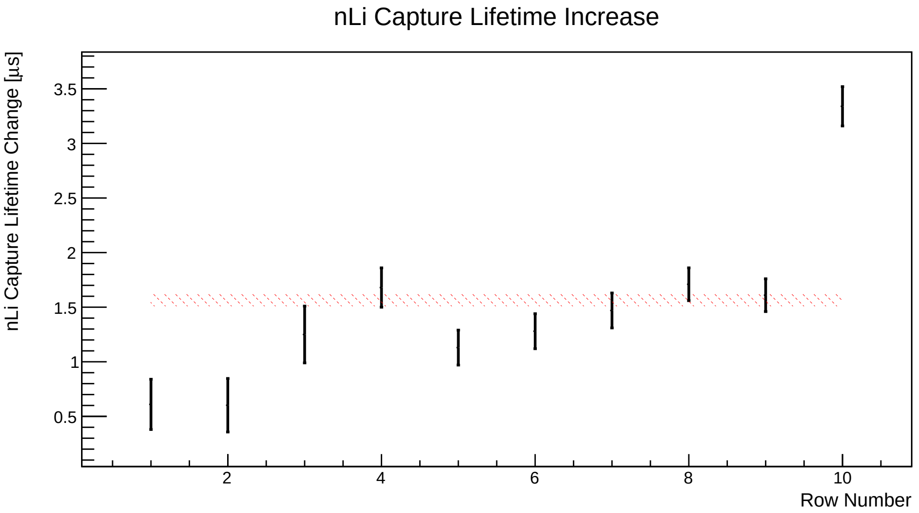

Figure 4.10: Change in nLi capture lifetime (μs/year) for each row of the detector. The shaded region indicates the total detector average. Plotted values found in Table 4.5.

Selection	nLi $\Delta\tau$ annually	% nLi $\Delta\tau$ annually
Full Detector	$1.57 \pm 0.06\ \mu s$	3.96 ± 0.15 %
Row 1	$0.61 \pm 0.23\ \mu s$	1.5 ± 0.6 %
Row 2	$0.60 \pm 0.25\ \mu s$	1.6 ± 0.6 %
Row 3	$1.25 \pm 0.26\ \mu s$	3.2 ± 0.7 %
Row 4	$1.68 \pm 0.18\ \mu s$	4.3 ± 0.5 %
Row 5	$1.13 \pm 0.16\ \mu s$	2.9 ± 0.4 %
Row 6	$1.28 \pm 0.16\ \mu s$	3.2 ± 0.5 %
Row 7	$1.47 \pm 0.15\ \mu s$	3.7 ± 0.4 %
Row 8	$1.71 \pm 0.15\ \mu s$	4.3 ± 0.4 %
Row 9	$1.61 \pm 0.18\ \mu s$	4.1 ± 0.5 %
Row 10	$3.34 \pm 0.15\ \mu s$	8.4 ± 0.4 %

Table 4.5: Summary of the change in the nLi capture lifetime, from linear fits in Figures 4.7, 4.8, and 4.9.

Selection	IBD Eff : Start	IBD Eff : 1 yr	Change after 1 yr
Full Detector	0.8915 ± 0.0002	0.8852 ± 0.0003	0.62 ± 0.04 %
Row 1	0.8903 ± 0.0008	0.8879 ± 0.0012	0.24 ± 0.14 %
Row 2	0.8938 ± 0.0008	0.8914 ± 0.0012	0.24 ± 0.15 %
Row 3	0.8946 ± 0.0008	0.8897 ± 0.0012	0.49 ± 0.15 %
Row 4	0.8934 ± 0.0006	0.8867 ± 0.0010	0.66 ± 0.12 %
Row 5	0.8922 ± 0.0006	0.8878 ± 0.0009	0.45 ± 0.11 %
Row 6	0.8907 ± 0.0006	0.8856 ± 0.0009	0.51 ± 0.11 %
Row 7	0.8907 ± 0.0005	0.8848 ± 0.0008	0.59 ± 0.09 %
Row 8	0.8907 ± 0.0008	0.8839 ± 0.0008	0.68 ± 0.10 %
Row 9	0.8915 ± 0.0007	0.8851 ± 0.0010	0.64 ± 0.12 %
Row 10	0.8907 ± 0.0008	0.8772 ± 0.0008	1.34 ± 0.10 %

Table 4.6: Projected change in nLi capture lifetime over 1 year given linear trends in fit lines in Figures 4.7, 4.8, and 4.9.

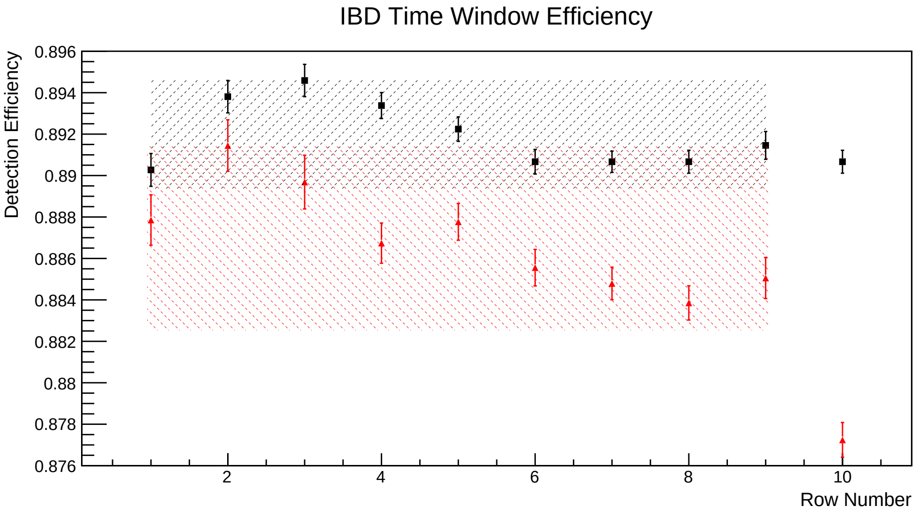

Figure 4.11: IBD detection efficiency from the capture lifetime window by row, at the beginning of data taking (black squares) and predicted 1 year (red triangles) from Table 4.6. Shaded regions show 0.3% (black) and 0.5% (red) range of the 9-row average for the data.

4.4 Benchmarking Lithium Content in PG4

The ^{6}Li doping fraction needed to be high enough to reduce the total neutron capture lifetime in the scintillator and make ^{6}Li the dominant capture target, while not reducing the scintillator light collection below allowable photostatistics for energy resolution. Initial simulations and prototypes with a ^{6}Li doping of 0.1% by weight measured the neutron capture lifetime at $\sim$42 μs. However, the neutron capture lifetime following cosmogenic events in Section 4.3.2 showed a capture lifetime in the PROSPECT detector of $\sim$50 μs, that steadily increased suggesting that the ^{6}Li doping fraction within the detector is decreasing. Determining the ^{6}Li doping fraction in simulation to best match data is necessary to properly simulate IBD events.

PG4 simulations are used for determining the segment-to-segment efficiency variation in the detector due to dead segment effects and other geometric effects. Additionally, it is used to determine the response matrix to convert the prompt signal energy to neutrino energy. In this chapter, we use a deployed ^{252}Cf neutron source to determine what ^{6}Li doping fraction in PG4 simulations are required to match capture lifetimes and capture ratios in our data sets from each calibration campaign. We then test how well this PG4 doping fraction replicates the neutron mobility and nLi capture efficiency in data.

4.4.1 Lithium Doping Fraction in PG4

Using ^{252}Cf calibration data from 31 May 2018, 28 August 2018, 18 December 2018, and 25 February 2019, we assess what ^{6}Li doping fraction in the PG4 simulation will replicate the capture lifetime on both ^{6}Li and H, as well as the ratio of neutron captures (H to ^{6}Li) that we see in real data at these discrete points in time.

^{6}Li doping fractions between (7.0-8.0)$\cdot 10^{-4}$ by weight were simulated to gauge which one will match each of the three aspects above for each set of calibration data. Since the scintillator was spiked with ^{227}Ac also as a chloride solution, the loss rate of ^{6}Li in the detector can be compared to the loss rate of ^{227}Ac, as was done in Section 4.5.

4.4.1.1 Source Deployment Locations

Figure 4.12 shows the PROSPECT detector grid, along with the calibration source tubes used for this analysis. These deployment locations are centrally located and minimize the number of nearby dead segments. Deployments after May '18 use the same deployment location. The driver used for the May '18 data set was inoperable afterwards.

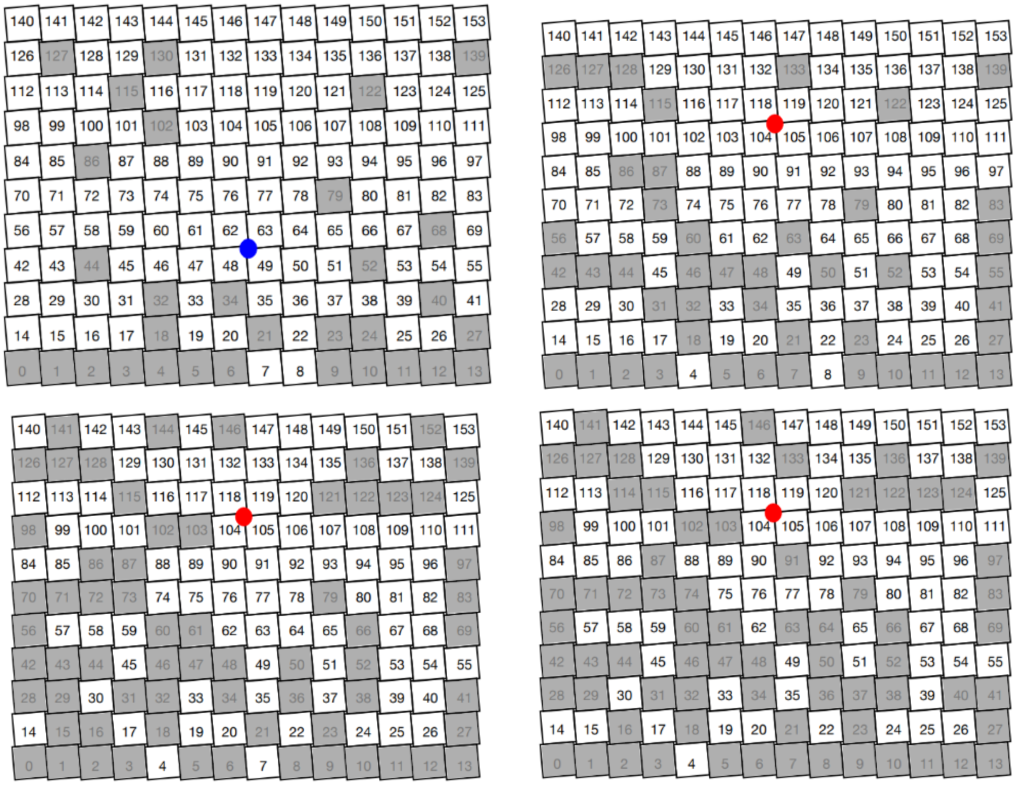

Figure 4.12: Location of ^{252}Cf deployment represented by a dot in detector for different deployment dates. May '18 top left, Aug '18 top right, Dec '18 middle left, Feb '19 middle right. Shaded boxes represent segments unusable for analysis.

4.4.1.2 Event Identification

The ^{252}Cf source, as described in Section 4.2, emits neutrons at a rate $O(1\text{ kHz})$. The photons Compton scatter and deposit all their energy in tens of nanoseconds, while the ~1 MeV neutrons thermalize in a few microseconds, then capture in ~50 μs. This allows temporal tagging of the prompt photons from fission followed by a delayed neutron capture signal. Using this, we identify the neutrons from ^{252}Cf capturing in the detector.

To identify fission events from ^{252}Cf, first a prompt flash of gamma energy is identified, and then neutron capture signals are identified within time windows for correlated and accidental events, similar to the previous cosmogenic neutron studies. Data selection criteria are shown in Table 4.7. The different analyses use different coincidence time ranges that reflect different systematics to the study.

Selection type	cut values
Prompt Energy	0.5 - 15.0 MeV
Δ t (coincidence)	2-250 μs
Δ t (accidental)	1.52-4.0 ms
Delayed nH Energy	1.8-2.5 MeV
Delayed nLi Energy	3σ
Delayed nLi PSD	3σ

Table 4.7: Data selection criteria for location nLi and nH captures from a ^{252}Cf source for the doping study.

With the measured the nLi capture lifetime in the detector ~50 μs from cosmogenic neutrons, the coincidence time window should detect $\sim$ 95% of neutron captures. When used for background subtraction, the accidental counts and capture time distribution is scaled down given the increased exposure time. The [2,250] μs coincidence time window is only used for counting nH and nLi captures for the capture ratio method. The methods for matching the capture lifetimes will use a different fit range discussed in their analysis.

The energy and PSD distributions for the nLi signal are approximately Gaussian. The Gaussian sigma value can be obtained from a fit and used for selecting these events. The neutron captures on ^{6}Li are cut in PSD and energy with a 3-σ circular cut, as seen in Figure 4.13. This is performed on each data set in order to remove dependence on energy and PSD resolution changes in time.

Similar to the prompt energy, the nH gamma rays deposits energy during multiple Compton scatters across several segments. The energy from these scatters are summed together into a cluster. While some nH capture gamma rays will register energies below 1.8 MeV due to energy being lost outside the active volume or in a dead segment, we only select those from 1.8 to 2.5 MeV.

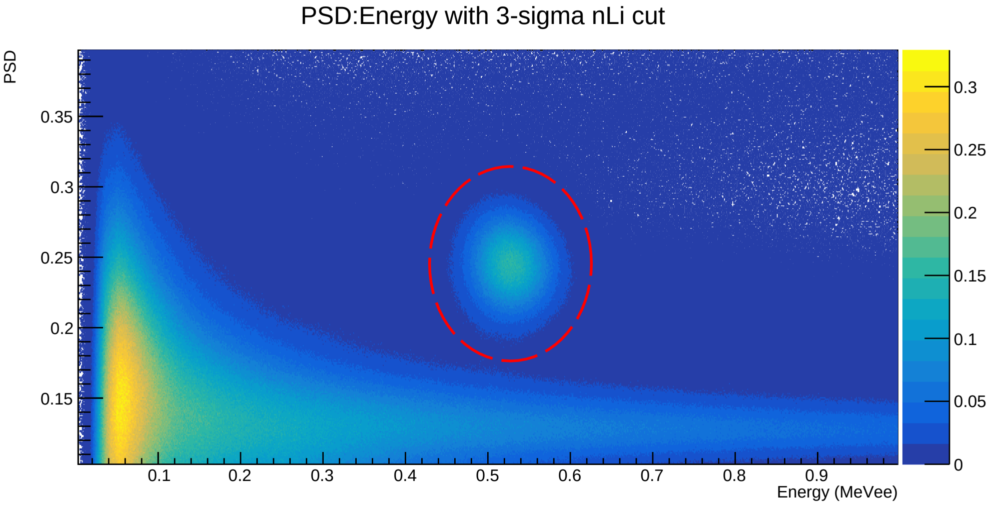

Figure 4.13: PSD and Energy 2-D histogram of single pulses from August calibration data. The red dashed line signifies the 3-σ circular cut on the PSD and energy peaks used for nLi selection.

4.4.1.3 Matching Simulation to Data

To precisely match the PSD and energy values in our simulation to data at the level we need for a precise ^{6}Li doping measurement, we add extra random noise to the simulated energy and PSD spectra as well as an overall offset. To each energy deposit in simulation we add a small Gaussian random term, η,

$$E_s \equiv E + \eta \tag{4.11}$$

where η has a non-zero mean and σ. Varying the Gaussian mean shifts the spectrum positions, and the Gaussian standard deviation smears the resolution of the spectrum. This is done separately for each of the nH energy, nLi energy, and nLi PSD spectra to produce the best match. For the nH energy peak, the Gaussian mean value is only applied once for the clustered sum energy.

The nLi PSD (from Equation 3.3) is smeared in a way to provide comparison to the nLi energy smearing. Starting from the un-smeared simulation PSD, the nLi energy is divided into two parts:

$$E_1 \equiv (1 - PSD) \cdot E, \quad E_2 \equiv PSD \cdot E \tag{4.12}$$

where E_1 and E_2 represent the prompt and delayed fluorescence of the pulse respectively. E_1 and E_2 are then modified independently:

$$E_{1,2}{}' \equiv E_{1,2} + \eta \tag{4.13}$$

where η represents the Gaussian value. Finally, to get our new PSD value, we recombine the prompt and delayed fluorescence energy

$$PSD' \equiv \frac{E_2'}{E_1' + E_2'}. \tag{4.14}$$

In order to find a best fit for these values, a χ^2 minimization method is used on each spectrum for each of μ_{Gaus} and σ_{Gaus}. Without knowing the exact trend of χ^2 as each smearing or shifting value is varied, as long as the changes are small enough, they can be approximated by a 2nd order polynomial via Taylor expansion. The optimal smearing and shifting values are found by fitting to this polynomial and solving for the fit minimum as shown in Figure 4.14. Table 4.8 summarizes the individual optimized smearing and shifting values used in order to match the data to simulation. For some of the plots in Figure 4.14, a polynomial approximation is a poor fit. While we see good agreement between the resulting spectra in Figures 4.15, 4.16 and 4.17, the nLi peaks (energy and PSD) were ultimately fitted to a Gaussian to determine the 3σ range separately for data and simulation, reducing the necessity for a precision match.[1] For the nH distributions, the resulting error from any imperfections from this match is handled in Section 4.4.1.7.

Data Set	nH E smear	nH E shift	nLi E smear	nLi E shift	nLi PSD smear	nLi PSD shift
May '18	0.0482	-0.00016	0.0419	-0.0068	0.0365	0.00401
Aug '18	0.0512	0.0120	0.0452	-0.0023	0.0400	0.00557
Dec '18	0.0551	0.0038	0.0493	-0.0085	0.0444	0.00728
Feb '19	0.0579	0.0133	0.0507	-0.0075	0.0589	0.0524

Table 4.8: Values used on simulation to minimize χ^2 to data. "Shift" refers to the non-zero Gaussian mean of η, and "smear" is related to σ_{Gaus} in MeV.

---

[1] While this results in slightly different cuts for each of the listed spectra, the effect from this is negligible compared to other uncertainties handled later in this section

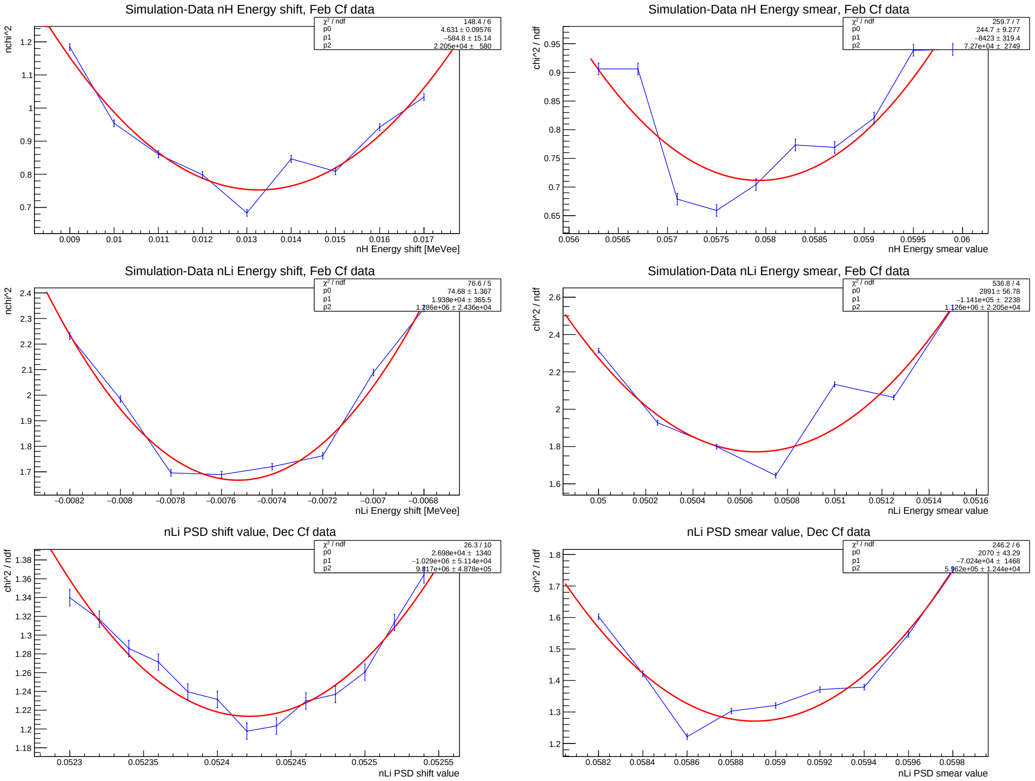

Figure 4.14: Sample optimization curves for the February data set. Each plot shows the χ^2 difference between data and simulation when varying μ and σ of the Gaussian term η. The fit is a quadratic polynomial used to minimize the χ^2 value.

With the relevant parameters of the simulation for each data period optimized, we proceed to optimize the agreement between data and simulation for neutron capture times and nH/nLi ratios by varying only the doping fraction. The previous parameter optimizations were not dependent on doping fraction since each distribution was normalized.

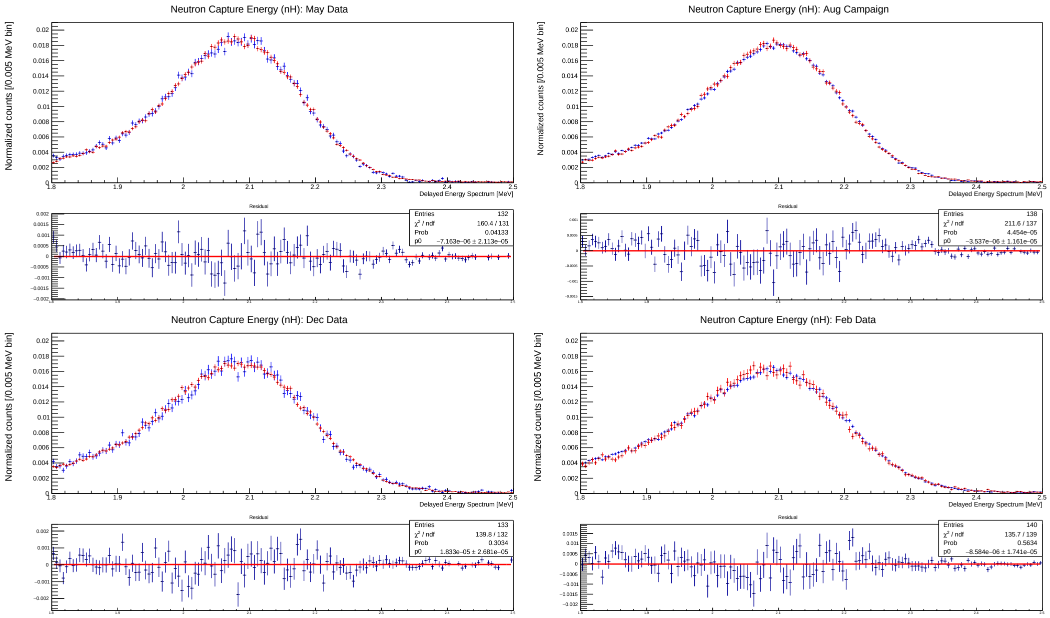

Figure 4.15: Optimized match of nH energy spectra (blue data, red simulation), with residual data - sim below for each of May '18 (top left), Aug '18 (top right), Dec '18 (bottom left), and Feb '19 (bottom right). Red line in residual is a horizontal fit line.

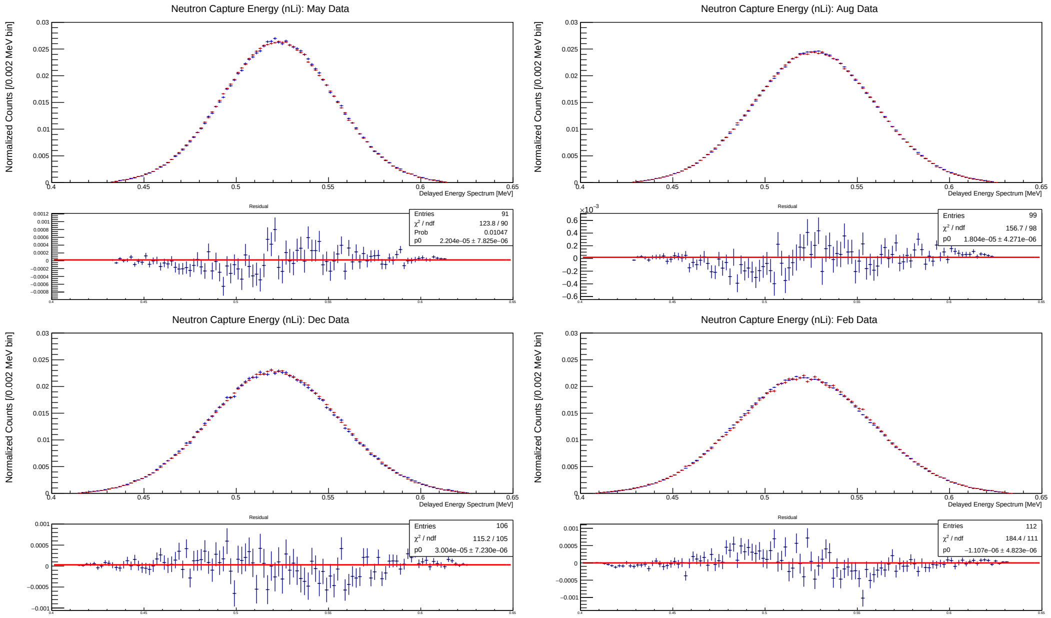

Figure 4.16: Optimized match of nLi energy spectra (blue data, red simulation), with residual data-sim below for each of May '18 (top left), Aug '18 (top right), Dec '18 (bottom left), and Feb '19 (bottom right). Red line in residual is a horizontal fit line.

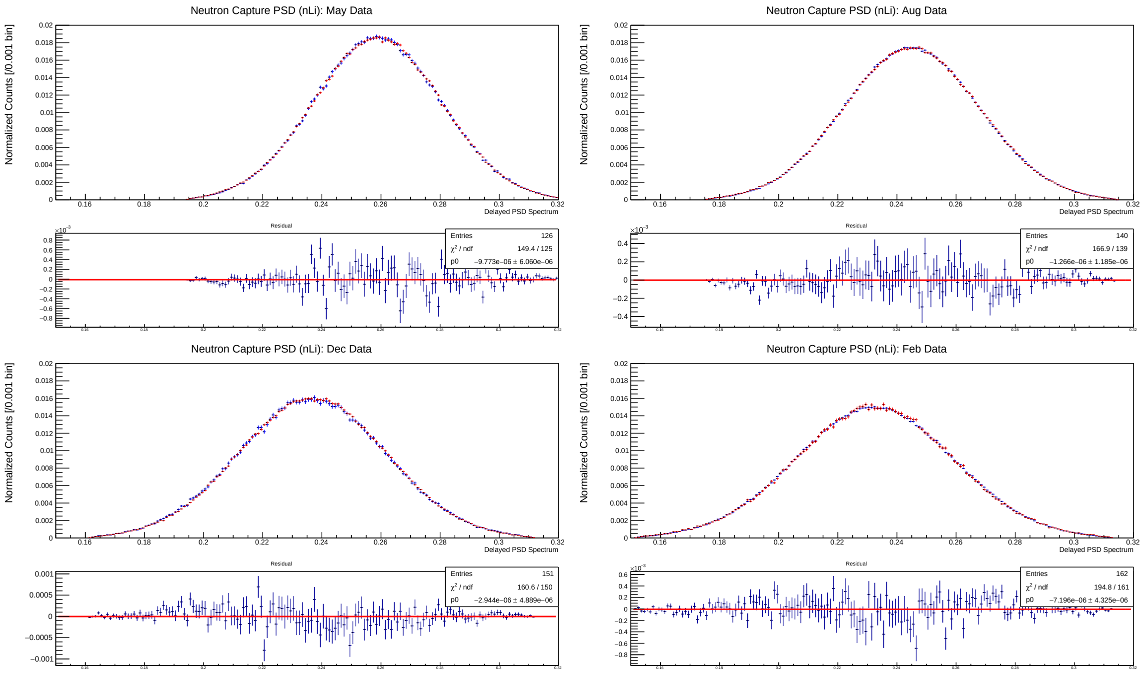

Figure 4.17: Optimized match of nLi PSD distribution (blue data, red simulation), with residual data-sim below for each of May '18 (top left), Aug '18 (top right), Dec '18 (bottom left), and Feb '19 (bottom right). Red line in residual is a horizontal fit line.

4.4.1.4 Capture Ratio

Using the aforementioned event selection in real data, we find the ratio of neutron captures on H to neutron captures on ^{6}Li (nH/nLi), shown in Table 4.9. These cannot be straightforwardly interpreted from Equation 4.3 due to changes in the detector over time, such as the increasing number of nearby dead segments and the efficiency of the hard box cuts on the nH peak. However, the emerging trend of the optimized doping fractions from the simulation is easier to interpret and measure for trends.

Simulating these values at various doping fractions with a similar pattern of dead segments will give a comparable value from one month to another, seen in Figure 4.18. From Equations 4.1 and 4.2, this capture ratio definition is inversely proportional to the ^{6}Li doping fraction. By fitting the simulation to

$$\frac{\text{nH}}{\text{nLi}} = \frac{p_0}{\text{Doping Fraction}} + p_1 \tag{4.15}$$

where p_0 and p_1 are fit parameters. The optimal doping is chosen to be where the fit line crosses the value measured from data. Note that both data and simulation are processed using exactly the same analysis code. These doping fractions are also given in Table 4.9, and summarized with the other methods in Figure 4.24.

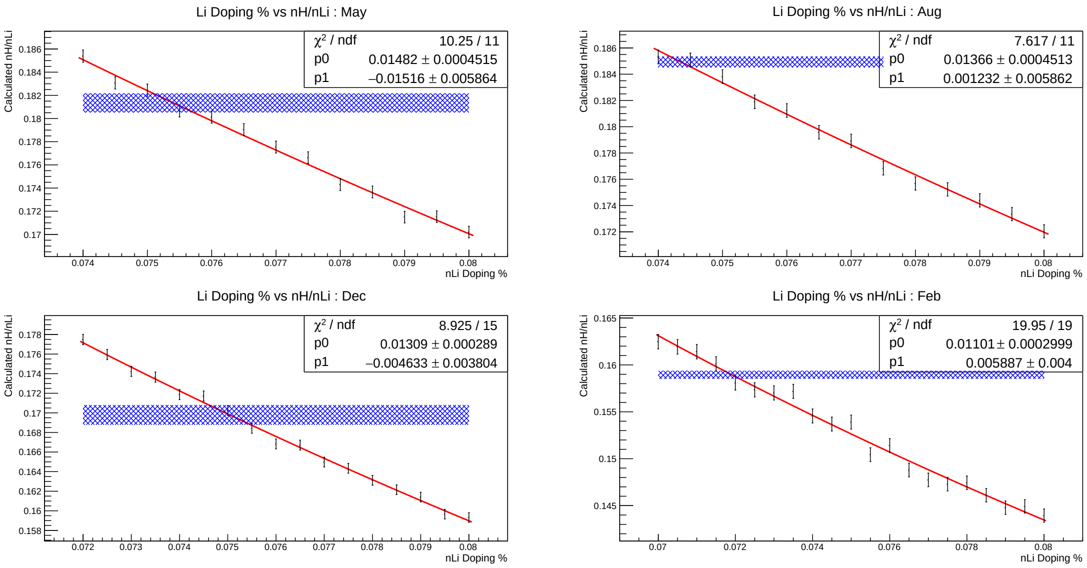

Figure 4.18: nH/nLi capture ratio for various doping fractions given on/off segment orientation for each data set. Black represents the simulated capture ratios, the blue lattice region represents the capture ratio range for data with uncertainty, and the red line is the fit from Equation 4.15.

Data Set	nH/nLi	Doping Fraction Match
May '18	0.1814 ± 0.0008	$(7.54 \pm 0.03) \cdot 10^{-4}$
Aug '18	0.1848 ± 0.0004	$(7.43 \pm 0.02) \cdot 10^{-4}$
Dec '18	0.170 ± 0.001	$(7.50 \pm 0.04) \cdot 10^{-4}$
Feb '19	0.1589 ± 0.0004	$(7.19 \pm 0.02) \cdot 10^{-4}$

Table 4.9: Capture ratios and doping fractions required to match simulation to data for each calibration data set.

4.4.1.5 nH Capture Lifetime

Following Equation 4.5, the capture time of hydrogen yields roughly an exponential decay trend ($y = p_0 \cdot e^{\frac{-t}{\tau}}$), where τ is the capture lifetime. However, non-exponential structure was observed in the simulation at early capture times for nH capture (<20 μs), but was not present in data or in the nLi capture timing structure for simulation or data. While the structure was relatively small compared to the rest of the distribution, fits on the nH capture lifetime in simulation that included this early timing structure gave a different capture time constant than the nLi capture lifetime. However, when a fit range of [20,250] μs was used, this gave agreement between simulation nLi and nH capture times. During this study, we looked at various aspects of the simulation to diagnose this, but didn't have complete conclusions. We moved forward with this study using capture lifetime fits of [20,250] μs to compare simulation and data. This was applied for the nLi capture lifetime fits as well in the following section. Figure 4.19 shows a sample capture time distribution for data and simulation for the Feb '19 data set. The capture lifetimes from these fits are shown in Table 4.10.

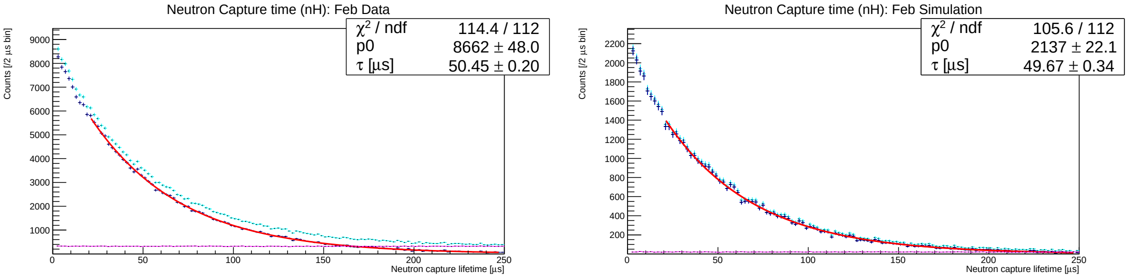

Figure 4.19: Neutron capture time on hydrogen in data (left) and an example simulation (right) for Feb '19 for the correlated time distribution (light blue), accidentals scaled timing distribution (magenta), and the accidentals subtracted curve (dark blue hatches), with red fit line $y = p_0 \cdot e^{\frac{-t}{\tau}}$.

The probability of a neutron capturing in a uniform material in some time interval dt can be expressed as

$$P_{cap}(E) \propto \sigma(E) \cdot \rho \cdot v \cdot dt \tag{4.16}$$

where the probability is function of energy, $\sigma(E)$ is the cross section of the medium, ρ is the density of the material, v is the velocity of the neutron, and $v \cdot dt$ then represents the distance traveled by the neutron. When simplifying

$$\sigma \propto \frac{1}{v} \tag{4.17}$$

$P_{cap}(E)$ loses energy dependence, making the capture time distribution an exponential function of time [89]. Using the simplification in Equation 4.17, the mean free time,

T, for a neutron to capture also simplifies to

$$T = \frac{\lambda}{v} = \frac{1}{\rho \cdot \sigma \cdot v} \propto \frac{1}{\rho} \tag{4.18}$$

meaning the average time to capture is inversely proportional to the number density in the target material.

The evolution of the capture lifetime is affected by the driver location and the number of dead segments, and is not immediately indicative of a doping evolution. These values are used to compare to simulation to find what Li doping fraction will best match the data, with a fit of $\tau = \frac{p_0}{\text{Doping Fraction}} + p1$, in Figure 4.20. The resulting doping fraction matches are in Table 4.10, and plotted with the other methods in Table 4.24.

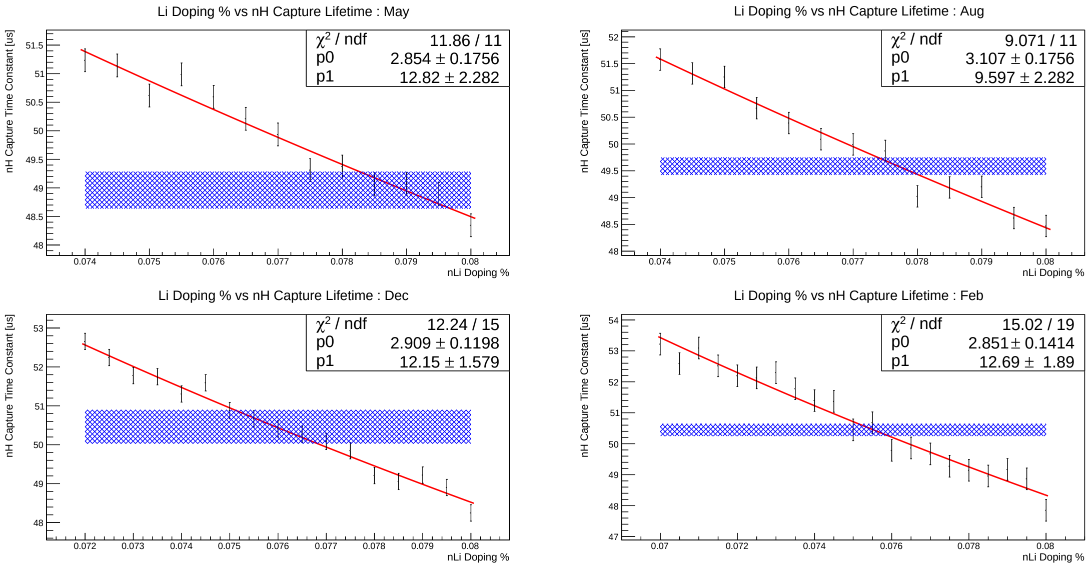

Figure 4.20: nH capture lifetimes for various doping percentages. Black represents the simulated nH capture lifetimes, the blue lattice region represents the nH capture lifetime for data with uncertainty, and the red line is the $\tau = \frac{p_0}{\text{Doping Fraction}} + p_1$ fit.

Data Set	nH Capture Lifetime	Doping Fraction Match
May '18	$49.0 \pm 0.3\ \mu s$	$(7.90 \pm 0.07) \cdot 10^{-4}$
Aug '18	$49.6 \pm 0.2\ \mu s$	$(7.77 \pm 0.03) \cdot 10^{-4}$
Dec '18	$50.5 \pm 0.4\ \mu s$	$(7.59 \pm 0.09) \cdot 10^{-4}$
Feb '19	$50.4 \pm 0.2\ \mu s$	$(7.55 \pm 0.04) \cdot 10^{-4}$

Table 4.10: Neutron capture lifetimes on hydrogen for each calibration data set, and the ^{6}Li doping fraction required to match that value in simulation.

4.4.1.6 nLi Capture Lifetime

Similar methods from the nH capture lifetime are applied here for the nLi capture lifetime, including the exponential fit limited window of [20,250] μs for consistency. Example capture lifetimes for nLi events are shown in Figure 4.21. Data nLi capture lifetimes are summarized in Table 4.11.

Similarly to the nH capture lifetime method for finding the doping percentage, the nLi capture lifetimes from data are compared to simulation to find an optimal Li doping percentage to match data. Figure 4.22 shows these values with a similar fit in the nH τ method. Doping fractions for the nLi τ method are summarized in Table 4.11, and compared to the other methods in Figure 4.24.

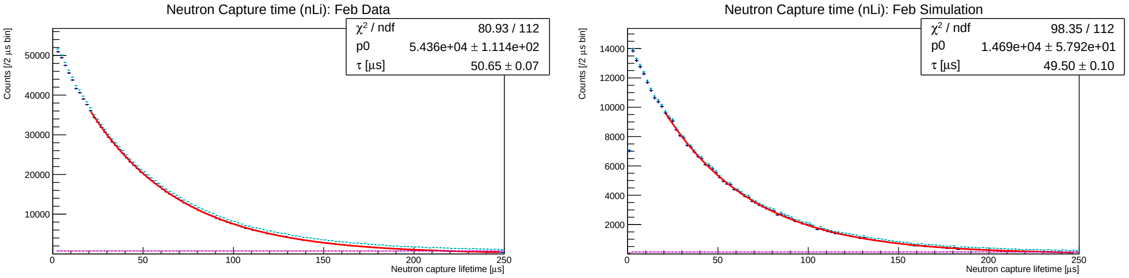

Figure 4.21: Neutron capture time on lithium in data (left) and example simulation (right), for the correlated time distribution (light blue), accidentals scaled timing distribution (magenta), and the accidentals subtracted curve (dark blue hatches), with red fit line $y = p_0 \cdot e^{\frac{-t}{\tau}}$.

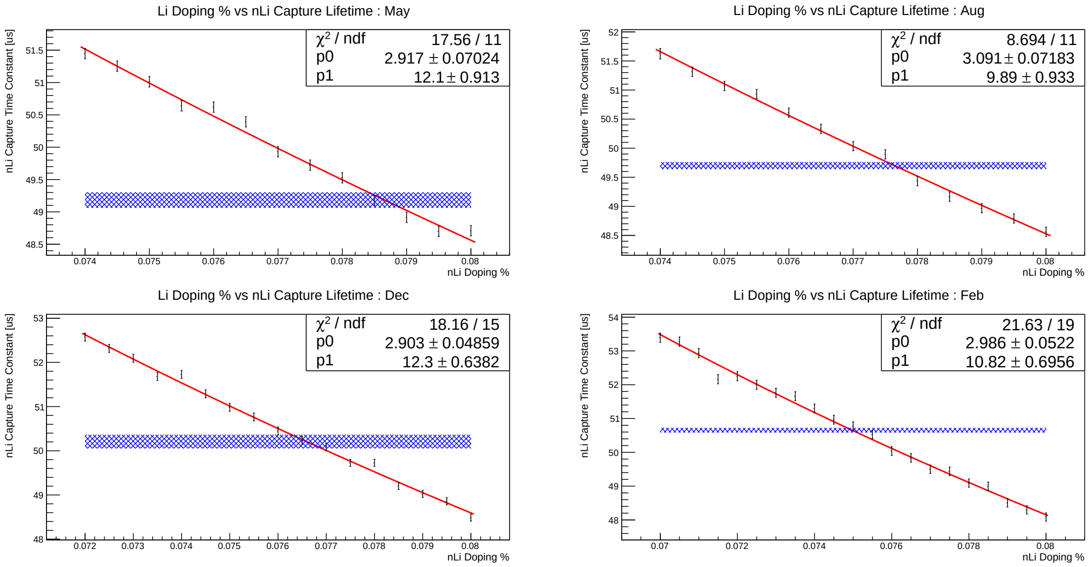

Figure 4.22: nLi capture lifetimes for various doping percentages. Black represents the simulated nLi capture lifetimes, the blue lattice region represents the nLi capture lifetime for data with uncertainty, and the red line is the $\tau = \frac{p_0}{\text{Doping Fraction}} + p_1$ fit.

Data Set	nLi Capture Lifetime	Doping Fraction Match
May '18	$49.18 \pm 0.12\ \mu s$	$(7.87 \pm 0.03) \cdot 10^{-4}$
Aug '18	$49.70 \pm 0.06\ \mu s$	$(7.76 \pm 0.01) \cdot 10^{-4}$
Dec '18	$50.21 \pm 0.16\ \mu s$	$(7.66 \pm 0.03) \cdot 10^{-4}$
Feb '19	$50.65 \pm 0.07\ \mu s$	$(7.50 \pm 0.01) \cdot 10^{-4}$

Table 4.11: Neutron capture lifetimes on ^{6}Li for each calibration data set, and the ^{6}Li doping fraction required to match that value in simulation.

4.4.1.7 Error from nH energy cut

The nH/nLi capture ratio depends on statistical counts of nH and nLi captures. The nH capture energy is taken as 1.8-2.5 MeV, but as seen in Figure 4.15, the energy peak is widening with time. In order to gauge the error introduced from this cut, the August calibration data is re-analyzed using instead a range of 1.0-2.5 MeV for the nH capture energy, Figure 4.23. Using the same simulation smearing and shifting from the 1.8-2.5 MeV analysis, the necessary doping percentages to match the nH/nLi ratio and the nH capture time are then determined, as previously in each study. The determined doping percentage for the ratio method with this new energy range is

$(7.29 \pm 0.02) \cdot 10^{-4}$, which is $\sim 1.8\%$ lower than, and inconsistent with, the doping percentage from Table 4.9 for the Aug '18 data. From Figure 4.23, it is obvious that whereas the nH energy peak had a good match with the optimal smearing and shifting in Figure 4.15, the simulation poorly matches the low energy tail. Including more of that low energy tail ($\sim 1.0 - 1.9$) will cause the nH/nLi ratio for data to increase by 25.5% and simulation by 22.8%, which drives the matching doping fraction in simulation down by $0.14 \cdot 10^{-4}$. We conservatively use this difference of $0.14 \cdot 10^{-4}$ between the two energy cuts as the systematic error to account for the effects driven by the discrepancy in the shape of the nH spectrum. Note that this large leading systematic error from the ratio analysis is absent from the nH lifetime analysis which are expected to be more robust using only the shape of the time distribution.

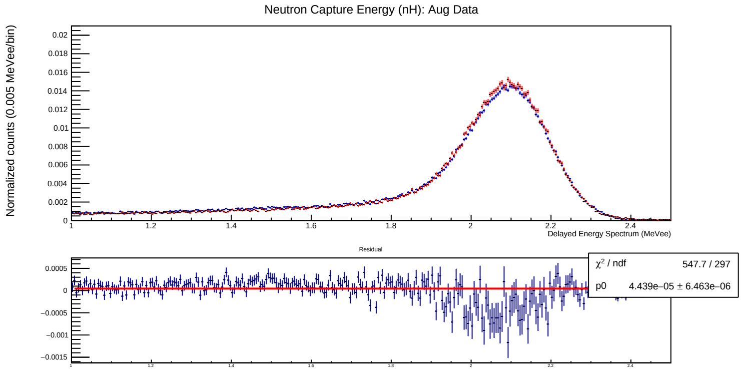

Figure 4.23: nH capture energy for August calibration data. Since histograms are normalized to their integrals, the fit residual around the peak looks worse than previously in Figure 4.15.

4.4.1.8 Error from time cut

The capture time data for nH and nLi were fit only to 20-250 μs to extract the capture lifetimes. However, the nH/nLi ratio is calculated with the inclusion of the early time structures, using a 2-250 μs capture time window. Using the 20-250 μs range to calculate the nH/nLi ratio for data and simulation produces a change in the necessary doping fractions showed in Table 4.12.

Data Set	% Difference from Time Cut	Doping Fraction Difference
May '18	$-0.65 \pm 0.73\%$	$0.05 \cdot 10^{-4}$
Aug '18	$-0.52 \pm 0.37\%$	$0.04 \cdot 10^{-4}$
Dec '18	$-0.52 \pm 1.01\%$	$0.04 \cdot 10^{-4}$
Feb '19	$-0.27 \pm 0.49\%$	$0.02 \cdot 10^{-4}$

Table 4.12: Doping fraction difference for each calibration data set for nH/nLi, using a time window of 20-250 μs instead of 2-250 μs.

Using the 20-250 μs selection for calculating the nH/nLi ratio produces a systematically lower simulation doping fraction to match data, although the uncertainty on this error is relatively large for most of the data sets. The early time structure in the nH capture lifetime showed more nH in simulation than nLi. By reducing the timing window, this lowered the relative number of nH/nLi, which would require a lower lithium doping to match data. However, since this early timing structure in simulation was ultimately never properly diagnosed, we conservatively assign a systematic error of $0.05 \cdot 10^{-4}$ to the doping fraction for the capture ratio method in all data sets.

4.4.1.9 Summary of Doping Methods

Table 4.13 and Figure 4.24 show all the doping percentages for each method used for this study. Each method demonstrates the ^{6}Li doping fraction is decreasing over time. Table 4.14 summarizes the doping fraction loss per year, as well as a percentage loss of ^{6}Li from the detector using this analysis, and also includes an absolute percentage of ^{6}Li loss using only the data from Aug '18, Dec '18, and Feb '18, since the May '18 deployment location was lower in the detector than the other three deployments. The apparent loss of lithium introduces concerns about our IBD detection in PROSPECT analyses, since our detection efficiency changes with the lithium content. The effect of this loss, with a comparison to the implied lithium loss from Section 4.3.2 is covered in Section 4.5.

Data Set	Doping (nH/nLi) $\cdot 10^{-4}$	Doping (nH τ) $\cdot 10^{-4}$	Doping (nLi τ) $\cdot 10^{-4}$
May '18	$7.54 \pm 0.03 \pm 0.15_{sys}$	7.90 ± 0.07	7.87 ± 0.03
Aug '18	$7.43 \pm 0.02 \pm 0.15_{sys}$	7.77 ± 0.03	7.76 ± 0.01
Dec '18	$7.50 \pm 0.04 \pm 0.15_{sys}$	7.59 ± 0.09	7.66 ± 0.03
Feb '19	$7.19 \pm 0.02 \pm 0.15_{sys}$	7.55 ± 0.04	7.50 ± 0.01

Table 4.13: Doping fractions required to match simulation to data for each calibration data set for all 3 methods. nH/nLi ratio systematic errors are from changing the nH energy cut and the timing cut described in previous sections.

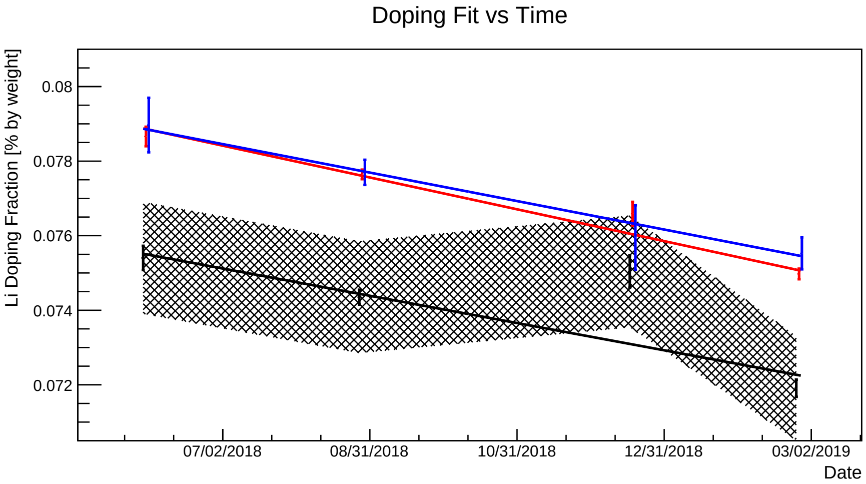

Figure 4.24: Doping percentage match for each calibration data set with linear fit. Blue data points represent the doping percentage to match the nH capture lifetime, red for the nLi capture lifetime, and black for the capture ratio (nH/nLi). Black lattice region around the nH/nLi ratio is the systematic error from changing the nH energy cut or the timing cut described in previous sections.

While the doping fraction determined by the capture lifetime methods agree, the doping fraction determined by comparing the capture ratios is significantly lower outside of error and uncertainties for most of the deployments. All of these methods are dependent on PG4 properly simulating the neutron mobility and neutron cross sections. Additionally, the ratio method in this study is strongly dependent on the energy clustering efficiency for the 2.2 MeV gamma ray from nH, since calculating the nH/nLi ratio relies on accurately counting events within our cut ranges. It is worth noting that the earliest doping from the capture lifetime methods agree with the BNL measured doping fraction of $(0.79 \pm 0.01) \cdot 10^{-4}$, however this value is only trustworthy for immediately after the detector deployment, as evident by the evolution seen in this study. Since the capture lifetime methods accurately predicted the doping fraction from the BNL measurement, and the nLi capture lifetime method has the smallest uncertainty, we will use the doping fraction from that method to benchmark the simulation nLi mobility and capture efficiency in Sections 4.4.2 and 4.4.3.

Method	Doping fraction loss annually	Absolute % loss annually	Absolute % loss annually (Aug-Dec-Feb)
nLi τ	$(0.51 \pm 0.03) \cdot 10^{-4}$	6.5 ± 0.4 %	6.8 ± 0.5 %
nH τ	$(0.46 \pm 0.09) \cdot 10^{-4}$	5.8 ± 1.2 %	5.6 ± 1.4 %
nH/nLi ratio	$(0.44 \pm^{0.05_{stat}}_{0.26_{syst}}) \cdot 10^{-4}$	$5.8 \pm^{0.6_{stat}}_{3.4_{syst}}$ %	$6.0 \pm^{0.8_{stat}}_{5.5_{syst}}$ %

Table 4.14: Loss of ^{6}Li doping fraction determined from linear fit in Figure 4.24. Absolute % loss is given compared to the May '18 doping fraction.

4.4.2 Neutron Singles Mobility

With an appropriate value for the ^{6}Li doping fraction, here we compare how well the PG4 simulation predicts the data neutron mobility. The neutron mobility is a primary driver of IBD selection efficiency non uniformity with position. IBD neutrons can travel into nearby segments, some of which are dead or not included in the analysis, meaning the neutron is not detected. The surrounding dead segment geometry can lower an individual segment's efficiency as much as 25%. Here we demonstrate how well PG4 simulates the neutron mobility across segments using nLi captures from a ^{252}Cf source.

A 1 hour long center ^{252}Cf source deployments from August '18 was used to characterize the neutron mobility effects and verify proper PG4 modeling. The simulation for this study uses the lithium doping fraction of $7.76 \cdot 10^{-4}$ given by the nLi capture lifetime method in the doping study. Similar to the doping study, neutron signals were selected by looking near the nLi capture peak in PSD and energy within 3-sigma of the Gaussian peaks, as shown in Figure 4.25, with applying the PSD and energy smearing to simulation as described in Section 4.4.1.3. In order to eliminate signals not from the ^{252}Cf source, a time equivalent background data set (no source in the detector) is subtracted from the source data.

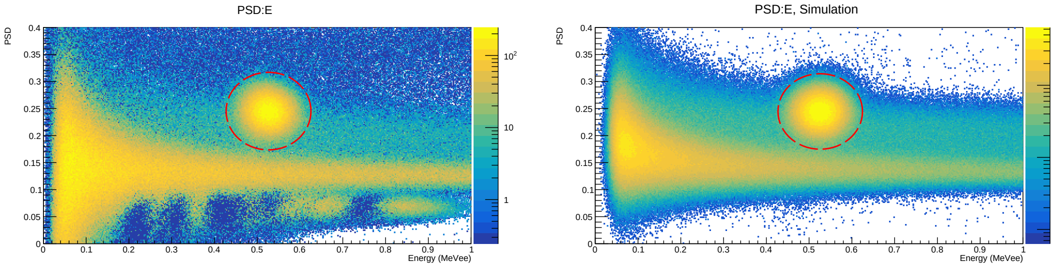

Figure 4.25: PSD and Energy of events near the nLi peak in data (left) and simulation (right). The red dashed lines outline a 3σ circular region in the two axes.

Since the probability of a neutron capture inside the detector is spatially dependent, precise matching of the position resolution in simulation to data is equally as important as matching the PSD and energy. A similar simulation smearing method to the energy and PSD in the doping study is employed for the position resolution for each deployment location. When varying the Gaussian sigma smearing as in Equation 4.11, a best fit can be obtained by finding a minimum χ^2 between data and simulation. Figure 4.26 shows the χ^2 minimization curve to optimize agreement between the simulation and data for the nLi capture position. The result of applying this position resolution smearing is shown in Figure 4.27. The shape of the neutron capture position distribution in Figure 4.27 comes from a combination of the neutron mobility and the detector position resolution.

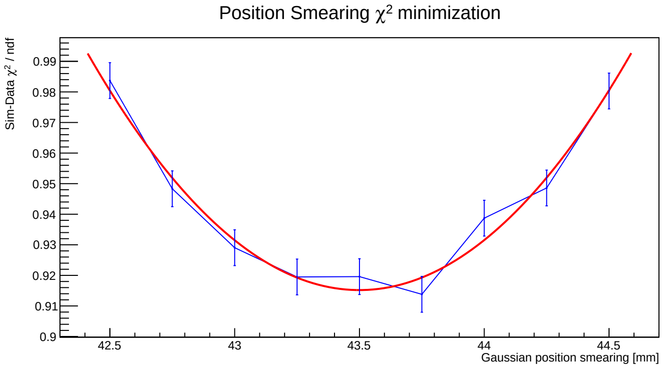

Figure 4.26: Optimization curve for simulation position resolution smearing to match data. χ^2 per degrees of freedom between data and simulation position distributions. The fit is a quadratic polynomial used to minimize the χ^2 value.

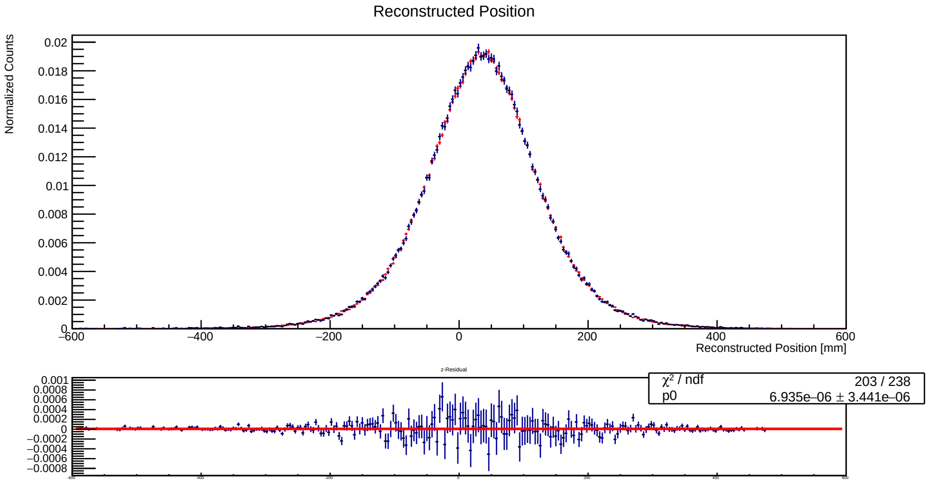

Figure 4.27: Comparison of the reconstructed position distribution of nLi captures from the ^{252}Cf source. Data is in blue, simulation in red. Simulation is smeared by a value determined by the χ^2 minimization demonstrated in Figure 4.26. The bottom plot is the residual between data and simulation. The fit is consistent with 0 at the $< 2\sigma$ level with good χ^2.

With the event selection established, nLi captures within 4 segments are summed together and separated by region. Figure 4.28 demonstrates the fractional contribution of ^{252}Cf neutron captures in different regions surrounding the source deployment axis. PG4 simulated fractional contributions using the custom ^{252}Cf generator are also pictured. The fractional contribution by region is summarized in Table 4.15, showing good agreement between predicted and observed capture fractions for the first three regions, which accounts for ∼99% of nLi captures. The IBD event selection uses events with neutron captures from at most 1 segment away from the primary IBD event, corresponding to regions 1 and 2 in this analysis. The simulation and data agree with each other within statistics at the part per thousand level, which is well below the systematic error for segment-to-segment efficiency differences in the oscillation analysis. It is seen that the simulation properly predicts the segment-to-segment transport of neutrons within high statistics out to 3 segments away from the source position. Simulation shows a slightly larger neutron mobility than data, but is negligible for the PROSPECT IBD analysis. However, this study uses neutrons with energies ∼1 MeV, while IBD neutrons have energies close to ∼10 keV. While this study does not guarantee proper modeling of IBD neutron energies, the match seen gives confidence in the simulation's ability to match the neutron mobility in the detector.

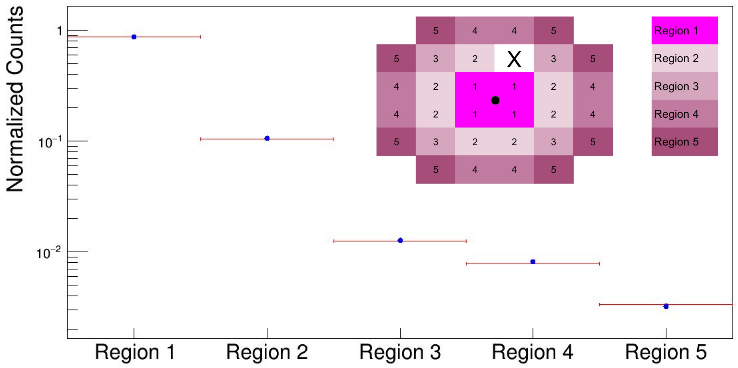

Figure 4.28: Detected nLi capture rates for regions of differing distance to ^{252}Cf location (black circle in region scheme). The inset image defines which segments are assigned to which region bin; in this inset, 'X' indicates an inactive segment. Blue dots represent data, while red lines represent PG4 simulations. As seen in Table 4.15, these two distributions agree within error out to region 3.

	Data	Simulation
Region 1	0.8711 ± 0.0006	0.8708 ± 0.0009
Region 2	0.1056 ± 0.0002	0.1052 ± 0.0003
Region 3	0.01239 ± 0.00008	0.0126 ± 0.0001
Region 4	0.00776 ± 0.00007	0.00809 ± 0.00008
Region 5	0.00309 ± 0.00006	0.00338 ± 0.00005

Table 4.15: nLi capture rates per region in Figure 4.28 for Data and Simulation

4.4.3 Spatial Capture Efficiency

Among the important uses of the ^{252}Cf source for simulation comparison was to map the nLi capture efficiency as a function of position within the detector. Segment-to-segment efficiency variations arose because signal loss is greater near the detector edges. Dead segment locations further exacerbated the position dependence of the efficiency. These must be properly modeled to disentangle the relative rate changes from physics and from those arising from segment dependent efficiencies. We deployed the ^{252}Cf source in two distinct calibration tubes denoted in Figure 4.29, while taking data at multiple points along the segment length during the August 2018 calibration campaign. The measured number of nLi are then compared to the expected number of neutrons determined by the source strength given by the manufacturer (Shown in Appendix 6.1). The deployment locations were chosen to maximize the number of local usable segments while being able to compare deployments near the detector grid center and edge.

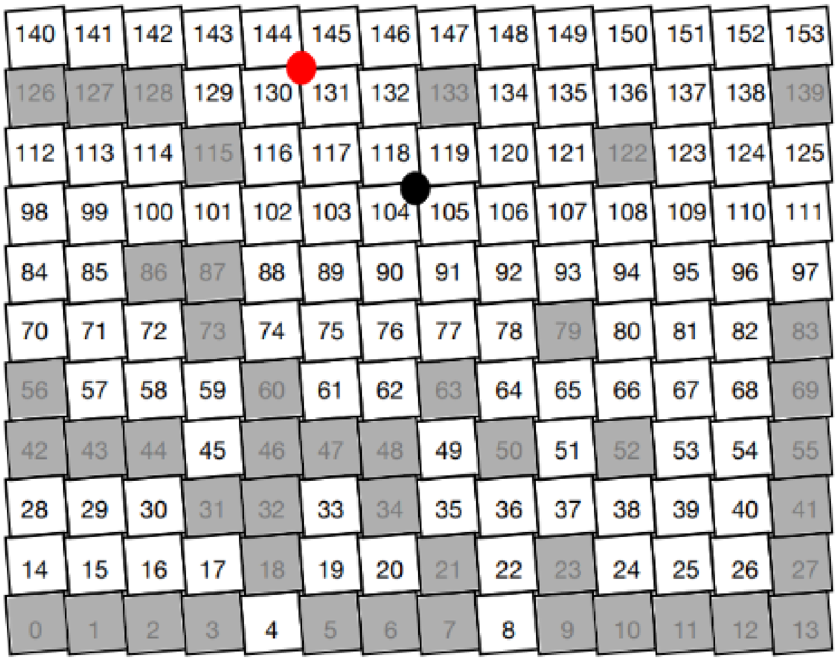
140
141
142
143
144
145
146
147
148
149
150
151
152
153
126
127
128
129
130
131
132
133
134
135
136
137
138
139
112
113
114
115
116
117
118
119
120
121
122
123
124
125
98
99
100
101
102
103
104
105
106
107
108
109
110
111
84
85
86
87
88
89
90
91
92
93
94
95
96
97
70
71
72
73
74
75
76
77
78
79
80
81
82
83
56
57
58
59
60
61
62
63
64
65
66
67
68
69
42
43
44
45
46
47
48
49
50
51
52
53
54
55
28
29
30
31
32
33
34
35
36
37
38
39
40
41
14
15
16
17
18
19
20
21
22
23
24
25
26
27
0
1
2
3
4
5
6
7
8
9
10
11
12
13

Figure 4.29: ^{252}Cf source deployment locations used for the efficiency study.

A ^{252}Cf source is simulated in the PG4 framework at the two deployment locations. Since the neutron target capture fraction is dependent on the scintillator ^{6}Li doping, we use the doping fraction from the method with the least uncertainty from the doping study in the previous section, (7.76×10^{-4} via nLi τ method) as used in the neutron mobility study. Simulation was matched to data with respect to energy, PSD, and position resolution for each deployment position as described in Sections 4.4.1.3 and 4.4.2. In order to account for the uncertainty of the position location, additional error is assigned to simulation efficiencies by varying the simulated source location by 5 mm in either direction, as well as varying the position resolution according the

χ^2 optimization uncertainty, and is included in the error bars for the plots shown in the efficiency studies.

There are two methods of detecting nLi events from a ^{252}Cf source in our detector: coincidence with the prompt fission spectrum (as shown in the previous sections), or by a count of the the nLi single signals without any prompt event tagging. These are dealt with separately in the following sections.

4.4.3.1 nLi Singles Efficiency

To measure the uncorrelated (singles) nLi capture efficiency with respect to the source strength, we must first establish specific nLi selection and counting criteria in data and simulation. In order to eliminate signals not from the ^{252}Cf source, a time equivalent background data (no source in the detector) is subtracted from the source data. Neutron captures on ^{6}Li can be identified by their combined PSD and energy values, as shown previously in Figure 4.25, but in order to eliminate recoil signals exhibiting the same PSD and energy as nLi captures, we must apply extra fits to avoid over counting. Figure 4.30 shows the PSD spectrum in the energy range of the nLi peak. The nLi peak is clear at PSD ~0.25, while gamma-like signals are at lower PSD values. To select nLi value ranges, we apply a Gaussian fit on the right side of the nLi peak to avoid contributions from the lower PSD peak. Figure 4.31 shows the energy values within a 3σ range along the PSD peak. It becomes clear that the singles peak with correct PSD and energy is on top of an exponential looking background. In order to measure uncorrelated nLi events, consideration must be given to the neutron recoils that have the same PSD and energy.

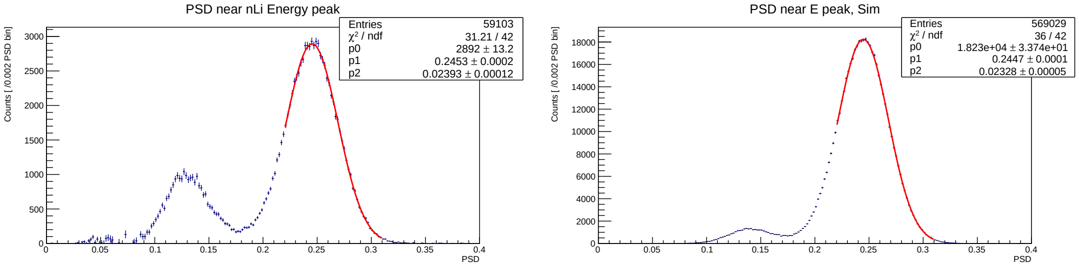

Figure 4.30: PSD spectrum near the nLi peak for data (left) and simulation (right). Gaussian fits are applied to determine cut widths.

The nLi capture energy is best approximated by a Gaussian, but the form of the neutron recoil band in this PSD range fits well to an exponential distribution. In order to get a cleaner count of the nLi singles, we fit the spectrum to a Gaussian plus an exponential. The integral of the energy spectrum above the exponential fit gives the nLi capture count. This integral (out to 3σ in energy as well) is then divided by the expected number of neutrons determined by the source strength and exposure time for each deployment location. Figure 4.32 shows these efficiencies as a function of deployment position.

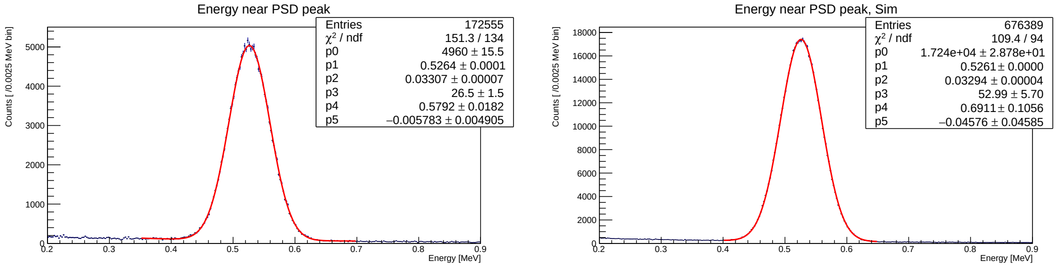

Figure 4.31: Energy spectrum for data (left) and simulation (right), within 3-sigma range of PSD determined in Figure 4.30. The Figures' applied fit is a Gaussian plus an exponential term.

Error from the exponential fit and from counting statistics are accounted for in the error bars in the efficiency plots. Systematic errors from the source include strength uncertainty (1.78% at 1σ), ^{252}Cf spontaneous fission branching fraction (0.26%), and neutron multiplicity per fission (0.6%) for an overall systematic uncertainty of 1.92%, which is not included in data error bars but is shown as a shaded region in final plots. Since the exact number of produced neutrons is available in PG4, these systematics errors do not exist for simulation. Since the intent of this study is to compare simulation to data, the effect of PSD and energy cuts on the efficiency are ignored, as they would be applied to both simulation and data equally. This is because the PSD and energy ranges are selected in terms of distribution sigma.

Error in the simulation due to doping fraction uncertainty is further assessed by calculating the difference in efficiency with a doping fraction of 7.43×10^{-4} from the nH/nLi method, which gave the largest discrepancy. The additional error in simulation from varying the position smearing and location is added in quadrature with the statistical uncertainty. These are shown to have very little effect and are represented in the small error bars on the simulation uncertainty in Figure 4.32.

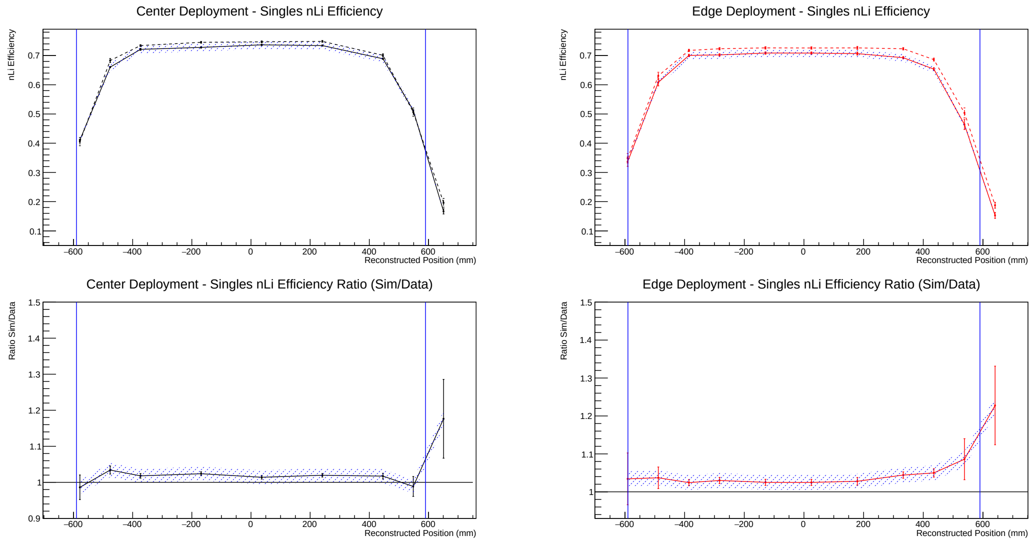

Figure 4.32: nLi singles detection efficiency as described in text comparing Simulation (dashed line) to data (solid line) for the top two Figures for a central (left) and edge (right) source deployment. The shaded region around data values represents the systematic error associated with the source strength uncertainty. The bottom two Figures show the ratio of simulation/data for each point. Segment ends are denoted by vertical blue lines.

If we assume symmetry between the two longitudinal halves of each segment, then we can use the offset in the source positioning to create a more continuous curve, as shown in Figure 4.33. These plots have been fit with a constant out to 500 mm in order to gauge how much the simulation differs from the data. Through these we see that the simulation over predicts the singles nLi efficiency in the center of the detector by $1.9 \pm 0.3\%$ and at the edge by $3.1 \pm 0.3\%$. These fit errors do not include the systematic uncertainty from the source strength. This indicates that the simulation predicts less neutron mobility near the detector edge segments, which would introduce a $1.2 \pm 0.4\%$ error in the segment-to-segment nLi detection efficiency when comparing center segments to edge segments. However, considerations for the edge deployment includes segments that are excluded in the fiducial cut, which excludes the outer ring of segments. The oscillation analysis conservatively assigned a 5% uncorrelated IBD segment uncertainty to encompass this and other effects.

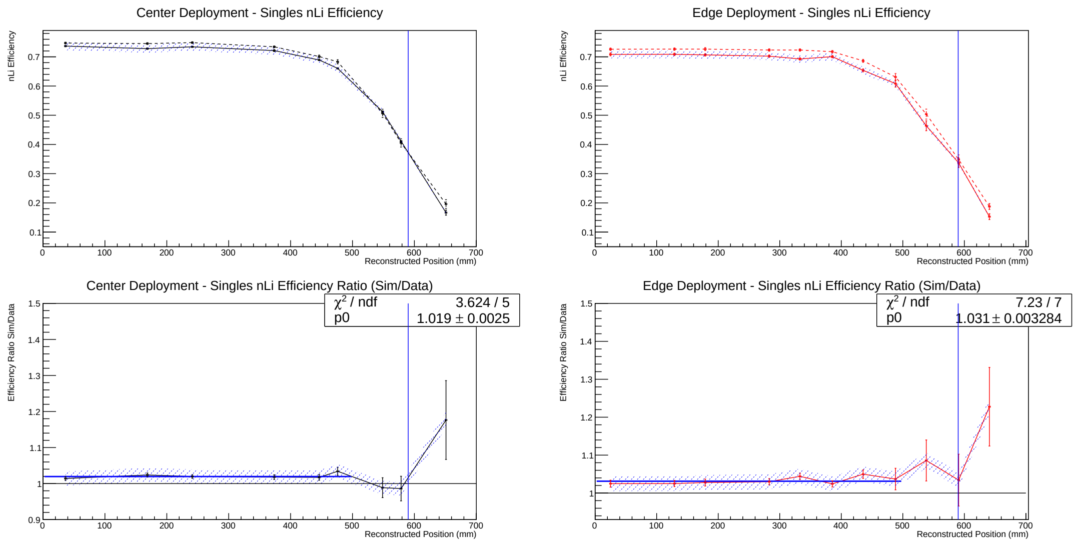

Figure 4.33: nLi singles effficiency curves from Figure 4.32 but using the absolute value along the z-axis, utilizing the source deployment offset to fill out the efficiency points. Segment ends are denoted by vertical blue lines. The ratio plots are fit with a constant out to 500 mm as discussed in text.

The efficiency comparison between data and simulation shows an overall discrepancy past 1σ of systematic uncertainty, but within 2σ near the middle of the segment. It is apparent in Figures 4.32 and 4.33 that the simulation poorly matches data very close to and past the segment endpoints. This would indicate that PG4 poorly simulates the neutron mobility in the regions beyond ±500 mm, or that the position reconstruction is poorly determined for data in this region. However, the IBD analysis excludes events that are outside ±440 mm to reduce backgrounds. This fiducial cut also eliminates regions where the nLi efficiency is no longer in agreement with simulation up to a constant offset. As evident in the ratio plots in Figures 4.32 and 4.33, the simulation/data comparison is stable out to these segment locations.

4.4.3.2 Coincident nLi Efficiency

Since the IBD analysis uses a gamma-like prompt signal with a nLi delayed signal, the coincident nLi efficiency is of interest to gauge the segment-to-segment efficiency. For this, PG4 simulations need to properly predict the neutron mobility and the capture probability of both neutrons and gamma rays. This study assumes that if the simulation can match these values for data with the ^{252}Cf source, then it is reasonable to expect the physics models are close enough to model the IBD interactions. However, the neutron energies from ^{252}Cf and IBD are orders of magnitude different and this study does not guarantee proper modeling.

Selection type	cut values
Prompt Energy	0.5 - 15.0 MeV
Δ t (coincidence)	0.5, 250 μs
Δ t (accidental)	-250, -0.5 μs
Delayed nLi Energy	3σ
Delayed nLi PSD	3σ

Table 4.16: Selection Cuts summary for coincident nLi efficiency. The 3σ cuts on energy and PSD can be seen in Figure 4.25.

Table 4.16 summarizes the selection criteria for nLi events in this analysis. Requiring a time coincidence for event selection eliminates the neutron recoil band in energy seen in the singles measurement, giving a Gaussian as demonstrated in Figure 4.16 from the doping study using a similar selection method. Since this study is sensitive to the absolute number of neutron captures, the time window must be as close to the prompt event as possible without including fast neutron recoils in the data set. In this study, the accidentals window is modified in order to get rid of random coincidences (as before), but also false triggers that are time correlated and not truly accidental. The false triggers, such as those by nH captures, are only removed by precisely placing the accidental time window to mirror the coincidence time window, since we are equally likely to see nLi captures preceding and following nH captures from the same fission. This means that an accidental time window of [-250,-0.5] μs will dual function to remove accidentals and correlated false triggers. In previous studies covered here, this was not a concern as we were looking at trends that were not as sensitive to the absolute counting rate.

We analyze background data (without the source present) in a similar manner as source data to further remove counting events not from the ^{252}Cf source, as

$$N_{nLi} = (C_{Cf} - A_{Cf}) - (C_{BG} - A_{BG}) \tag{4.19}$$

where N_{nLi} is the number of nLi from the ^{252}Cf source, C_i is the correlated counts for data set i, and A_i is the accidental counts for data set i. Dividing this by the expected number of neutrons from the ^{252}Cf source for each deployment position results in the efficiency curves seen in Figures 4.34 and 4.35, similar to the singles efficiency study. As with the singles study, the effect of PSD and energy cuts on the efficiency are ignored due to the fitting selection. The error from the inclusion of a time correlation component is assumed to be identical between data and simulation, because we use the ^{6}Li doping fraction for simulation that matched data for the nLi timing distribution.

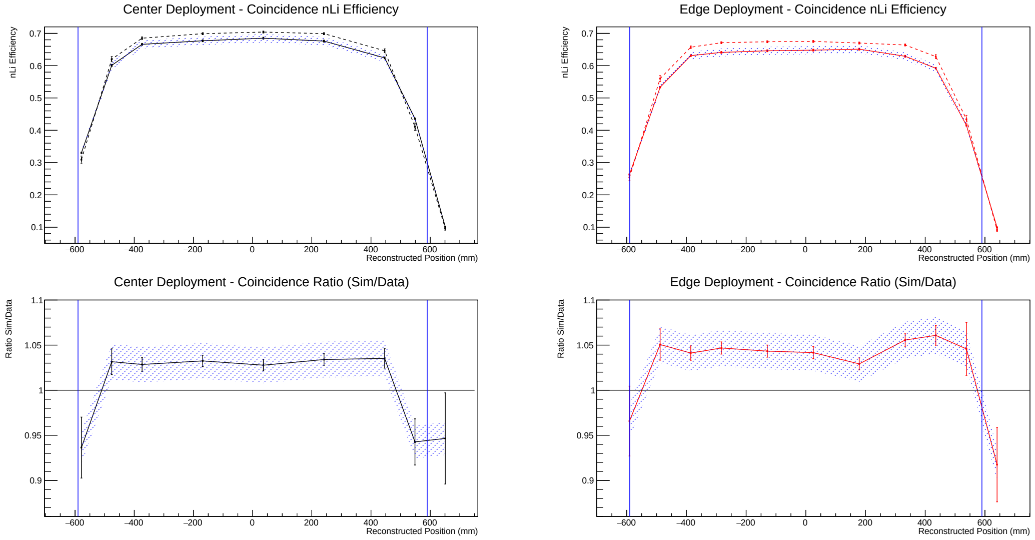

Figure 4.34: nLi coincidence detection efficiency as described in text comparing Simulation (dashed line) to data (solid line) for the top two Figures for a central (left) and edge (right) source deployment. The bottom two Figures show the ratio of simulation/data for each point.

As expected, the coincidence nLi efficiency is lower than the singles efficiency in the previous section due to folding in the gamma ray event detection efficiency. In the singles efficiency study, the simulation predicts a higher nLi efficiency close to the segment ends. For this study, close to the end of the segments, it is clear that the data and simulation do not match the gamma transport and detection well, as the overall nLi detection efficiency ratio drops significantly close to the segment ends. This might indicate that near the segment ends, PG4 simulations poorly recreate the gamma ray transport and detection efficiency, since this study directly relies on identifying neutrons correlated to fission gamma rays. However, the intent of this study was to verify the neutron dynamics in PG4, at least within the fiducial volume.

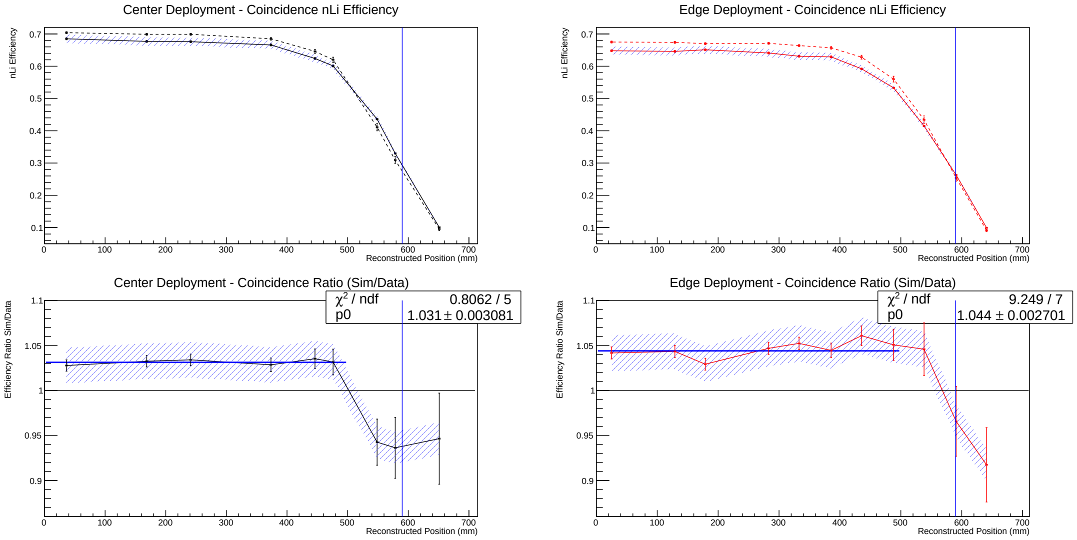

Figure 4.35: nLi coincidence efficiency curves from Figure 4.34 but using the absolute value along the z-axis, utilizing the source deployment offset to fill out the efficiency points. The ratio plots are fit with a constant out to 500 mm as discussed in text.

Once again we see that the efficiency is relatively stable within error out to ±500 mm for both center and edge deployments, and the difference between data and simulation is outside of 1σ but within 2σ of the systematic uncertainty of the source data. Since the PROSPECT analysis makes a fiducial cut of ±440 mm, we conclude that the measured and simulated nLi efficiency stability agree across the fiducial region up to a constant offset.

The fits on the ratio plots indicate simulation over predicts the coincidence nLi efficiency by $3.1 \pm 0.3\%$ at the center of the detector and $4.4 \pm 0.3\%$ near the edge segments, for a difference of $1.3 \pm 0.4\%$, similar to the difference of $1.2 \pm 0.4\%$ seen in the singles efficiency study. This is easily covered by systematics assigned by the various analyses.

4.5 Indications and Effects of Lithium Loss

Although tests performed prior to constructing the detector showed that the microemulsion used to keep the ^{6}Li in solution was stable, this is called into question by indications from detector evolution by measuring the capture lifetime from cosmogenic signals and simulation predictions. In Section 4.4.1, we showed that the data-simulation comparisons predicted the BNL measured ^{6}Li doping fraction, but also showed a decrease in this doping fraction at a rate of >5.5% annually, as shown in Table 4.14.

^{6}Li and ^{227}Ac were both introduced into the detector via aqueous chlorides. Previous analysis of decay rates in the PROSPECT detector by Danielle Berish indicated a reduction in ^{227}Ac rates greater than expected by the half-life and may be interpreted as ^{227}Ac falling out of the solution. The ^{227}Ac decay rate analysis found an excess loss of ^{227}Ac in the detector of $2.7 \pm 0.4\%$ annually [80]. When splitting the detector into a top and bottom half, she found a larger rate of loss in the top of the detector: $4.1 \pm 0.5\%$ and $0.5 \pm 0.6\%$ loss annually for the top and bottom halves respectively.

The ^{227}Ac decay rate analysis could be interpreted as showing a slower loss of aqueous chlorides in the detector than the losses shown in Table 4.14, although the two results are within a 2σ discrepancy. If the loss of ^{227}Ac and ^{6}Li in the detector are due to a displacement of segment scintillator with mineral oil from the PMT housings, then the effective losses could be accelerating with time. Depending on the extent of this possible trend, it might be difficult to gauge this with so few data points from Section 4.4.1. While the ^{227}Ac loss does not completely agree with these results, there may be overlapping or separate causes.

In order to make a more granular comparison to the ^{227}Ac rate trend, we will convert the nLi capture lifetime evolution trend seen in Section 4.3.2 to a predicted lithium content here.

4.5.1 Lithium Loss Prediction from Cosmogenic Neutrons

Both the ^{227}Ac and ^{6}Li were expected to be held in solution by the same chemistry. The increase in the nLi capture lifetime from Section 4.3.2 is indicative of a loss of ^{6}Li falling out of the LiLS. Figure 4.8 and 4.9 showed the lifetime constant (τ) evolution for each row. Each individual row has a differing number of available segments, further changing the statistics from row to row. A summary of the linear fits from the nLi capture lifetime trends for each row was shown in Figure 4.10 and Table 4.5.

Figures 4.10 and Table 4.5 demonstrated a gradient that increases from top to bottom, suggesting a higher loss rate of ^{6}Li in the top of the detector. The ^{227}Ac decay rate analysis also found a similar gradient, with the greater rate losses higher in the detector. The reason is suspected to be some combination of ^{6}Li and ^{227}Ac leaving the LiLS or scintillator being replaced by mineral oil from PMT housing leakage, which might affect the bottom row segments more if related to the number of "dead segments."

The rate of lithium density reduction in the LiLS can be calculated using the change in the neutron capture lifetime. The lithium loss rate can then be compared to the loss of ^{227}Ac as well, since they were expected to change by a similar amount. Calculating the lithium loss rate requires relating the capture lifetime to one of the contributing target's number density. Capture lifetimes can be represented inversely proportional to the number density ρ_i of the target,

$$\frac{1}{\tau_i} = k\rho_i \tag{4.20}$$

with k being a proportionality constant. Recalling from Equation 4.7 that capture lifetimes add in reciprocal, we can represent the capture lifetime measured in the detector in terms of the number density of ^{6}Li:

$$\frac{1}{\tau} = k\rho_{Li} + \frac{1}{\tau_{ee}} \tag{4.21}$$

where τ is the measured lifetime, ρ_{Li} is the number density of ^{6}Li in the detector, let k be the proportionality between $\frac{1}{\tau_{Li}}$ and ρ_{Li}, and τ_{ee} is the contribution of the capture lifetime from all elements other than ^{6}Li in the detector. Solving for ρ_{Li}

$$k\rho_{Li} = \frac{1}{\tau} - \frac{1}{\tau_{ee}} \tag{4.22}$$

$$\rho_{Li} = \frac{1}{k\tau} - \frac{1}{k\tau_{ee}} \tag{4.23}$$

In order to find a rate in time, we take the time derivative:

$$\frac{\partial \rho_{Li}}{\partial t} = \frac{\partial}{\partial t}\left(\frac{1}{k\tau}\right) - \frac{\partial}{\partial t}\left(\frac{1}{k\tau_{ee}}\right) \tag{4.24}$$

Using the model that scintillator is being replaced with mineral oil in the detector, we assume the contribution of this change in the hydrogen and chlorine density don't change τ_{ee} measurably compared to τ. Since τ_{ee} is assumed to not change in time, equation 4.24 becomes

$$\frac{\partial \rho_{Li}}{\partial t} = -\frac{1}{k\tau^2}\frac{\partial \tau}{\partial t} \tag{4.25}$$

In order to turn Equation 4.25 into a percentage rate, we scale both sides by the lithium density, using Equation 4.23 on the right side and rearranging we get

$$\frac{1}{\rho_{Li}}\frac{\partial\rho_{Li}}{\partial t} = -\frac{\partial\tau}{\partial t}\left(\frac{1}{\tau - \frac{\tau^2}{\tau_{ee}}}\right) = -\frac{1}{\tau}\frac{\partial\tau}{\partial t}\left(\frac{1}{1-\frac{\tau}{\tau_{ee}}}\right) \tag{4.26}$$

If $\frac{\tau}{\tau_{ee}} << 1$, meaning the contribution from ^{6}Li almost solely dictates the capture time, then the rates scale in a simple manner. In our case, the values are $\tau = 49.52 \pm 0.06\ \mu$ s from the data start date for the full detector and $\tau_{ee} = 248.7 \pm 1.1\ \mu$s from simulation of scintillator absent of ^{6}Li. This makes the factor

$$\frac{1}{1-\frac{\tau}{\tau_{ee}}} = 1.249 \pm 0.002 \tag{4.27}$$

Using Equation 4.26 and the value of τ for each row, we can model the loss of ^{6}Li from the change in the capture lifetime. Table 4.17 gives these calculated annual loss values for ^{6}Li, and Figure 4.36 shows these values compared to the ^{227}Ac loss rates. We see a faster loss of ^{6}Li in this study than the loss of ^{227}Ac. Although the mechanism for these effects is not clear, and the magnitude of these effects does not match, it is obvious that there is a distinct loss of both ^{6}Li and ^{227}Ac that varies within the detector volume.

Row	^{6}Li loss annually
1	1.5 ± 0.6 %
2	1.6 ± 0.6 %
3	3.2 ± 0.7 %
4	4.3 ± 0.5 %
5	2.9 ± 0.4 %
6	3.2 ± 0.5 %
7	3.7 ± 0.4 %
8	4.3 ± 0.4 %
9	4.1 ± 0.5 %
10	8.4 ± 0.4 %
Detector Average	3.96 ± 0.15 %

Table 4.17: Percentage ^{6}Li loss annually from Figure 4.36.

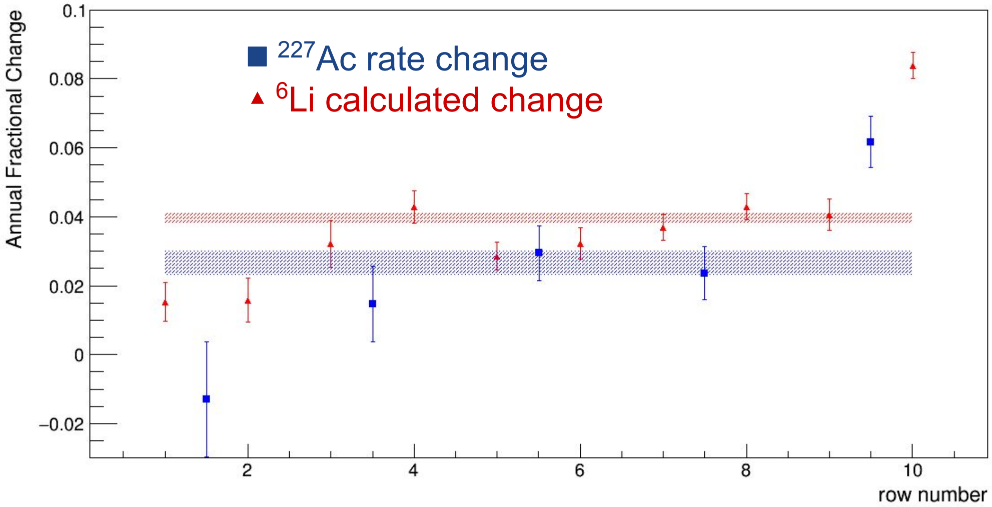

Figure 4.36: Calculated fractional loss in ^{6}Li (red) and ^{227}Ac (blue) [80] per row. The shaded regions represent the full detector averages.

The doping study predicted a lithium loss of $6.8 \pm 0.5\%$ annually from the nLi capture lifetime method when comparing data from a single location near rows 7 and 8. This lithium loss predicted by the cosmogenic nLi lifetime evolution is much lower, predicting $3.96 \pm 0.15\%$ lithium loss in the entire detector, which is close to the average seen between rows 7 and 8 for the same method. While the discrepancy between these two methods is outside of error, this conversion of the nLi capture lifetime method is advantageous to measure the gradient of lithium and the variation between segments.

4.5.2 Effects of Lithium Loss on IBD Efficiency

The evolving nLi capture lifetime introduced changes in the IBD detection efficiency discussed in Sections 4.3.2.1 and 4.3.2.2, and were shown to be negligible within our assigned systematic uncertainties for the PROSPECT analyses. However, losing ^{6}Li in the detector introduces further efficiency variations since there are fewer neutron capture targets. For the IBD analysis, this introduces an error associated with the segment to segment efficiency variation within the detector, which is measurable if we know the change in the nLi capture efficiency.

We can calculate the probability of an nLi capture if we assume a given neutron energy by using the relative densities and cross sections of each capture target as

$$P_{nLi} = \frac{n_{Li}\sigma_{a,Li}}{\sum\limits_{i} n_i \sigma_{a,i}} \tag{4.28}$$

where n_i is the number density and $\sigma_{a,i}$ is the neutron capture cross section for target i. For this calculation, we will assume thermal neutrons, and use the 5 most dominant capture targets, with their values listed in Table 4.18. Assuming that chlorine is lost in the same manner as lithium in the detector, the density of ^{35}Cl and ^{37}Cl are determined by the ^{6}Li doping, using that the ^{6}Li was 95% enriched, and the natural abundance of ^{35}Cl (75.8%) and ^{37}Cl (24.2%). By varying the density of ^{6}Li in this calculation, we can predict the nLi capture efficiency changes due to the lithium content, excluding detector effects.

Capture Target	n (10^{22}/cm^3)	$\sigma_{a,i}$ (b)
^{6}Li	varies	944
H	5.66	0.334
^{35}Cl	$0.758\times n_{Li}$	4.40
^{37}Cl	$0.242\times n_{Li}$	4.42
^{12}C	4.14	0.00388

Table 4.18: Values used to determine the thermal neutron capture probability on ^{6}Li [74, 88].

For the nominal ^{6}Li doping fraction of $7.9\cdot 10^{-4}$ from both the nLi capture lifetime method in the doping study, as well as the BNL measurement [74], the nLi capture efficiency is 75.46%. For the IBD analysis, the change in our efficiency introduces error when subtracting the background spectra. However, the average reactor on cycle is typically less than 30 days apart from the average reactor off cycle for this subtraction. If we assume the largest doping study change of 6.8% per year (0.56% per 30 days), this reduces the nLi capture efficiency to 75.37% in 30 days. This is a relative decrease of 0.12% in efficiency, which is well below the 0.25% statistical error for a 3 year data set used in the IBD analysis.

The oscillation analysis requires proper modeling of segmet-to-segment variations, which was accounted for with a 5% uncorrelated IBD rate uncertainty for a ∼3 month data set. If we assume all segments had the same doping fraction at the start of data taking, we can use this efficiency model to predict the segment-to-segment variation in the IBD detection efficiency caused by lithium loss. By taking the largest difference in lithium loss across the detector from Table 4.17, we calculate the largest variation in detection efficiency between any two rows for a 3 month data taking period, as well as a 1 year difference, as shown in Table 4.19. Rows 1 and 10 have the largest difference in predicted lithium loss across the detector, but since row 10 is excluded by the analysis fiducial cut, we also evaluate the difference between rows 1 and 4. It is seen that these values are still significantly below the conservative 5% segment IBD efficiency systematic uncertainty used by the oscillation analysis, even out to a 1 year data set.

Data set	Eff after 3 Months	Eff after 1 year
Row 1	0.7539 ± 0.0002	0.7522 ± 0.0009
Row 4	0.7529 ± 0.0002	0.7476 ± 0.0008
Row 10	0.7512 ± 0.0002	0.7403 ± 0.0007
Row 1-4 ΔEff	$0.13 \pm 0.03\%$	$0.612 \pm 0.17\%$
Row 1-10 ΔEff	$0.35 \pm 0.03\%$	$1.58 \pm 0.15\%$

Table 4.19: Change in IBD efficiency between rows 1, 4, and 10 in the detector due to the loss of lithium in the detector from Table 4.17 after 3 months and 1 year. These values assume a 0.7546 starting efficiency for each row, based on a ^{6}Li doping fraction of $7.9 \cdot 10^{-4}$.

4.6 Conclusions

Neutron detection provides a way to reduce backgrounds for the IBD analysis, as well as track detector stability and benchmark the PG4 simulations. Cosmogenic neutrons provided a source for tracking stability in the PROSPECT detector. While the energy resolution was worsening over time, the use of a smeared energy mitigated the change from degradation over time within the required $10\%/\sqrt{E}$, and linear trends in the resolution predict that this limit would not be reached until after the 3 year data goals of the PROSPECT detector.

The neutron capture lifetime was measured to change over time and showed a gradient in the detector. The uncertainty this causes in the IBD detection efficiency (overall and segment-to-segment) is small compared to the systematic and statistical uncertainties in the published data sets. This lifetime change further implied loss of lithium in the scintillator that was still below the allotted uncertainties for PROSPECT analyses. However, these trends are problematic for the sake that they were unexpected and not fully understood. At present, there is collaboration effort to determine the cause of the lithium loss and scintillator degradation.

Comparing ^{252}Cf data and PG4 simulations accurately predicted the measured scintillator ^{6}Li doping fraction from production, and was used as a second measurement of scintillator degradation. These PG4 doping fractions give good agreement of the nLi mobility when compared to data, which is key to simulating the segment-to-segment efficiency map for the oscillation analysis. The neutron rate is consistenw ith expectation from the source within 2σ where the dominant error is the source strength. This doping fraction, in addition to the other response characterizations, were used for a final PG4 IBD simulation to produce the segment-to-segment efficiency map for the IBD analysis.

CHAPTER 5

CF-252 NEUTRON MULTIPLICITY

The neutron multiplicity from ^{252}Cf serves as a reference for other actinide neutron multiplicity measurements. The average neutron multiplicity is commonly determined by independent measurements of the fission rate and absolute neutron output, and deviations and uncertainties in our understanding of the ^{252}Cf neutron multiplicity distribution impacts the neutron balance and economy of reactor and instrument designs [90]. Information on the decay of ^{252}Cf was covered in Section 4.2.

Here we give an independent analysis of the neutron multiplicity distribution from ^{252}Cf spontaneous fission using the PROSPECT detector. A comparison is made to the combination of previous multiplicity distribution measurement evaluations, compiled by Holden and Zucker in 1984 [91, 92], as well as Santi and Miller in 2008 [93].

5.1 Event Selection

Given our detector design and the source placement (shown in Figure 4.12 for the August 2018 deployment), we expect the source-emitted gamma rays and neutrons to be completely contained in our detector volume, with the caveat that some may deposit energy in dead segments. The nLi detection efficiency for this deployment was determined in Section 4.4.3.1, while the gamma energy loss is minimal and we anticipate will not affect our measurement. We detect neutrons from ^{252}Cf spontaneous fissions, which will thermalize and capture with a capture lifetime of 49.70 ± 0.06 μs determined in Section 4.4.1.6. We use a capture time window of [1, 300] μs following prompt spontaneous fission gamma rays that accompany a fission event. We cannot distinguish between multiple gamma rays and a single gamma ray scattering multiple times, so we sum all the energy deposits within a few ns of each other and possibly distributed over multiple segments into a "cluster." A large number of neutrons in our detector capture on hydrogen, producing a 2.2 MeV gamma ray. To remove this class of events from the fission-like events, we use a 3.0 MeV cut on our reconstructed prompt gamma ray "cluster" energy, described in Section 3.2.9. Otherwise, these gamma rays create a false fission trigger, since they are often followed by correlated neutron captures on lithium from the same fission event. Figure 5.1 shows the resulting total prompt gamma ray energy spectrum for events preceding a neutron capture with the nH peak easily visible around 2 MeV. Another source of false fission triggers comes from neutron recoils on ^{12}C. Neutron scatters excites the ^{12}C which de-excites, releasing a 4.4 MeV gamma ray. The neutron then thermalizes and captures which mimics our detection prompt-delay scheme. Other neutron and fission induced signals at higher energies and their estimated effect is discussed in Section 5.3.2. Instead of using a higher energy cut to eliminate these signals, we veto subsequent prompt signals are less than 500 μs after the previous prompt signal that was not cut. Any gamma rays associated with the alpha decays have energies lower than our 3.0 MeV energy cut and the alpha particles are contained in the aluminum source capsule [94].

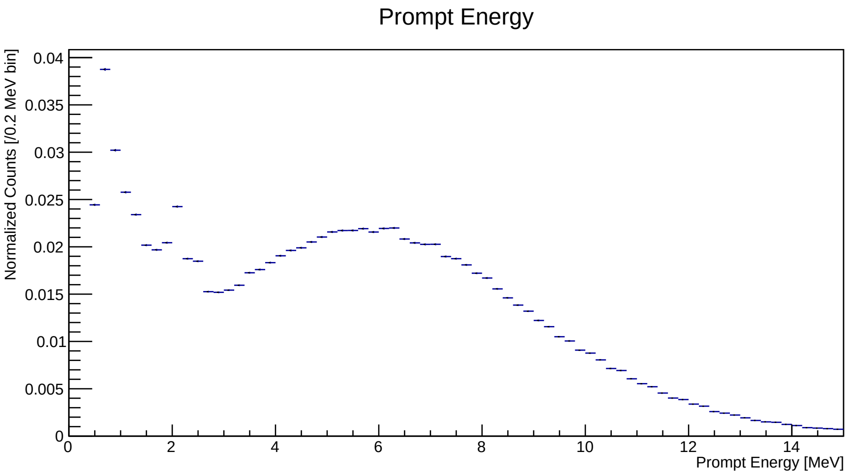

Figure 5.1: ^{252}Cf spontaneous fission gamma energy spectrum selection for non-zero neutron multiplicities. Signals at low energies and nH captures motivates the energy selection of E > 3.0 MeV to eliminate signals not from ^{252}Cf spontaneous fission.

Studies from Nifenecker in 1972 suggested a positive linear correlation of gamma energy to neutron multiplicity [95]. However, recent and more precise studies have shown a weak correlation between the prompt gamma ray multiplicity (and gamma ray energy) and neutron multiplicity [96], which would suggest that the prompt gamma ray energy cut would not influence our measurement.

Figure 5.2 shows the coincidence nLi multiplicity distribution from the event selection described. The high 0 multiplicity of ∼3 million counts is obviously suspicious at this stage. Having ^{252}Cf fission events with no emitted neutrons is expected from previous multiplicity measurements [91, 93]. The inefficiency of our neutron detection drives the multiplicity distribution lower. In the following sections we will address all the required corrections in the order which they are applied to go from the measured nLi distribution to the emitted neutron multiplicity distribution.

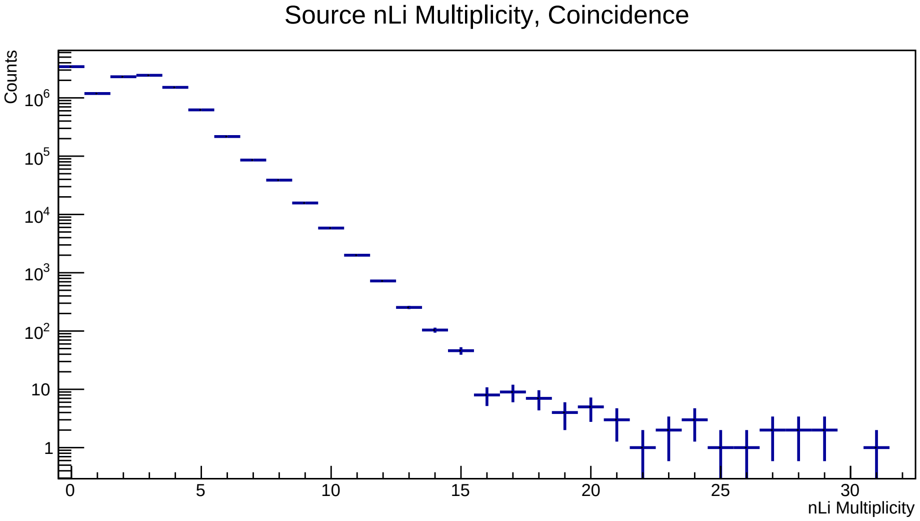

Figure 5.2: Multiplicity of nLi captures coincident with a fission trigger. Error bars are statistical. The excess of events with zero multiplicity is discussed in the text.

5.2 Accidentals Pileup Treatment

There is a chance that we detect neutrons from other sources in our coincidence time window, artificially increasing the multiplicity for that fission. Additionally, neutrons from other fissions could potentially be included in the correlated time window for a given fission. In order to correct for this, we use a time window uncorrelated to the fission to sample ambient neutron multiplicities.

Assume a probability distribution A_i for detecting i neutrons in our coincidence time window that did not come from the source spontaneous fission. Then the total detected number of neutrons C_k is

$$C_k = \sum_{i}^{k} M_i A_{k-i} \tag{5.1}$$

where M_i is the distribution of neutron multiplicities from source fissions. We can think about this as a matrix operation,

$$\mathbf{C} = \mathbf{A}\mathbf{M} \tag{5.2}$$

$$\begin{bmatrix} C_0 \\ C_1 \\ \vdots \\ C_k \end{bmatrix} = \begin{bmatrix} A_0 & 0 & 0 & \dots & 0 \\ A_1 & A_0 & 0 & \dots & 0 \\ \vdots & \vdots & \vdots & \ddots & \vdots \\ A_i & A_{i-1} & A_{i-2} & \dots & A_0 \end{bmatrix} \begin{bmatrix} M_0 \\ M_1 \\ \vdots \\ M_i \end{bmatrix}, \tag{5.3}$$

and to determine the emitted neutron distribution M_i, we simply need to invert matrix $\mathbf{A}$ to get

$$\mathbf{M} = \mathbf{A^{-1}}\mathbf{C}. \tag{5.4}$$

The accidental distribution A_i is experimentally determined using the same selection criteria as our coincidence distribution, but with a time window of [-3.0, -2.701] ms preceding every prompt fission event (and thus cannot be correlated). It is important that the exposure time for the coincidence and accidental time windows are equal, since longer exposure times increase the multiplicity of that time window. This event selection provides the distribution A_i shown in Figure 5.3. We can see that the uncorrelated time window contains a significant fraction of events with non-zero nLi multiplicity, and thus the accidental pileup treatment is necessary. By using the distribution from Figure 5.3 as A_i and our coincidence distribution C_k from Figure 5.2 in Equation 5.1, we can solve for the elements of M_i as shown in Figure 5.4.

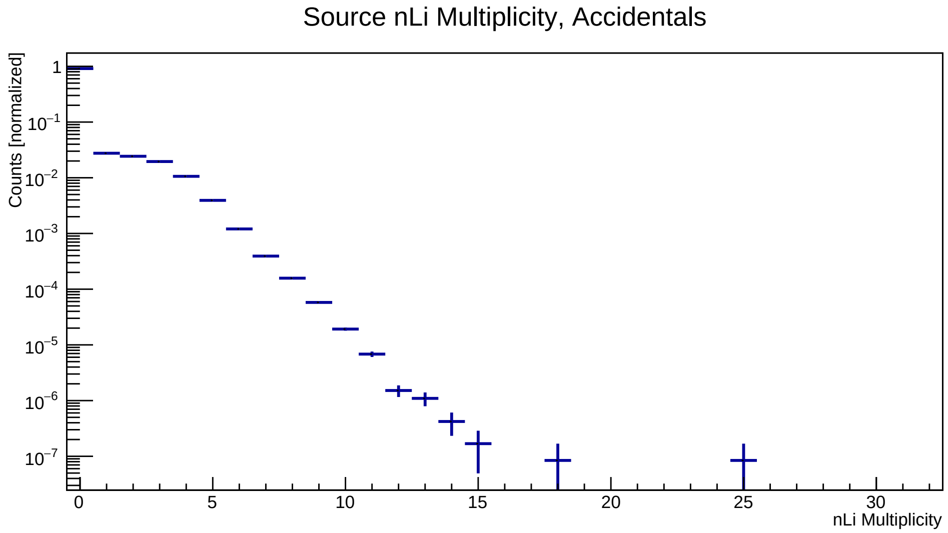

Figure 5.3: Accidental nLi multiplicity distribution, A_i from Equation 5.1, for a deployed ^{252}Cf source.

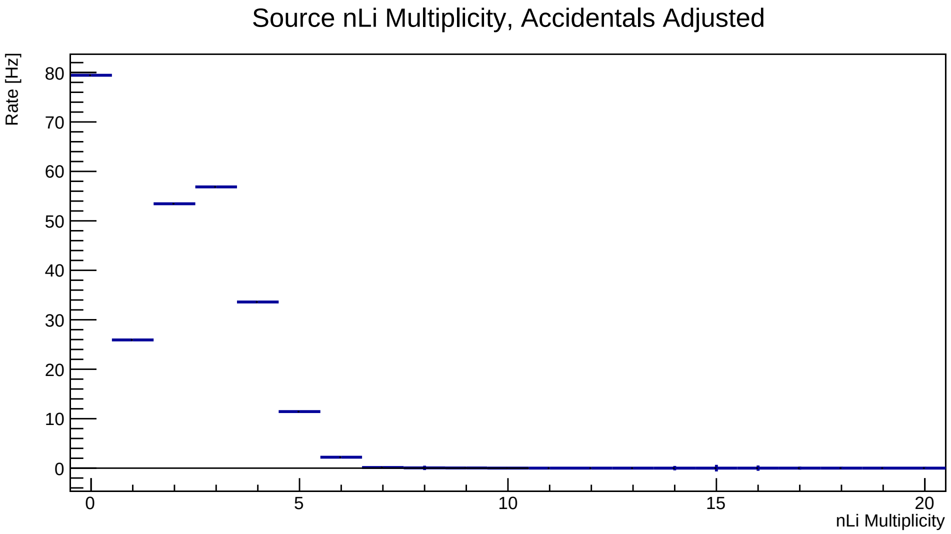

Figure 5.4: Neutron multiplicity distribution after applying the treatment from Equation 5.4 using the distribution from 5.3 for distribution A_i. nLi multiplicities past 8 are consistent with 0 in statistically propagated error. Y axis is converted to Rate for comparison with later plots.

5.3 False Triggers

We detect energy signals mimicking our prompt gamma ray event selection that are not from ^{252}Cf fission. Some of these are coming from the source itself while others are present in background data. These false prompt event triggers contribute to the excess rate of zero multiplicity events in our distributions in Figure 5.4. Here we separately address the false triggers that come from the source along with those unrelated to the source.

5.3.1 Beta Decays From Fission Fragments

When a ^{252}Cf nucleus undergoes spontaneous fission, there are typically two fission fragments along with the neutrons. These daughter particles will undergo beta decay on a time scale much longer than the average time between fissions given our source strength, and thus will appear as a uniform random background uncorrelated to fission events [97]. These beta decays contribute to the rate of signals with uncorrelated neutron captures rate in our multiplicity distribution.

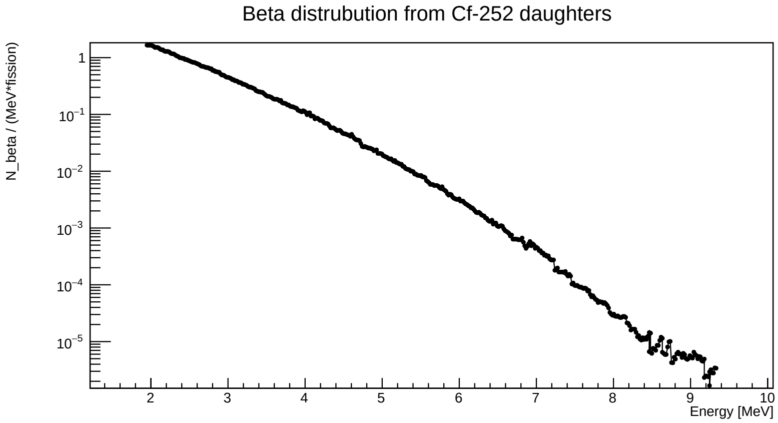

Figure 5.5: Beta energy distribution from fission fragments produced from ^{252}Cf spontaneous fission [98].

Not all beta decays from the fission fragments will escape the aluminum source capsule with enough energy above our prompt fission signal cut of 3.0 MeV. We need the beta energy spectrum from ^{252}Cf fission fragments, shown in Figure 5.5 taken from reference [98], along with information about the source capsule in order to calculate how many beta decays will show up in our detector.

We take the dominant aluminum source capsule width as 0.125 cm (from Figure 3.19), the density of aluminum as 2.7 g/cm^3, and the electron energy loss in aluminum from Figure 5.6 [99] to estimate that only beta particles with energies above 3.54 ± 0.09 MeV will escape the capsule above our prompt energy cut. The uncertainty in this energy primarily comes from our ~5% energy resolution.

Integrating Figure 5.5 for the energies of our fission trigger, we find 0.133 ± 0.018 beta particles per fission escaping the capsule in an energy region selected in this analysis as a fission trigger. The error in our energy resolution is propagated into the integral uncertainty. The 500 μs dead time following fissions times our fission rate of 252 ± 5 Hz, and including the 0.133 beta signals per fission, introduces an efficiency of 0.857 ± 0.003 for detecting these relatively long lived beta decays. Including an additional estimated 9% loss from the capsule geometry, we find a rate of 26.2 ± 4.0 detected beta particles per second escape from the source capsule above our energy cut. This rate is represented in Figure with other false trigger measurements in Figure 5.10.

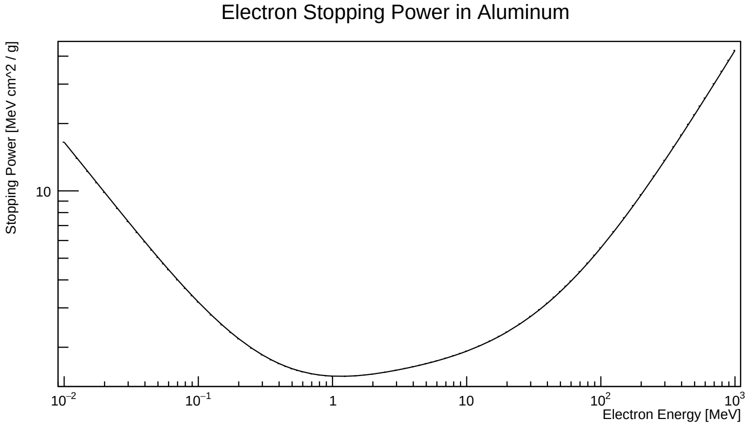

Figure 5.6: Electron energy loss in aluminum as a function of the electron energy [99].

5.3.2 Other Fission Induced Signals

While the E > 3.0 MeV energy cut on our prompt signal eliminates the false triggers on nH captures, here we consider the effect of other neutron interactions. After ^{6}Li and H, the next dominant target for neutron captures is ^{35}Cl. PG4 simulations and measurements estimate that the detected capture on ^{35}Cl is ∼2.7% of all neutron captures. In order to model how well our 500 μs veto eliminates these captures, we model the reduction by how much the nH peak is reduced by the veto. Without the veto, we detect ∼78 Hz of nH in our prompt triggers before the 3.0 MeV energy cut. This becomes ∼3.2 Hz (4.1% of 78 Hz) when introducing the 500 μs veto. This gives an effect of 0.11% from nCl, which is negligible compared to the various other effects. Other neutron capture targets in the scintillator have a much lower capture probability than ^{35}Cl, and will not affect the results of this study in a noticeable way.

5.3.3 Background events

We measure the background contribution to the multiplicity distribution by measuring data with the ^{252}Cf source retracted. Figures 5.7 and 5.8 show the coincidence and accidental nLi multiplicity distributions for a background data set. Using Equation 5.4 with these two distributions we find the accidentals treated nLi multiplicity distribution with the source removed, shown in Figure 5.9

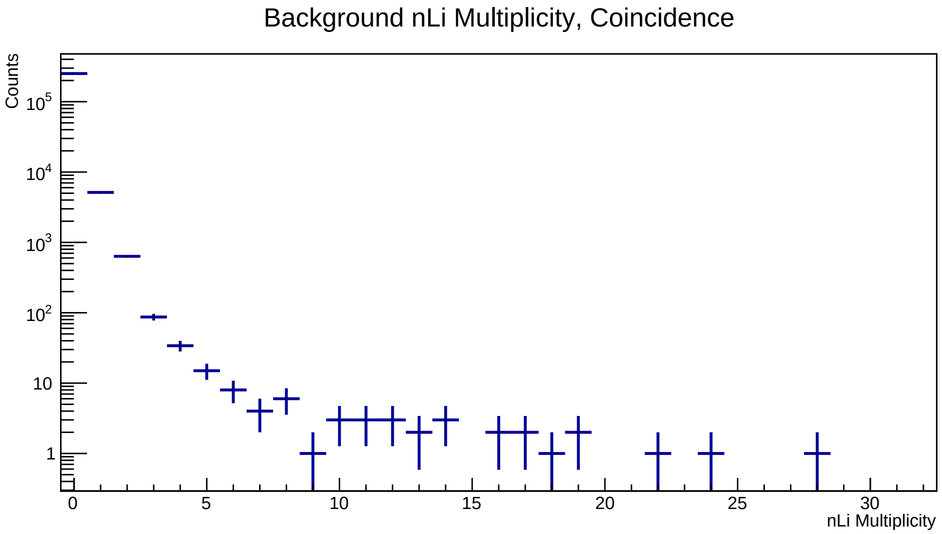

Figure 5.7: Coincidence nLi multiplicity distribution for ambient background data.

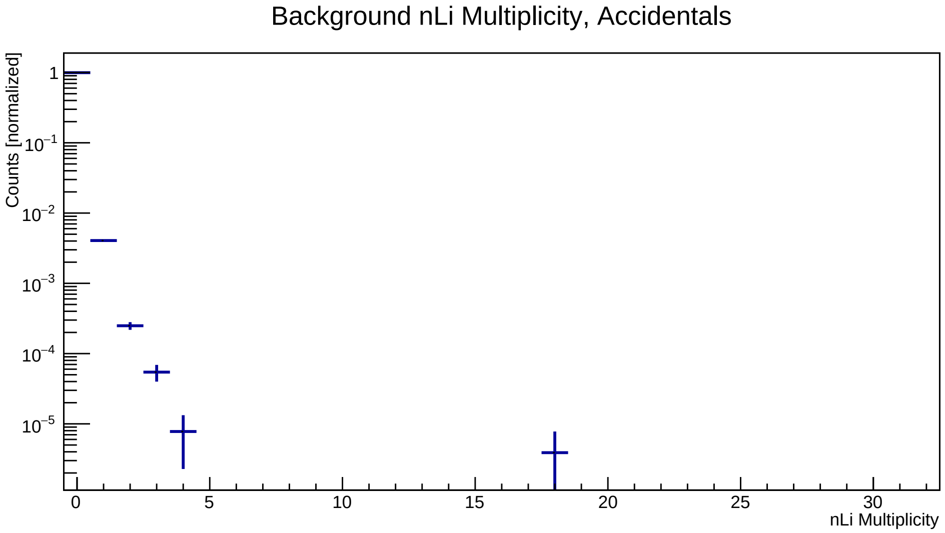

Figure 5.8: Accidental nLi multiplicity distribution for ambient background data.

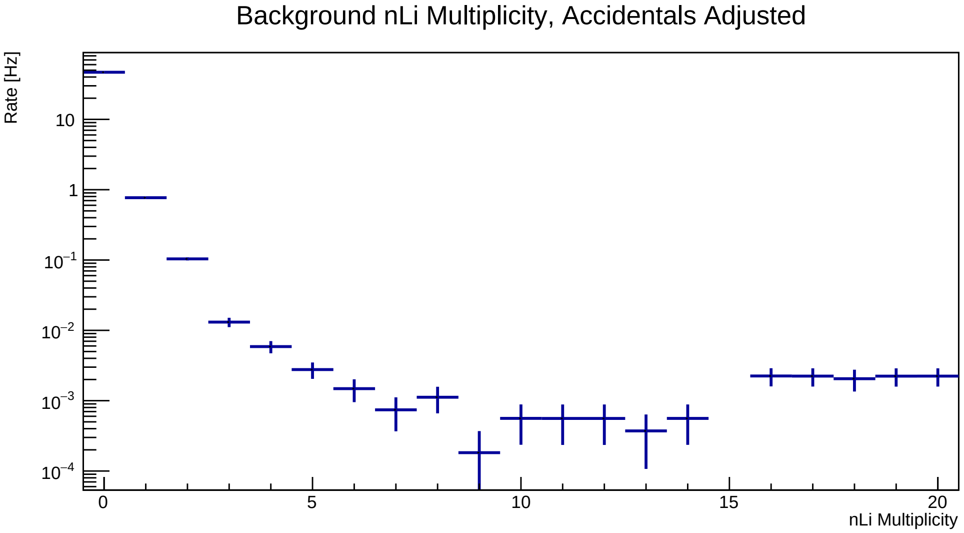

Figure 5.9: Background nLi multiplicity distribution after the accidentals pileup treatment in Equation 5.4 using the distributions in Figures 5.7 and 5.8, converted to a rate for comparison to the coincidence distribution.

Figure 5.10 shows the comparison between the accidentals treated source and background rate distribution, along with the rate from the previously calculated beta rate.

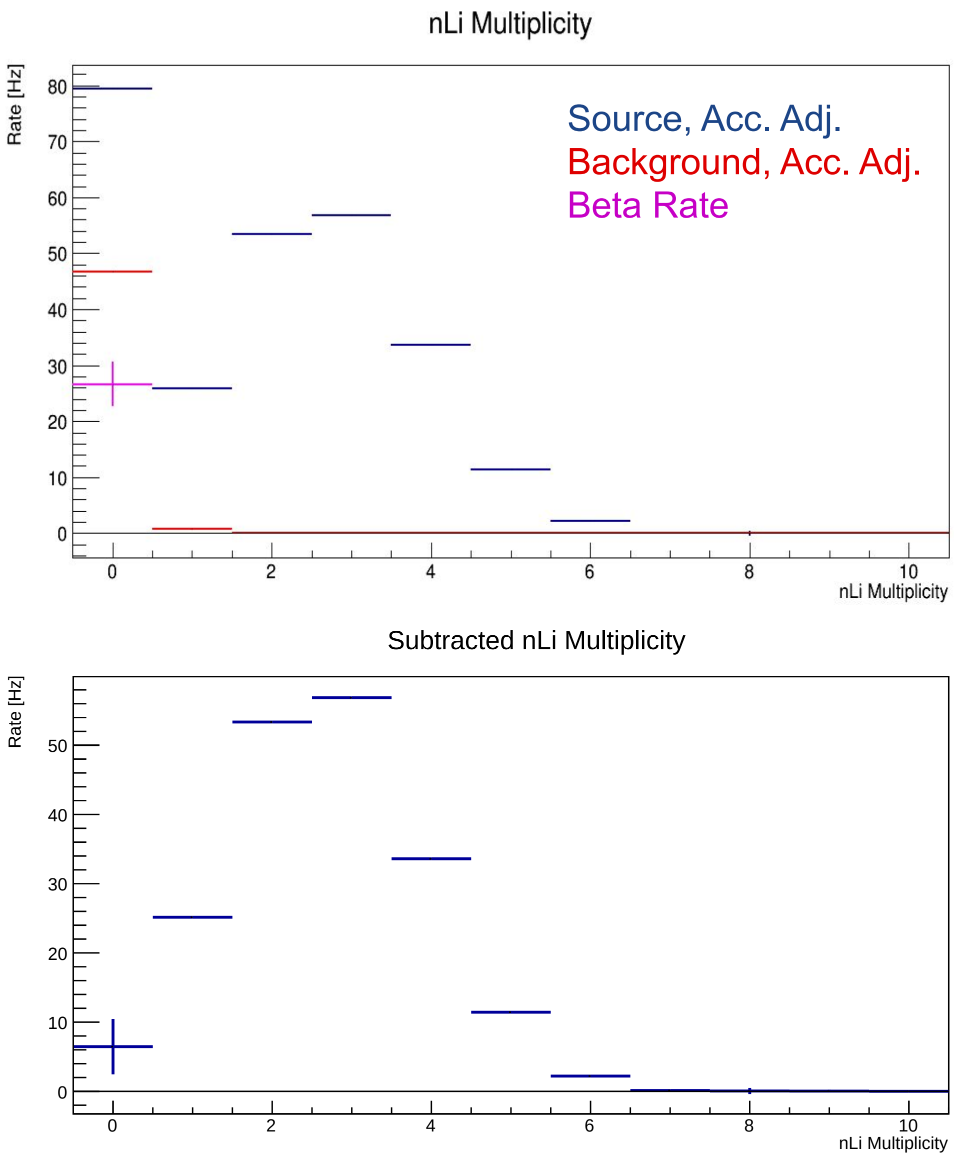

Figure 5.10: TOP: nLi multiplicity rate distribution comparing data from the source measurements, background measurements, and the calculated beta rate from the source. BOTTOM: The background and beta rates subtracted from the source rates, with errors added in quadrature.

5.4 Neutron Detection Efficiency Inversion

In order to reproduce the total neutron multiplicity, we need to account for undetected neutrons due to the finite nLi detection efficiency. The analysis here follows the formalism in Ref [100]. Let ϵ be the efficiency of detecting any given uncorrelated neutron in the detector, $P(p)$ be the probability that p neutrons are emitted in a given fission, and $Q(v)$ be the probability of detecting v neutrons from the same fission. The relationship between $Q(v)$ and $P(p)$ is

$$Q(v) = \sum_{p=v}^{\infty} C_v^p \epsilon^v (1-\epsilon)^{p-v} P(p), \tag{5.5}$$

where

$$C_v^p = \frac{p!}{v!\,(p-v)!} \tag{5.6}$$

are the binomial coefficients. The inverse of Equation 5.5 is

$$P(v) = \sum_{p=v}^{\infty} C_v^p \epsilon^{-v} (1-\epsilon^{-1})^{p-v} Q(p) \tag{5.7}$$

which means that if we know the neutron detection efficiency, this summation can be used to remake the original emitted neutron distribution [101, 100]. Our detector nLi efficiency is $0.727 \pm 0.014_{syst} \pm 0.008_{stat}$ at the ^{252}Cf source location, as determined in Section 4.4.3.1. The capture lifetime and time window lowers this efficiency further to 0.710 ± 0.016, where we combine the statistical and systematic uncertainties in quadrature. Applying this efficiency correction from Equation 5.7 to the distribution in the bottom panel of Figure 5.10 results in the distributions in Figure 5.11. The three shown distributions are for the calculated efficiency, as well as the upper and lower bound by uncertainty measurements. Although previous plots have truncated the x-axis, the values for multiplicities up to 20 were retained for this efficiency inversion. Since we are only interested in reporting multiplicities up to 10, the discrepancy of truncating the summation to 20 instead of infinity is negligible.

Since the efficiency inversion is a summation of terms, propagating the statistical error from Figure 5.10 is done by adding the weighted error from each contribution in quadrature. For multiplicities above 8, the propagated statistical error is inflated since each value with error was consistent with zero. In order to not artificially inflate the propagated statistical error for essentially 0 contributions to the inversion sum, errors from the multiplicities up to 10 in Figure 5.10 were used.

Exponential terms combined with the binomial coefficients for higher multiplicities p and v in Equation 5.7 cause large oscillatory behavior for high multiplicities with low statistics and high error [102, 103]. Small changes in the efficiency will cause very large changes in the inversion results for these events. This oscillatory behavior shows up in the high multiplicity bins (multiplicity > 10) where the rate was consistent with 0 before the efficiency treatment. For the multiplicities we report at the end of the study, the effect of error from the nLi efficiency is determined by the difference between the distributions shown in Figure 5.11.

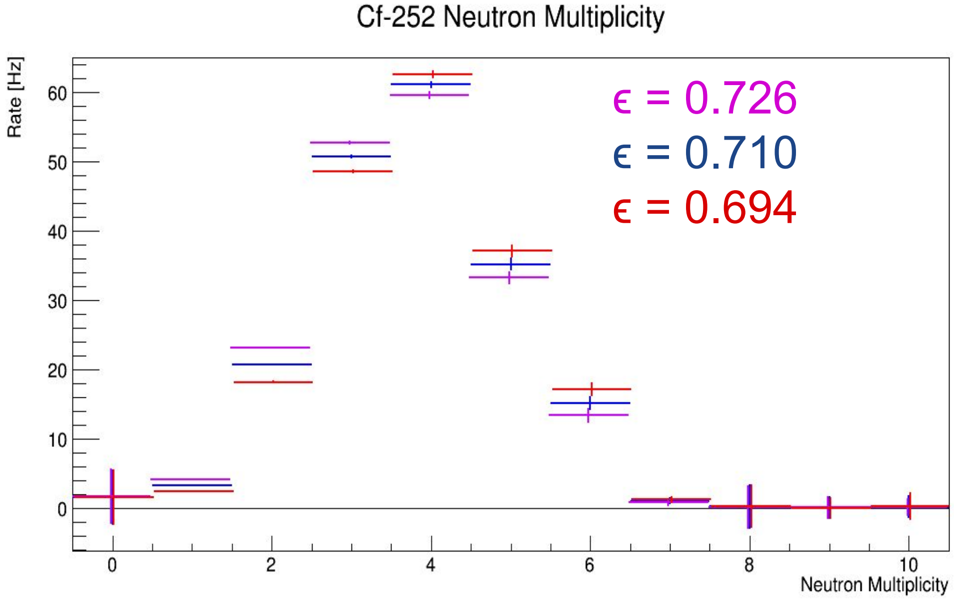

Figure 5.11: Resulting multiplicity distributions after efficiency correction in Equation 5.7. The multiple distributions cover the range of uncertainty in our efficiency. Error bars are statistical and propagated from Figure 5.10. Multiplicities above 10 are shown to exhibit the oscillatory behavior from the inversion described in text. Statistical error bars for these higher multiplicities are ignored since they are not reported later, and extend outside the range of the y-axis.

5.5 Simulation Cross Checks

The methods and treatments described in this chapter were tested with high statistics toy simulations on exactly known input distributions. These simulations were used to check statistical errors were propagated properly by repeating the accidentals algorithm and efficiency inversion with a random Gaussian error smearing, and measuring the difference in the resulting values. One of the important uses of this toy simulation was to gauge the validity of our accidentals distribution from the source.

5.5.1 Accidentals Distribution Cross Check

In order to make sure we understand the source accidentals distribution, we simulated events with fission gammas uniformly distributed in time with the source strength, followed by neutrons with multiplicity taken from Santi & Miller [93] according to our capture lifetime and accounting for our nLi detection efficiency. In addition, a random 17 Hz uncorrelated neutron rate is added based on measurements on background data. Figure 5.12 shows the accidentals distribution from this toy simulation compared to the measured distribution shown in Figure 5.3. A systematic error band is applied by repeating the simulation with a Gaussian error smearing correlated to the uncertainty in the nLi efficiency and the neutron capture lifetime. The agreement seen in Figure 5.12 demonstrates that our simple model sufficiently captures the important dynamics of the source for this study.

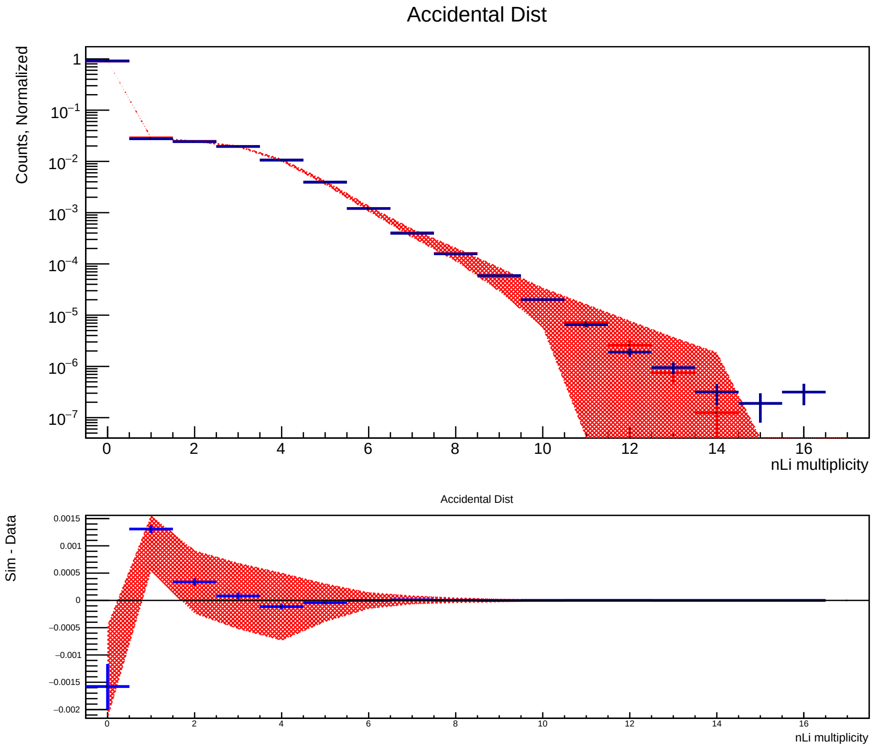

Figure 5.12: Toy simulation (red) and data (blue) for the accidentals multiplicity distribution from a ^{252}Cf source (top), with the plotted difference between the distributions (bottom). The red band signifies systematic error from the neutron capture lifetime and efficiency.

Additionally, our 500 μs dead time between prompt triggers introduces a bias in our coincidence distribution that is not equally represented in the accidentals distribution. Using the toy simulation to predict the size of this effect at our source rate, we see a ∼0.1% deviation introduced for each final multiplicity probability. This is negligible compared to the propagated statistical error and the error from the efficiency inversion, and is not included in final result.

5.6 Final Multiplicity Distribution

By normalizing the distribution by the integral rates of each multiplicity, we can find the probability multiplicity distribution. Statistical uncertainty is combined in quadrature with uncertainties from efficiency and unfolding. By normalizing the distribution by the integral of each multiplicity, we find the probability multiplicity distribution. Figure 5.13 shows this distribution with a comparison to the evaluation of Holden and Zucker in 1984, and Santi and Miller in 2008, with the values and errors displayed in Table 5.1 [92, 93].

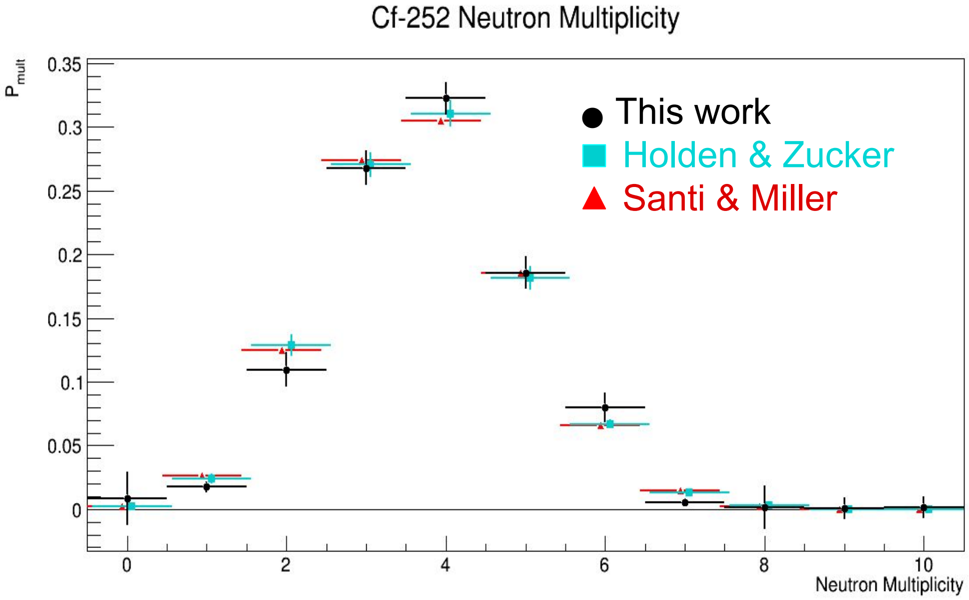

Figure 5.13: Neutron multiplicity probability distribution from the spontaneous fission of ^{252}Cf from this work (black circles) compared to the distributions from Holden & Zucker [92] (teal squares) and Santi & Miller [93] (red triangles).

	Present Work	Holden & Zucker	Santi & Miller
P_0	0.009 ± 0.021	0.0023 ± 0.00121	0.0021767 ± 0.00012
P_1	0.0173 ± 0.0046	0.024 ± 0.004	0.0259869 ± 0.00123
P_2	0.109 ± 0.014	0.129 ± 0.008	0.1251188 ± 0.00132
P_3	0.268 ± 0.014	0.271 ± 0.001	0.2740459 ± 0.00119
P_4	0.322 ± 0.013	0.310 ± 0.011	0.3050812 ± 0.00144
P_5	0.186 ± 0.013	0.181 ± 0.009	0.1854741 ± 0.00119
P_6	0.080 ± 0.012	0.067 ± 0.004	0.0658998 ± 0.00065
P_7	0.006 ± 0.003	0.013 ± 0.003	0.0142918 ± 0.00096
P_8	0.0014 ± 0.018	0.0027 ± 0.0013	0.0018219 ± 0.0003
P_9	0.0004 ± 0.009	0.00004 ± 0.00007	0.0001022 ± 0.00017
P_{10}	0.0012 ± 0.009	0.00000043 ± 0.00000142	0.0000005 ± 0.0000016
$< v >$	3.805 ± 0.053	3.797 ± 0.020	3.757 ± 0.010

Table 5.1: Neutron multiplicity probability distribution of ^{252}Cf spontaneous fission from this work, compared to the values from Holden & Zucker [92] and Santi & Miller [93].

This present work shows that we agree with the two publication summaries within $\sim$1-2σ both bin by bin for most multiplicites, and overall. Multiplicities past 7 in our work have relatively large errors arising from propagated statistical error and suffer from having severely reduced event representation due to the accidental distribution. The error from the published distributions are compilations of previous studies and their error comes from the standard error of the measurements included in each compilation, and may be an underestimation of total error.

The estimation of the uncertainty in many older original measurements combined in refs [93, 92] is problematic. Small uncertainties corresponding to the precision of their measurements are quoted, but do not include systematic errors. In addition, assumptions of detector efficiencies rely on forcing multiplicity distribution means to exactly 3.757, reducing error introduced during the efficiency inversion as shown in this study [92]. As described in Section 4.4.3.1, calculating the single neutron detection efficiency in our detector did rely on knowledge of the neutron source rate, which was calculated from the manufacturer source strength as well as an assumed neutron multiplicity, this efficiency was measured relatively independent of the neutron coincidence counting, and error from the source strength dominated uncertainties in the efficiency error.

This study shows that although the PROSPECT detector was built for other purposes, the calibration system design made a reasonable calculation of the neutron multiplicity from ^{252}Cf spontaneous fission possible. The treatments outlined in this chapter are applicable to most well characterized scintillator based detectors. Since other neutrino detectors use ^{252}Cf as a neutron source for calibrations, this opens up the possibility of these experiments similarly adding to the existing library of multiplicity measurements. Although the large systematic uncertainties associated with this measurement largely remove its publication merit, a modest increase in the ^{6}Li doping would increase the efficiency and lower the neutron capture lifetime. This would allow one to use a shorter coincidence and accidental window, and combined with a lower rate source, would greatly reduce the accidental correction uncertainty, possibly providing a new independent measurement of the ^{252}Cf spontaneous fission neutron multiplicity.

CHAPTER 6

CONCLUSIONS

Current results from reactor neutrino experiments pose interesting quandaries for the nuclear-particle physics community. The PROSPECT experiment used a segmented detector to either rule out or measure short baseline neutrino oscillation independent of reactor flux calculations, and measure the ^{235}U antineutrino energy spectrum from HFIR. The PROSPECT collaboration published results with over 30,000 reactor correlated neutrino events. Analysis is ongoing with more data ($\sim$50,000 events) than is already published, with new publications forthcoming. The detector has already been decommissioned and is back in storage with ongoing studies for a potential upgrade in the following years.

IBD measurements with the PROSPECT detector are dependent on understanding the neutron detection. Calibrations were used to benchmark aspects of the neutron response in MC simulations. By comparing PG4 simulations with neutron calibration data from the ^{252}Cf source and cosmogenic neutrons, the detector ^{6}Li doping fraction in the scintillator was found to be decreasing in the detector volume. Current studies on the LiLS after detector decommissioning are underway to shed more light on this. While this scintillator degradation is concerning, the effects did not introduce error beyond the assigned systematic or statistical uncertainties in PROSPECT published results.

We took advantage of the high volume and neutron detection efficiency to make a new measurement of the neutron multiplicity distribution from ^{252}Cf spontaneous fission that was in agreement with previously published studies and re-evaluation publications. In order to improve on this study, a lower source strength to reduce the accidental pile-up rate, and higher neutron detection efficiency would be required.

In addition to the work described in chapters 4 and 5, my contribution to the PROSPECT collaboration included cleaning and assembling individual detector components during the Summer and Fall of 2017. During the detector commissioning, I assisted on-site at HFIR to assist and monitor the detector filling procedures. During data-taking, I organized multiple week long radioactive source calibration campaigns at HFIR. This encompassed creating schedules for source deployments, assisting in switching sources in the calibration hardware system, and leading the on-site team.

BIBLIOGRAPHY

[1] J. Chadwick. The Intensity Distribution in the Magnetic Spectrum of Beta Particles from Radium (B + C). *Verh. Phys. Gesell.*, 16:383–391, 1914.

[2] Laurie M Brown. The Idea of the Neutrino. *Physics Today*, 31(9):23, 1978.

[3] E. Fermi. An Attempt of a Theory of Beta Radiation. 1. *Z. Phys.*, 88:161–177, 1934.

[4] Frederick Reines, Clyde L Cowan Jr, FB Harrison, AD McGuire, and HW Kruse. Detection of the Free Antineutrino. *Physical Review*, 117(1):159, 1960.

[5] Frederick Reines and Clyde L Cowan Jr. Free Antineutrino Absorption Cross Section. I. Measurement of the Free Antineutrino Absorption Cross Section by Protons. *Physical Review*, 113(1):273, 1959.

[6] Clyde L Cowan Jr, Frederick Reines, FB Harrison, HW Kruse, and AD McGuire. Detection of the Free Neutrino: a Confirmation. In *Neutrinos And Other Matters: Selected Works of Frederick Reines*, pages 57–58. World Scientific, 1991.

[7] Gaillard Danby, JM Gaillard, Konstantin Goulianos, LM Lederman, N Mistry, M Schwartz, and J Steinberger. Observation of High-energy Neutrino Reactions and the Existence of Two Kinds of Neutrinos. *Physical Review Letters*, 9(1):36, 1962.

[8] K Kodama, N Ushida, C Andreopoulos, N Saoulidou, G Tzanakos, P Yager, B Baller, D Boehnlein, Walter Freeman, B Lundberg, et al. Observation of Tau Neutrino Interactions. *Physics Letters B*, 504(3):218–224, 2001.

[9] ALEPH Collaboration, DELPHI Collaboration, L3 Collaboration, OPAL Collaboration, and SLD Collaboration. The SLD Electroweak and Heavy Flavour Groups, Precision electroweak measurements on the Z resonance. phys. rept. 427, 257 (2006).

[10] Georgios Voutsinas, Emmanuel Perez, Mogens Dam, and Patrick Janot. Beam-beam Effects on the Luminosity Measurement at LEP and the Number of Light Neutrino Species. *Physics Letters B*, 800:135068, 2020.

[11] F Capozzi, E Lisi, A Marrone, D Montanino, and A Palazzo. Neutrino Masses and Mixings: Status of Known and Unknown 3ν Parameters. *Nuclear Physics B*, 908:218–234, 2016.

[12] M. Tanabashi et al. Review of Particle Physics. *Phys. Rev. D*, 98:030001, Aug 2018.

[13] Samoil M Bilenky, Donato Nicolo, and ST Petcov. Constraints from a Three-Neutrino Oscillation Analysis of the CHOOZ Data. *Physics Letters B*, 538(1-2):77–86, 2002.

[14] Masaki Ishitsuka, Takaaki Kajita, Hisakazu Minakata, and Hiroshi Nunokawa. Resolving the Neutrino Mass Hierarchy and CP Degeneracy by Two Identical Detectors with Different Baselines. *Physical Review D*, 72(3):033003, 2005.

[15] Aldo Serenelli. Alive and Well: a Short Review About Standard Solar Models. *The European Physical Journal A*, 52(4):78, 2016.

[16] JN Abdurashitov, EL Faizov, VN Gavrin, AO Gusev, AV Kalikhov, TV Knodel, II Knyshenko, VN Kornoukhov, IN Mirmov, AM Pshukov, et al. Results from SAGE (The Russian-American Gallium Solar Neutrino Experiment). *Physics Letters B*, 328(1-2):234–248, 1994.

[17] Wolfgang Hampel, J Handt, G Heusser, J Kiko, T Kirsten, M Laubenstein, E Pernicka, W Rau, M Wojcik, Yu Zakharov, et al. GALLEX Solar Neutrino Observations: Results for GALLEX IV. *Physics Letters B*, 447(1-2):127–133, 1999.

[18] M Altmann, M Balata, P Belli, E Bellotti, R Bernabei, E Burkert, C Cattadori, Giorgio Cerichelli, Marco Chiarini, M Cribier, et al. GNO Solar Neutrino Observations: Results for GNO I. *Physics Letters B*, 490(1-2):16–26, 2000.

[19] Herbert H Chen. Direct Approach to Resolve the Solar-Neutrino Problem. *Physical Review Letters*, 55(14):1534, 1985.

[20] Karsten M Heeger and RGH Robertson. Probability of a Solution to the Solar Neutrino Problem Within the Minimal Standard Model. *Physical review letters*, 77(18):3720, 1996.

[21] Bruno Pontecorvo. Neutrino Experiments and the Problem of Conservation of Leptonic Charge. *Sov. Phys. JETP*, 26(984-988):165, 1968.

[22] Samoil M Bilenky and B Pontecorvo. Lepton Mixing and Neutrino Oscillations. *Physics Reports*, 41(4):225–261, 1978.

[23] Y Fukuda, T Hayakawa, E Ichihara, K Inoue, K Ishihara, Hirokazu Ishino, Y Itow, T Kajita, J Kameda, S Kasuga, et al. Evidence for Oscillation of Atmospheric Neutrinos. *Physical Review Letters*, 81(8):1562, 1998.

[24] Q Retal Ahmad, RC Allen, TC Andersen, JD Anglin, G Bühler, JC Barton, EW Beier, M Bercovitch, J Bigu, S Biller, et al. Measurement of the Rate of $\nu_e + d \rightarrow p + p + e^-$ Interactions Produced by B 8 Solar Neutrinos at the Sudbury Neutrino Observatory. *Physical Review Letters*, 87(7):071301, 2001.

[25] T Araki, K Eguchi, S Enomoto, K Furuno, K Ichimura, H Ikeda, K Inoue, K Ishihara, T Iwamoto, T Kawashima, et al. Measurement of Neutrino Oscillation with KamLAND: Evidence of Spectral Distortion. *Physical Review Letters*, 94(8):081801, 2005.

[26] A Yu Smirnov. Solar Neutrinos: Oscillations or No-oscillations? *arXiv preprint arXiv:1609.02386*, 2016.

[27] Y Suzuki. Solar Neutrino Results from Super-Kamiokande. *Nuclear Physics B-Proceedings Supplements*, 77(1-3):35–42, 1999.

[28] A Yu Smirnov. The MSW Effect and Matter Effects in Neutrino Oscillations. *Physica Scripta*, 2005(T121):57, 2005.

[29] Takaaki Kajita. Discovery of atmospheric neutrino oscillations. *Nippon Butsuri Gakkai-Shi*, 58(5):326–331, 2003.

[30] X Qian and P Vogel. Neutrino Mass Hierarchy. *Progress in Particle and Nuclear Physics*, 83:1–30, 2015.

[31] A. C. Hayes and Petr Vogel. Reactor Neutrino Spectra. *Ann. Rev. Nucl. Part. Sci.*, 66:219–244, 2016.

[32] Feng Peng An, AB Balantekin, HR Band, M Bishai, S Blyth, I Butorov, D Cao, GF Cao, J Cao, WR Cen, et al. Measurement of the Reactor Antineutrino Flux and Spectrum at Daya Bay. *Physical review letters*, 116(6):061801, 2016.

[33] Y Abe, Christoph Aberle, JC Dos Anjos, JC Barriere, M Bergevin, A Bernstein, TJC Bezerra, L Bezrukhov, E Blucher, NS Bowden, et al. Reactor ν_e Disappearance in the Double Chooz Experiment. *Physical Review D*, 86(5):052008, 2012.

[34] J Ashenfelter, AB Balantekin, HR Band, G Barclay, CD Bass, D Berish, L Bignell, NS Bowden, A Bowes, JP Brodsky, et al. The PROSPECT Physics Program. *Journal of Physics G: Nuclear and Particle Physics*, 43(11):113001, 2016.

[35] AC Hayes, JL Friar, GT Garvey, Gerard Jungman, and Guy Jonkmans. Systematic Uncertainties in the Analysis of the Reactor Neutrino Anomaly. *Physical Review Letters*, 112(20):202501, 2014.

[36] DA Dwyer and TJ Langford. Spectral Structure of Electron Antineutrinos from Nuclear Reactors. *Physical review letters*, 114(1):012502, 2015.

[37] AA Sonzogni, EA McCutchan, TD Johnson, and P Dimitriou. Effects of Fission Yield Data in the Calculation of Antineutrino Spectra for U 235 (n, fission) at Thermal and Fast Neutron Energies. *Physical review letters*, 116(13):132502, 2016.

[38] Alejandro A Sonzogni, M Nino, and EA McCutchan. Revealing Fine Structure in the Antineutrino Spectra from a Nuclear Reactor. *Physical Review C*, 98(1):014323, 2018.

[39] Xin Qian and Jen-Chieh Peng. Physics with Reactor Neutrinos. *Rept. Prog. Phys.*, 82(3):036201, 2019.

[40] F. Von Feilitzsch, A. A. Hahn, and K. Schreckenbach. Experimental Beta Spectra From PU-239 and U-235 Thermal Neutron Fission Products and their Correlated Anti-neutrino Spectra. *Phys. Lett.*, 118B:162–166, 1982.

[41] K. Schreckenbach, G. Colvin, W. Gelletly, and F. Von Feilitzsch. Determination of the Anti-neutrino Spectrum from U-235 Thermal Neutron Fission Products up to 9.5-MeV. *Phys. Lett.*, 160B:325–330, 1985.

[42] A. A. Hahn, K. Schreckenbach, G. Colvin, B. Krusche, W. Gelletly, and F. Von Feilitzsch. Anti-neutrino Spectra From ^{241}Pu and ^{239}Pu Thermal Neutron Fission Products. *Phys. Lett.*, B218:365–368, 1989.

[43] P. Vogel, G. K. Schenter, F. M. Mann, and R. E. Schenter. Reactor Antineutrino Spectra and their Application to Antineutrino-induced Reactions. II. *Phys. Rev. C*, 24:1543–1553, Oct 1981.

[44] Th A Mueller, D Lhuillier, M Fallot, A Letourneau, S Cormon, M Fechner, L Giot, Th Lasserre, J Martino, G Mention, et al. Improved Predictions of Reactor Antineutrino Spectra. *Physical Review C*, 83(5):054615, 2011.

[45] Patrick Huber. Determination of Antineutrino Spectra from Nuclear Reactors. *Physical Review C*, 84(2):024617, 2011.

[46] P Vogel and JF Beacom. Angular Distribution of Neutron Inverse Beta Decay. *Phys. Rev. D*, 60:053003–1, 1999.

[47] Glenn R Jocher, Daniel A Bondy, Brian M Dobbs, Stephen T Dye, James A Georges III, John G Learned, Christopher L Mulliss, and Shawn Usman. Theoretical Antineutrino Detection, Direction and Ranging at Long Distances. *Physics Reports*, 527(3):131–204, 2013.

[48] SH Seo, WQ Choi, H Seo, JH Choi, Y Choi, HI Jang, JS Jang, KK Joo, BR Kim, HS Kim, et al. Spectral Measurement of the Electron Antineutrino Oscillation Amplitude and Frequency Using 500 Live Days of RENO Data. *Physical Review D*, 98(1):012002, 2018.

[49] H. De Kerret et al. First Double Chooz θ_{13} Measurement via Total Neutron Capture Detection. 2019. arXiv:1901.09445 [hep-ex].

[50] Y Abe, JC Dos Anjos, JC Barriere, E Baussan, I Bekman, M Bergevin, TJC Bezerra, L Bezrukov, E Blucher, C Buck, et al. Improved Measurements of the Neutrino Mixing Angle θ_{13} with the Double Chooz Detector. *Journal of High Energy Physics*, 2014(10):86, 2014.

[51] Henry Band, Alfredo Galindo-Uribarri, and Hans P Mumm. The PROSPECT Physics Program. Technical report, Oak Ridge National Laboratory (ORNL), Oak Ridge, TN (United States), 2016.

[52] K Schreckenbach, HR Faust, F Von Feilitzsch, AA Hahn, K Hawerkamp, and JL Vuilleumier. Absolute Measurement of the Beta Spectrum from ^{235}U Fission as a Basis for Reactor Antineutrino Experiments. *Physics Letters B*, 99(3):251–256, 1981.

[53] F Von Feilitzsch, AA Hahn, and K Schreckenbach. Experimental Beta-spectra from ^{239}Pu and ^{235}U Thermal Neutron Fission Products and their Correlated Antineutrino Spectra. *Physics Letters B*, 118(1-3):162–166, 1982.

[54] K Schreckenbach, G Colvin, W Gelletly, and F Von Feilitzsch. Determination of the Antineutrino Spectrum from ^{235}U Thermal Neutron Fission Products up to 9.5 MeV. *Physics Letters B*, 160(4-5):325–330, 1985.

[55] Antineutrino Spectra from ^{241}Pu and ^{239}Pu Thermal Neutron Fission Products, author=Hahn, AA and Schreckenbach, K and Gelletly, W and Von Feilitzsch, F and Colvin, G and Krusche, B, journal=Physics Letters B, volume=218, number=3, pages=365–368, year=1989, publisher=Elsevier.

[56] N Haag, W Gelletly, F von Feilitzsch, L Oberauer, W Potzel, K Schreckenbach, and AA Sonzogni. Re-publication of the Data from the BILL Magnetic Spectrometer: The Cumulative β Spectra of the Sission Products of ^{235}U, ^{239}Pu, and ^{241}Pu. *arXiv preprint arXiv:1405.3501*, 2014.

[57] AC Hayes, JL Friar, GT Garvey, Duligur Ibeling, Gerard Jungman, T Kawano, and Robert W Mills. Possible Origins and Implications of the Shoulder in Reactor Neutrino Spectra. *Physical Review D*, 92(3):033015, 2015.

[58] Nils Haag, Achim Guetlein, Martin Hofmann, L Oberauer, W Potzel, K Schreckenbach, and FM Wagner. Experimental Determination of the Antineutrino Spectrum of the Fission Products of ^{238}U. *Physical review letters*, 112(12):122501, 2014.

[59] J Ashenfelter, AB Balantekin, C Baldenegro, HR Band, CD Bass, DE Bergeron, D Berish, LJ Bignell, NS Bowden, J Boyle, et al. The PROSPECT Reactor Antineutrino Experiment. *Nuclear Instruments and Methods in Physics Research Section A: Accelerators, Spectrometers, Detectors and Associated Equipment*, 922:287–309, 2019.

[60] FP An, AB Balantekin, HR Band, M Bishai, S Blyth, D Cao, GF Cao, J Cao, YL Chan, JF Chang, et al. Evolution of the Reactor Antineutrino Flux and Spectrum at Daya Bay. *Physical Review Letters*, 118(25):251801, 2017.

[61] D Adey, FP An, AB Balantekin, HR Band, M Bishai, S Blyth, D Cao, GF Cao, J Cao, YL Chan, et al. Improved Measurement of the Reactor Antineutrino Flux at Daya Bay. *Physical Review D*, 100(5):052004, 2019.

[62] Mona Dentler, Álvaro Hernández-Cabezudo, Joachim Kopp, Pedro Machado, Michele Maltoni, Ivan Martinez-Soler, and Thomas Schwetz. Updated Global Analysis of Neutrino Oscillations in the Presence of eV-Scale Sterile Neutrinos. *Journal of High Energy Physics*, 2018(8):10, 2018.

[63] A Aguilar, LB Auerbach, RL Burman, DO Caldwell, ED Church, AK Cochran, JB Donahue, A Fazely, GT Garvey, RM Gunasingha, et al. Evidence for Neutrino Oscillations from the Observation of Electron Anti-neutrinos in a Muon Anti-neutrino Beam. *arXiv preprint hep-ex/0104049*, 2001.

[64] C Giunti, M Laveder, YF Li, and HW Long. Pragmatic View of Short-Baseline Neutrino Oscillations. *Physical Review D*, 88(7):073008, 2013.

[65] Carlo Giunti and Marco Laveder. Statistical Significance of the Gallium Anomaly. *Phys. Rev.*, C83:065504, 2011.

[66] G Mention, M Fechner, Th Lasserre, Th A Mueller, D Lhuillier, M Cribier, and A Letourneau. Reactor Antineutrino Anomaly. *Physical Review D*, 83(7):073006, 2011.

[67] https://neutrons.ornl.gov/hfir.

[68] PROSPECT Collaboration, J Ashenfelter, AB Balantekin, C Baldenegro, HR Band, CD Bass, DE Bergeron, D Berish, LJ Bignell, NS Bowden, et al. First Search for Short-Baseline Neutrino Oscillations at HFIR with PROSPECT. *Physical review letters*, 121(25):251802, 2018.

[69] PROSPECT Collaboration, J Ashenfelter, AB Balantekin, HR Band, CD Bass, DE Bergeron, D Berish, NS Bowden, JP Brodsky, CD Bryan, et al. Measurement of the Antineutrino Spectrum from U 235 Fission at HFIR with PROSPECT. *Physical Review Letters*, 122(25):251801, 2019.

[70] Germina Ilas, David Chandler, Brian J Ade, Eva E Sunny, Benjamin R Betzler, and Daniel Pinkston. Modeling and Simulations for the High Flux Isotope Reactor Cycle 400. Technical report, Oak Ridge National Lab.(ORNL), Oak Ridge, TN (United States). High Flux , 2015.

[71] J Ashenfelter, B Balantekin, CX Baldenegro, HR Band, G Barclay, CD Bass, D Berish, NS Bowden, CD Bryan, JJ Cherwinka, et al. Background Radiation Measurements at High Power Research Reactors. *Nuclear Instruments and Methods in Physics Research Section A: Accelerators, Spectrometers, Detectors and Associated Equipment*, 806:401–419, 2016.

[72] Brennan Hackett. DANG and the Background Characterisation of HFIR for PROSPECT. https://prospect.yale.edu/sites/default/files/hackett_brennan_-_university_of_surrey.pdf.

[73] Blaine Alexander Heffron. Characterization of Reactor Background Radiation at HFIR for the PROSPECT Experiment. https://trace.tennessee.edu/utk_gradthes/4747/.

[74] J Ashenfelter, AB Balantekin, HR Band, CD Bass, DE Bergeron, D Berish, LJ Bignell, NS Bowden, JP Brodsky, CD Bryan, et al. Lithium-Loaded Liquid Scintillator Production for the PROSPECT Experiment. *Journal of Instrumentation*, 14(03):P03026, 2019.

[75] J Ashenfelter, AB Balantekin, HR Band, CD Bass, DE Bergeron, D Berish, NS Bowden, JP Brodsky, CD Bryan, JJ Cherwinka, et al. A Low Mass Optical

Grid for the PROSPECT Reactor Antineutrino Detector. *Journal of Instrumentation*, 14(04):P04014, 2019.

[76] Glenn F Knoll. *Radiation Detection and Measurement.* John Wiley & Sons, 2010.

[77] J Ashenfelter, AB Balantekin, HR Band, CD Bass, DE Bergeron, D Berish, NS Bowden, JP Brodsky, CD Bryan, A Bykadorova Telles, et al. Performance of a Segmented 6Li-Loaded Liquid Scintillator Detector for the PROSPECT Experiment . *Journal of Instrumentation*, 13(06):P06023, 2018.

[78] M. Mendenhall. AD1 Calibrations tech note. PROSPECT DocDB 2314-v2, May 2018.

[79] M. Mendenhall. PRD Figure 7: PSD vs Signal. PROSPECT DocDB 2731-v1, May 2019.

[80] Daniel E. Landschoot. Short-Wavelength Reactor Neutrino Oscillations. PhD Thesis, Temple University, Dec 2019.

[81] J Ashenfelter, AB Balantekin, HR Band, CD Bass, DE Bergeron, D Berish, NS Bowden, JP Brodsky, CD Bryan, JJ Cherwinka, et al. The Radioactive Source Calibration System of the PROSPECT Reactor Antineutrino Detector. *Nuclear Instruments and Methods in Physics Research Section A: Accelerators, Spectrometers, Detectors and Associated Equipment*, 944:162465, 2019.

[82] Sea Agostinelli, John Allison, K al Amako, J Apostolakis, H Araujo, P Arce, M Asai, D Axen, S Banerjee, G Barrand, et al. GEANT4a Simulation Toolkit. *Nuclear instruments and methods in physics research section A: Accelerators, Spectrometers, Detectors and Associated Equipment*, 506(3):250–303, 2003.

[83] J.B. BIRKS. Chapter 8 - organic liquid scintillators. In J.B. BIRKS, editor, *The Theory and Practice of Scintillation Counting*, International Series of Monographs in Electronics and Instrumentation, pages 269 – 320. Pergamon, 1964.

[84] Xianyi Zhang. Energy Scale Study for PROSPECT's Measurement of the Antineutrino SPectrum of ^{235}U. PhD Thesis, Illinois Institute of Technology, December 2019.

[85] Joseph A Formaggio and CJ Martoff. Backgrounds to Sensitive Experiments Underground. *Annu. Rev. Nucl. Part. Sci.*, 54:361–412, 2004.

[86] Timothy E Valentine. Evaluation of Prompt Fission Gamma Rays for Use in Simulating Nuclear Safeguard Measurements. *Annals of Nuclear Energy*, 28(3):191–201, 2001.

[87] RC Martin, JB Knauer, and PA Balo. Production, Distribution and Applications of Californium-252 Neutron Sources. *Applied Radiation and Isotopes*, 53(4):785–792, 2000.

[88] Sigma Periodic Table Browse. `https://www.nndc.bnl.gov/sigma/`. Accessed: 2019-07-14.

[89] NS Bowden, M Sweany, and S Dazeley. A Note on Neutron Capture Correlation Signals, Backgrounds, and Efficiencies. *Nuclear Instruments and Methods in Physics Research Section A: Accelerators, Spectrometers, Detectors and Associated Equipment*, 693:209–214, 2012.

[90] RR Spencer, R Gwin, and R Ingle. A Measurement of the Average Number of Prompt Neutrons from Spontaneous Fission of Californium-252. *Nuclear Science and Engineering*, 80(4):603–629, 1982.

[91] NE Holden and MS Zucker. Neutron Multiplicities for the Transplutonium Nuclides. Technical report, Brookhaven National Lab., Upton, NY (USA), 1985.

[92] MS Zucker and NE Holden. Parameters for Several Plutonium Nuclides and ^{252}Cf of Safeguards Interest. Technical report, Brookhaven National Lab., 1984.

[93] P Santi and M Miller. Reevaluation of Prompt Neutron Emission Multiplicity Distributions for Spontaneous Fission. *Nuclear science and engineering*, 160(2):190–199, 2008.

[94] National Nuclear Data Center. ENSDF Database.

[95] H Nifenecker, C Signarbieux, M Ribrag, J Poitou, and J Matuszek. Gamma-Neutron Competition in the De-excitation Mechanism of the Fission Fragments of ^{252}Cf. *Nuclear Physics A*, 189(2):285–304, 1972.

[96] Matthew J Marcath, Robert C Haight, Ramona Vogt, Matthew Devlin, Patrick Talou, Ionel Stetcu, Jørgen Randrup, Patricia F Schuster, Shaun D Clarke, and Sara A Pozzi. Measured and Simulated ^{252}Cf (SF) Prompt Neutron-Photon Competition. *Physical Review C*, 97(4):044622, 2018.

[97] Ronald Allen Knief, BW Wehring, and ME Wyman. Measurements of Equilibrium and Time-dependent Energy Spectra of Beta Rays from Californium-252 Fission Fragments. *Nuclear Science and Engineering*, 53(1):47–60, 1974.

[98] David Lee Wark. β Spectrum Following Fission from ^{252}Cf, 1987.

[99] NIST. NIST ESTAR Stopping-power And Range Tables For Electrons. `https://www-nds.iaea.org/relnsd/vcharthtml/VChartHTML.html`, 2013.

[100] H Nifenecker. Correction for Fission Neutron Detector Efficiency and Unfolding of Neutron Multiplicity Histograms. *Nuclear Instruments and Methods*, 81(1):45–48, 1970.

[101] BC Diven, HC Martin, RF Taschek, and J Terrell. Multiplicities of Fission Neutrons. *Physical Review*, 101(3):1012, 1956.

[102] Valentin F Turchin. Statistical Regularization. In *Advanced methods in the evaluation of nuclear scattering data*, pages 33–49. Springer, 1985.

[103] M Dakowski, Yu A Lazarev, VF Turchin, and LS Turovtseva. Reconstruction of Particle Multiplicity Distributions Using the Method of Statistical Regularization. *Nuclear Instruments and Methods*, 113(2):195–200, 1973.

APPENDIX

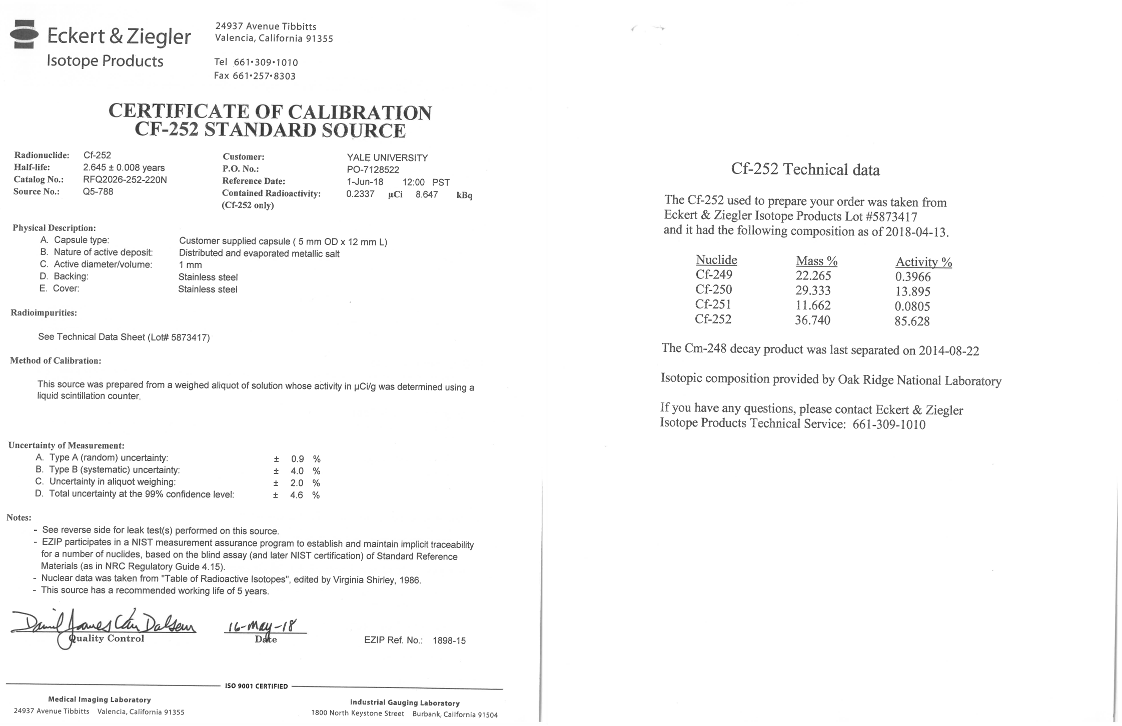

Eckert & Ziegler
Isotope Products

24937 Avenue Tibbitts
Valencia, California 91355

Tel 661•309•1010
Fax 661•257•8303

CERTIFICATE OF CALIBRATION
CF-252 STANDARD SOURCE

Radionuclide:	Cf-252	**Customer:**	YALE UNIVERSITY
Half-life:	2.645 ± 0.008 years	**P.O. No.:**	PO-7128522
Catalog No.:	RFQ2026-252-220N	**Reference Date:**	1-Jun-18 12:00 PST
Source No.:	Q5-788	**Contained Radioactivity:** (Cf-252 only)	0.2337 µCi 8.647 kBq

Physical Description:

A. Capsule type:	Customer supplied capsule (5 mm OD x 12 mm L)
B. Nature of active deposit:	Distributed and evaporated metallic salt
C. Active diameter/volume:	1 mm
D. Backing:	Stainless steel
E. Cover:	Stainless steel

Radioimpurities:

See Technical Data Sheet (Lot# 5873417)

Method of Calibration:

This source was prepared from a weighed aliquot of solution whose activity in µCi/g was determined using a liquid scintillation counter.

Uncertainty of Measurement:

A. Type A (random) uncertainty:	± 0.9 %
B. Type B (systematic) uncertainty:	± 4.0 %
C. Uncertainty in aliquot weighing:	± 2.0 %
D. Total uncertainty at the 99% confidence level:	± 4.6 %

Notes:

- See reverse side for leak test(s) performed on this source.
- EZIP participates in a NIST measurement assurance program to establish and maintain implicit traceability for a number of nuclides, based on the blind assay (and later NIST certification) of Standard Reference Materials (as in NRC Regulatory Guide 4.15).
- Nuclear data was taken from "Table of Radioactive Isotopes", edited by Virginia Shirley, 1986.
- This source has a recommended working life of 5 years.

Daniel James Van Dalsem
Quality Control

16-May-18
Date

EZIP Ref. No.: 1898-15

ISO 9001 CERTIFIED

Medical Imaging Laboratory
24937 Avenue Tibbitts Valencia, California 91355

Industrial Gauging Laboratory
1800 North Keystone Street Burbank, California 91504

Cf-252 Technical data

The Cf-252 used to prepare your order was taken from Eckert & Ziegler Isotope Products Lot #5873417 and it had the following composition as of 2018-04-13.

Nuclide	Mass %	Activity %
Cf-249	22.265	0.3966
Cf-250	29.333	13.895
Cf-251	11.662	0.0805
Cf-252	36.740	85.628

The Cm-248 decay product was last separated on 2014-08-22

Isotopic composition provided by Oak Ridge National Laboratory

If you have any questions, please contact Eckert & Ziegler Isotope Products Technical Service: 661-309-1010

Figure 6.1: ^{252}Cf manufacturer source certificate.